2

JET PROPULSION LABORATORY
CALIFORNIA INSTITUTE OF TECHNOLOGY
PASADENA, CALIFORNIA

FINAL REPORT

FLOW FIELD COMPUTATIONS FOR BLUNT BODIES IN PLANETARY ENVIRONMENTS

By

Stanley Byron, Richard M. Foster, and Bruce S. Masson

Contract No. 951646

(Subcontract under NASA Contract NAS7-100)

Submitted by

PHILCO-FORD CORPORATION
SPACE AND RE-ENTRY SYSTEMS DIVISION

In Cooperation with

APPLIED RESEARCH LABORATORIES, AERONUTRONIC DIVISION

22 April, 1968

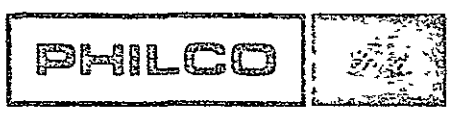

PHILCO-FORD CORPORATION
Space & Re-Entry Systems Division
Newport Beach, Calif • 92663

This work was performed for the Jet Propulsion Laboratory, California Institute of Technology, sponsored by the National Aeronautics and Space Administration under Contract NAS7-100.

ABSTRACT

Numerical methods to determine the flow field around blunt bodies traveling at hypersonic speeds in planetary atmospheres are presented. The state and motion variables and the convective and radiative heat transfer are determined for both equilibrium and non-equilibrium flow models. The flow model is chosen to be applicable to conditions encountered in typical out-of-orbit and hyperbolic Martian entry trajectories where maximum stagnation point convective and radiative heat transfer occurs. For the conditions of interest, the coupling between the inviscid region, the viscous region, and the radiative transfer is significant, and is included through simplified engineering approximations Numerical results are presented for equilibrium and non-equilibrium flow over a sphere-cone having a base diameter of 12 ft, and moving at 19,600 ft/sec in a 70% N_2, 30% CO_2 atmosphere at an ambient density of 10^{-6} slugs/ft^3. Results are also given for non-equilibrium flow over a sphere-cap at the same flight condition.

CONTENTS

ILLUSTRATIONS

ILLUSTRATIONS (continued)

ILLUSTRATIONS (continued)

LIST OF TABLES

SYMBOLS

a	sound speed
$B_{i+\frac{1}{2},j+\frac{1}{2}}$	geometric quantity, defined by Equation (A9)
c	speed of light
C	reaction rate constant
$d_{i,i+\frac{1}{2}}$	length of bow shock between rays i and $i+1$
$e(p\ \rho)$	specific thermodynamic internal energy
E',E''	electronic states of a molecule
$E_{j,i+\frac{1}{2}}, E_{j+\frac{1}{2},i}$	specific total energies on cell boundaries
E_{vj}	vibrational energy of species j
f	vector of conservation quantities
$G_{j+\frac{1}{2},i+\frac{1}{2}}, G^{j+\frac{1}{2},i+\frac{1}{2}}$	areas of cell $j+\frac{1}{2},i+\frac{1}{2}$ at t_o and $t_o+\tau$
$G_{j,i+\frac{1}{2}}$	area swept by inward motion of cell boundary, $j,i+\frac{1}{2}$
$h(p,\rho)$	specific enthalpy
h_j	free enthalpy of species j
h	increment in space variable
h	Planck's constant
$I_{j+\frac{1}{2},i}, I_{j,i+\frac{1}{2}}$	geometry quantity, defined by Equations (A27) and (A28)

i	index for increments along shock layer from axis
j	index for increments across shock layer from shock
J', J''	index of rotational states of a molecule
k	values 0 or 1 for respectively plane and axi-symmetric flow
k	Boltzmann's constant
$\overline{K}_i$	Equilibrium constant for reaction i
k_f	forward reaction rate coefficient
$\ell_{j,i}$	length from x axis along ith ray to intersection with jth body parallel
M	Mach number
M	molecular weight
m	mass flux from left to right across a disturbance front
p, P	pressure
$P_{j,i+\frac{1}{2}}, P_{j+\frac{1}{2},i}$	pressures on cell boundaries
$P(f)$	vector function of the flow variables
$Q(f)$	vector function of the flow variables
Q_{ij}	volume rate of production of species j by reaction i
q	fluid speed $\left[u^2+v^2\right]^{\frac{1}{2}}$
q_s	stagnation point heat transfer
r	ratio of p/ρ to e
$R_{j,i+\frac{1}{2}}, R_{j+\frac{1}{2},i}$	densities on cell boundaries
$R(f)$	vector function of the flow variables
R_o, R_N	body nose radius of curvature

R_{e_o}	Reynolds number in the stagnation region
S	entropy
$S_{j,i+\frac{1}{2}}, S_{j+\frac{1}{2},i}$	lengths of cell boundaries
t	time
t_o	time at beginning of time step
T	temperature
u	x component of fluid velocity
$\bar{u}$	ratio of characteristic vibrational temperature of a molecule to the translational temperature
u_o	anharmonicity correction
$U_{j,i+\frac{1}{2}}, U_{j+\frac{1}{2},i}$	x components of fluid velocity on cell boundaries
v	y component of fluid velocity
V', V''	index of vibrational states of a molecule
$V_{j,i+\frac{1}{2}}, V_{j+\frac{1}{2},i}$	y components of fluid velocity on cell boundaries
$V^{\pm}$	velocity of right and left running disturbance fronts
$V_{i+\frac{1}{2}}$	velocity of shock segment $1,i+\frac{1}{2}$ normal to itself
V_i	velocity of shocks intersection with the ith ray
V_n	outward normal velocity of cell boundary
w_n, w_t	fluid velocity components in cell resolved normal and tangential to cell boundaries
$W_{j+\frac{1}{2},i}, W_{j,i+\frac{1}{2}}$	fluid velocities normal to cell boundaries
x,y	spatial coordinates respectively, along and normal to the plane or axis of symmetry of body
z	spatial coordinate along a streamline

Greek Symbols

$\beta_{i\alpha}$	mole number of species α produced (positive) or consumed (negative) in reaction i
γ	ideal gas ratio of specific heats
γ_i	mole fraction of species i
ϵ	specific total energy, i.e., internal plus kinetic energy
θ_i	angle between ith ray and x-axis
$\phi_{j,i+\frac{1}{2}}, \phi^{j,i+\frac{1}{2}}$	geometric quantity, defined by Equations (A18) and (A20)
λ	radiation wavelength
ρ	density
μ	viscosity
$\bar{\mu}'$	spectral absorption coefficient
τ	time increment
τ_{max}	max time increment for numerical stability
$\sigma_{j,i+\frac{1}{2}}$	angle of segment, $j,i+\frac{1}{2}$ relative to x-axis
ξ_i	intercept of ray i on x-axis
Ω	control area for integral law
ω	radiation frequency
$\nu_{i\alpha}$	mole number of species α produced in reaction i
$\nu'_{i\alpha}$	mole number of species α consumed in reaction i
$\partial\Omega$	boundary of Ω
$\pm$	upper or lower sign used consistently through formula

Subscripts

t,x,y	differentiation with respect to t,x,y
∞,o	free stream quantities
cd	state on contact discontinuity
stag or s	stagnation point values
w	vehicle wall values

Superscripts

+,-	fluid state right and left respectively of discontinuity
n	index of time steps
o	modification values needed at axis of symmetry
·	differentiation with respect to time, $\dot{\sigma}$ denoting angular velocity
‾	denotes average or approximate quantity used during convergence
*	excited state population

SECTION 1

INTRODUCTION

The flight conditions and the planned vehicle shapes for Martian entry pose a number of problems in making satisfactory flow field predictions. Because of the low ballistic coefficient vehicles, peak heating occurs at low ambient density, which leads to a relatively thick viscous region. The high emissivity of CO_2-N_2 mixtures leads to significant radiative heat transfer. Because of the low ambient density, much of the gas in the shock layer is out of equilibrium and produces larger radiation emission than would be produced if the gas were at equilibrium. Finally, because of the low density and high emissivity, the radiation losses from the shock layer gas lead to a reduction in gas enthalpy. To carry out the desired flow field calculations, the flow model must include all of these physical effects, but it should not become unnecessarily complicated. Thus we have chosen the simplest methods of calculation that retain the essential physical information.

A survey of applicable theoretical and experimental low Reynolds number shock layer studies indicates a wide variation in the method of solution, the gas models, and the assumed free stream conditions with a corresponding large variation in the predicted magnitude of "rarefied regime" effects.

At present one of the most general and yet definitive studies of rarefied gas regimes is that given by Goldberg.[1] In this study, non-similar hypersonic continuum flow field sphere-cap solutions were obtained for a flow model which is applicable through the incipient merged layer regime.[2] An examination of the results of References 1 and 3 indicates that for the shock layer Reynolds numbers of interest in this study, viscous and conduction effects due to velocity and temperature gradients at the shock and in the inviscid shock layer can be neglected. Thus, Rankine-Hugoniot shock relations and inviscid shock layer equations can be used to calculate the flow field. It also is assumed that the vehicle wall is cold in this study and, thus, the boundary layer displacement thickness is small and the inviscid shock shape and body pressure distribution are not affected appreciably by the boundary layer.

For the flight conditions given in this study, the low Reynolds number results[1,3] predict greater convective heat transfer rates than are obtained from the classical discontinuous shock - inviscid shock layer - thin boundary layer theory. This increase in heat transfer is primarily due to the shock layer vorticity induced by the curved bow shock. The effect of vorticity can be incorporated in conventional boundary layer theory, however, as long as the proper boundary layer edge velocity conditions are used.[1,3]

In computing radiative heat transfer it is apparent from shock tube data that for the flight conditions under study much of the gas in the shock layer is out of equilibrium. However techniques for computing non-equilibrium radiative heat transfer are not yet well developed. Thus it is desirable to carry out equilibrium calculations as well; although an equilibrium flow model is less realistic here, the accuracy of the numerical results is greater. In Section 2 below, the equilibrium flow model is described and in Section 3 the non-equilibrium model is set forth. The numerical results are given in Section 4.

SECTION 2

EQUILIBRIUM FLOW

2.1 INVISCID ANALYSIS

It was originally planned to use the first approximation method of integral relations computer program to determine the inviscid flow properties. A number of modifications in the analysis were needed, however. As these were investigated, it became apparent that several difficulties could not be overcome satisfactorily. The major problem with the first approximation integral relation solution is that, at the low specific heat ratios which are representative of the equilibrium case, the 60° cone shock layer thickness is significantly overestimated. This difficulty is illustrated further in Section 4.1. It was also found that the stagnation point velocity gradient was not determined accurately by the one strip integral method[4] and that attempts to infer this quantity from the numerical results were unsuccessful. Furthermore integration of the inviscid flow equations through the transonic region was found to be very difficult and could not be carried out satisfactorily. Thus an alternative and, fortunately, more accurate method was applied to this problem. This method was under development at the time the present program was planned.

The method has been developed here for the computation of either planar or axisymmetric blunt body flow fields. For steady flow fields the formulation of the problem is direct in the sense that the body is given and the shock wave computed. Steady flows are computed as the large time limits of transient flows. The time dependent equations of motion are solved by a finite difference technique. The stable, explicit finite difference approximations are determined by a method proposed by Godunov, Zabrodin and Prokopov.[5]

An initial condition in the form of velocity components, density, pressure and internal energy plus kinetic energy is specified on a mesh covering the region of integration. This initial data is in theory arbitrary, but in practice is specified by a steady, constant γ flow field. The amount by which the data does not satisfy the steady equations of motion determines the time derivative of the flow field. The time derivative then determines new values of the flow variables in each cell of the mesh. In this manner, the flow field evolves in time, subject to the conservation laws, from the specified initial conditions.

The boundaries of the mesh are dependent on the method by which the bow shock is treated. It has been common practice in finite difference computations to ignore the existence of shock waves and leave their treatment to the finite difference scheme itself. The computed shocks are represented by smooth but rapid transitions of flow variables over a linear distance of nominally 5 to 10 mesh points. To adequately model the flow variations, 5 mesh points should constitute a small portion of the shock layer width, and commonly 50 to 100 points would be required between the body and the upstream mesh boundary at which a uniform stream condition is applied. Smeared shock calculations of this type have proved to be quite feasible for blunt body flows, Bohachevsky[6] has used Lax's scheme,[7] Burstein[8] used the Lax-Wendroff scheme,[9] and Emery[10] compared Rusanov's scheme[11] with those of Lax and Lax-Wendroff.

The alternative employed in this code is to retain the bow shock as a discontinuous boundary of the region of integration. To achieve this distribution of computational points, it is necessary to introduce a mesh that always exactly fills the shock layer. The cells in the mesh expand and contract as the standoff distance between the shock and body increases or decreases as a function of time and position. The upstream boundary of the mesh maintains the full jump in flow variables from the free stream to the shock layer values immediately behind the shock. This type of mesh has been widely used in the blunt body problem; in the time dependent form, see Hayes and Probstein,[2] Godunov, Zabrodin and Prokopov,[5] Moretti and Abbett.[12]

In addition to the bow shock wave, the boundary of the region of integration is composed of the x-axis, the trace of the body in the xy plane, and a surface entirely embedded in the supersonic portion of the flow, across which there is no upstream influence.

Given the upstream and body portions of the mesh boundary, the internal mesh is constructed in the following manner. Straight line rays are selected which intersect both the body and the upstream shock boundaries. The ith ray makes an angle θ_i with respect to the x-axis and intersects the axis at the position $x = \xi_i$ as illustrated in Figure 1. The rays divide the shock layer into discrete intervals along the body. The first of these rays is coincident with the x-axis, and the last forms the downstream boundary, immersed in supersonic flow.

The interval on each ray between the interaction with the upstream and body boundaries is divided into a fixed number of subintervals, say J. Let $\ell_{1,i}$ represent the distance from the x-axis measured along the ray θ_i to the intersection of the ray and upstream-shock boundary, and $\ell_{J+1,i}$ denote the similarly measured body-ray intersections. Then the lengths $\ell_{j+1,i}$ and $\ell_{j,i}$ denote the inner and outer end points of the jth subinterval in from the bow shock boundary.

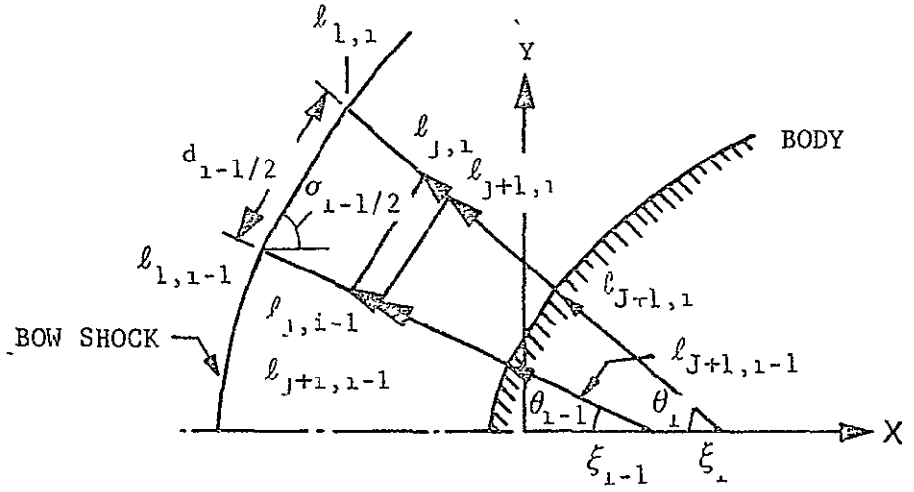

FIGURE 1. MESH GEOMETRY FOR SHOCK LAYER AND CELL $j+1/2$, $i+1/2$

When the points $\ell_{j,i}$ for fixed j are connected by straight line segments, a polygonal interpolation curve running along the shock layer is obtained. These interpolating polygons and the rays divide the shock layer into a mesh of quadrilateral cells upon which the difference equations are constructed.

The cell bounded by the ith and i+1st rays and the jth and j+1st transverse interpolating polygon is denoted by $j+\frac{1}{2}, i+\frac{1}{2}$. Similarly, the interval on the ith ray bounded by the intersections with the jth and j+1st interpolating polygon is denoted by $j+\frac{1}{2},i$. Finally the segment of the jth interpolating polygon, $j, i+\frac{1}{2}$ is that segment running between the ith and i+1st rays, see Figure 1.

2.1.1 FINITE DIFFERENCE EQUATIONS

The differential conservation laws will be used in the form

$$f_t + P_x + Q_y + y^{-1}R = 0 \tag{1}$$

The quantities f, P, Q, R are the following vector valued functions

$$f = \begin{bmatrix} \rho \\ \rho u \\ \rho v \\ \rho \epsilon \end{bmatrix} \tag{2}$$

$$P(f) = \begin{bmatrix} \rho u \\ \rho u^2+p \\ \rho uv \\ \rho u\epsilon+up \end{bmatrix} \tag{3}$$

$$Q(f) = \begin{bmatrix} \rho v \\ \rho uv \\ \rho v^2+p \\ \rho v\epsilon+vp \end{bmatrix} \tag{4}$$

$$R(f) = k \begin{bmatrix} \rho v \\ \rho uv \\ \rho v^2 \\ \rho v(\epsilon + \frac{p}{\rho}) \end{bmatrix} \tag{5}$$

where $k = 0,1$ for plane and axisymmetric problems respectively and $\epsilon = e(p,\rho) + \frac{1}{2}(u^2+v^2)$ is the internal plus kinetic energy.

The difference equations are generated by integrating Equation (1) over a cell $\Omega(t)$, whose boundaries are time dependent due to the floating mesh, and from initial time t_o to $t_o+\tau$. The integrated form reads

$$\iint_{\Omega(t_o+\tau)} f(x,y,t_o+\tau)dxdy = \iint_{\Omega(t_o)} f(x,y,t_o)dxdy + \int_{t_o}^{t_o+\tau} dt \left\{ \int_{\partial\Omega(t)} f(x,y,t)V_n ds \right.$$

$$\left. - \oint_{\partial\Omega(t)} (Pdy - Qdx) - \iint_{\Omega(t)} \frac{1}{y} R(x,y,t)dydx \right\} \tag{6}$$

where $\partial\Omega$ is the boundary of Ω and V_n represents the component of the boundary velocity in the outward normal direction. This equation is to be evaluated to first order in smallness of time step τ and altitudes h_x, h_y of the cell Ω. The derivation of the finite difference equations is completed in Appendix A.

2.1.2 SOLUTION OF DIFFERENCE EQUATIONS AND EQUATION OF STATE

An equation of state must be added to finite difference Equations (A13) to (A16) before a computation can be carried through. For equilibrium runs, an Ames polynomial fit to the equation of state of a 30% CO_2-70% N_2 mixture was employed.[14] The polynomials provide the internal energy, e, and sound speed, a, as a function of p and ρ. However ρ and e are the thermodynamic variables determined at the new time by the conservation laws. Thus some iteration process is necessary to determine p accurately at each time. This iteration can be done simultaneously with the flow field's approach to steadiness in such a manner as to require no additional evaluations of the polynomials.

The initial thermodynamic data in the cells is specified by $p^{(o)}$ and $\rho^{(o)}$. From this data the internal energy $\bar{e}^{(o)}$ is determined from the Ames tables. The ratio $r^{(o)}$ is defined by

$$r^{(o)} = \frac{p^{(o)}}{\rho^{(o)}\bar{e}^{(o)}} \tag{7}$$

At the nth time step, the quantities $p^{(n)}$, $\rho^{(n)}$ $\bar{e}^{(n)}$ and $r^{(n)}$ are determined from these same quantities at the $n\text{-}1^{st}$ time step in the following manner. The conservation laws will provide the quantities $\rho^{(n)}$ and $e^{(n)}$ from $\rho^{(n-1)}$, $\bar{e}^{(n-1)}$ and $p^{(n-1)}$. The new pressure will be given by

$$p^{(n)} = r^{(n-1)}\rho^{(n)}e^{(n)} \tag{8}$$

The Ames tables will give $\bar{e}^{(n)}$ as a function of $p^{(n)}$ and $\rho^{(n)}$ and the ratio $r^{(n)}$ follows as

$$r^{(n)} = \frac{p^{(n)}}{\rho^{(n)}\bar{e}^{(n)}} \tag{9}$$

When steadiness of the flow field is achieved $p^{(n-1)} = p^{(n)}$, $\rho^{(n-1)} = \rho^{(n)}$ and $\bar{e}^{(n-1)} = \bar{e}^{(n)}$. From Equation (8) $\bar{e}^{(n)} = e^{(n)}$ and hence a consistent answer is achieved on convergence. The convergence of this scheme depends upon the polynomial coefficients in the Ames tables. Qualitatively

convergence is achieved since the quantity r varies very slowly with any of the thermodynamic quantities. Over the entire flow field r will vary by about 20% and by no more than 1% over a time step. Thus the $p^{(n-1)}$ predicted by Equation (8) will be quite accurate for use in the conservation laws and $e^{(n)}$ and $\bar{e}^{(n)}$ will not differ appreciably.

2.1.3 FLUXES ACROSS CELL BOUNDARIES

The flow quantities on the cell boundary segments internal to the mesh are given in Godunov's scheme by the solution of a related one dimensional unsteady flow problem. The one dimensional problem is constructed using the pressure, density and normal component of the fluid velocity relative to the cell boundary velocity in the two cells adjacent to the segment. These values are used to define the initial uniform states in a Riemann problem, the general discontinuity separating two uniform fluid states. This discontinuity evolves in time through left and right running disturbances separated by a contact discontinuity. The full solution for the properties is prescribed in Courant and Friedrichs.[13]

As numerically demonstrated by Godunov, stability is maintained, even when computing through a shock, when the solution of the Riemann problem is linearized with respect to small differences across the discontinuity. Then any rarefaction disturbances have negligible width and the cell boundary lies in one of four constant state regions: (1) to the left of the left running disturbance, (2) between the left running disturbance and the contact surface, (3) between the contact surface and the right running disturbance, (4) to the right of the right running disturbance, see Figure 2. Note that the t axis is the position of the cell boundary.

If the disturbances propagate so that the t axis is located in regions (1) or (4), the cell boundary lies in undisturbed fluid. The pressure, density and velocity components on the boundary are equal to the quantities in the cells corresponding to the initial left or right states. If the t axis

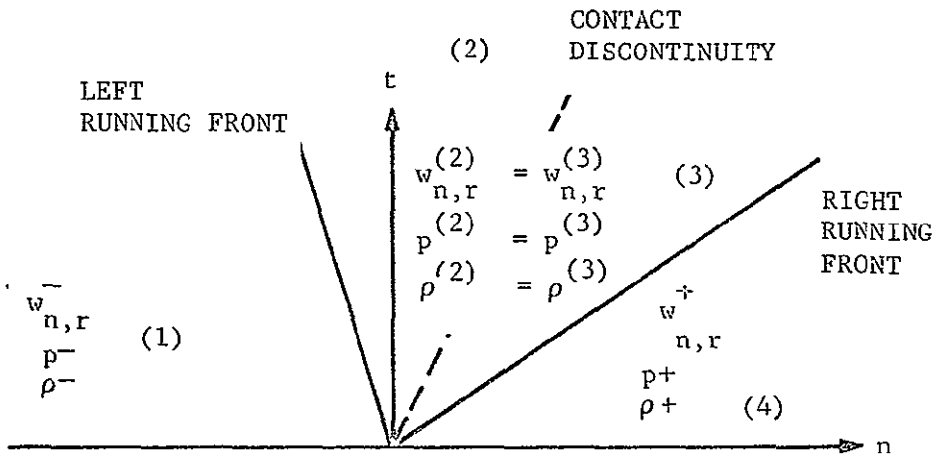

FIGURE 2. EVOLUTION OF DISCONTINUITY IN FLUID STATE

is located in regions (2) or (3), the cell boundary lies behind a disturbance, and the pressure and normal velocity component are determined by expansion of the solution in Reference 13. Denoting the average of the initial right and left state by bars and the difference of the left from the right state by Δ's, permits the pressure and normal relative velocity components, $w_{n,r}$, in regions (2) and (3) to be written as

$$p^{(2)} = p^{(3)} = \bar{p} - m\Delta w_{n,r}/2 + O(\Delta^2) \tag{10}$$

$$w_{n,r}^{(2)} = w_{n,r}^{(3)} = w_{n,r} - \Delta p/2m + O(\Delta^2) \tag{11}$$

$$m = \bar{\rho}\,\bar{a} + O(\Delta^2) \tag{12}$$

where $\bar{a}$ is the sound speed evaluated at $\bar{p}$, $\bar{\rho}$. The entropy s is constant across the disturbances

$$s^{(1)} = s^{(2)} \tag{13}$$

$$s^{(3)} = s^{(4)} \tag{14}$$

The pressure on the cell boundary has the value $p^{(2)}$, and the normal component of the fluid velocity relative to the boundary velocity is $w_{n,r}^{(2)}$. The density on the cell boundary is determined by the known values of pressure and entropy, and the fluid velocity component tangential to the cell boundary has a value equal to those in regions (1) and (4) depending on whether the t-axis lies to the left or right of the contact discontinuity.

2.1.4 BOW SHOCK BOUNDARY CONDITIONS

At the beginning of a time step, say t_o, each bow shock segment separates a cell containing a uniform state of fluid from the free stream. Let the state in the cell bordering the bow shock be denoted by p^+, ρ^+, w_n^+, w_t^+, where w_n^+, w_t^+ are the components of the fluid velocity resolved normal and tangential to the bow shock segment. The jump in the properties p^+, ρ^+, w_n^+ to the free stream values p_∞, ρ_∞, q_{∞_n} can be viewed as a Riemann

problem in a coordinate n normal to the segment of the bow shock, with $n > 0$ directed downstream and $n < 0$ upstream. The left running disturbance must be identified with the actual bow wave. The right running disturbance carries the information of the bow wave's motion during the ensuing time interval into the first cell.

For the bow shock, if

$$m^- = [p_{cd}-p^-)(1/\rho^- - 1/\rho^-_{cd})]^{\frac{1}{2}} \tag{15}$$

then the momentum equation is

$$w^-_n m^- + p^- = w_{ncd} m^- = p_{cd} \tag{16}$$

and the Hugoniot relation is

$$e^-_{cd} - e^- = \tfrac{1}{2}(p_{cd} + p^-)\ (1/\rho^- - 1/\rho^-_{cd}) \tag{17}$$

The right running disturbance on the other hand is weak and travels with the sound speed, a^+, into the interior of the cell. Then

$$m^+ = \rho^+ a^+ \tag{18}$$

is known explicitly. The momentum balance across this disturbance is

$$w_{n,cd} m^+ + p_{cd} = w_n^+ m^+ + p^+ \tag{19}$$

Equations (15)-(19) can be iterated to determine the pressure and normal velocity on the contact surface, p_{cd} and $w_{n,cd}$ which determine in turn the quantities R, U, V, P, E to be used in Equations (A13) through (A16). If the cell under consideration is 3/2, $i+\frac{1}{2}$ the fluxes are to be determined from

$$R_{1,i+\frac{1}{2}} = \bar{\rho}_{cd}$$

$$(W_n)_{1,i+\frac{1}{2}} = w_{cd}$$

$$(W_t)_{1,i+\frac{1}{2}} = q_\infty \cos\sigma_{1,i+\frac{1}{2}}$$

$$R_{1,i+\frac{1}{2}} = p_{cd} \tag{20}$$

where $\sigma_{1,i+\frac{1}{2}}$ is the angle of the bow shock segment 1, $i+\frac{1}{2}$ relative to the free stream direction. The velocity of the bow wave, $\bar{V}$, can be found, after $\bar{m}$ is known, from the mass conservation principle

$$\rho_\infty(q_{\infty,n} - \bar{V}) = \bar{m} \tag{21}$$

2.1.5 MESH DEFORMATION DURING TIME STEP

Since the upstream boundary of the mesh is the only portion of the boundary that moves, the deformation of the mesh during the time increment follows from the analysis of the preceding section. If V_i is the velocity of the intersection of the shock with the ith ray inwardly directed, then the mesh deformation will be determined by the differential equation

$$\frac{d\ell_{1,i}}{dt} = V_i \tag{22}$$

After each segment of the bow shock is allowed to move parallel to itself during the increment τ, the shock, though continuous initially, would not end up continuous. What was neglected above was the angular velocity of rotation of the segment, $\dot{\sigma}_{1,i+\frac{1}{2}}$. Let $V_{i+\frac{1}{2}}$, denote the shock velocity for the shock segments just above and below the ray i. The $V_{i\pm\frac{1}{2}}$ of course are the $\bar{V}$ determined previously for the two cells. From Figure 3 it is seen that V_i can be expressed in two ways one relative to the lower ray, the other relative to the upper. It follows that

$$V_i = \frac{V_{i+\frac{1}{2}}}{\sin(\sigma_{1,i\pm\frac{1}{2}} + \theta_1)} \mp \frac{\dot{\sigma}_{1,i+\frac{1}{2}} \cdot d_{1,i+\frac{1}{2}}}{2\sin(\sigma_{1,i\pm\frac{1}{2}} + \theta_1)}$$

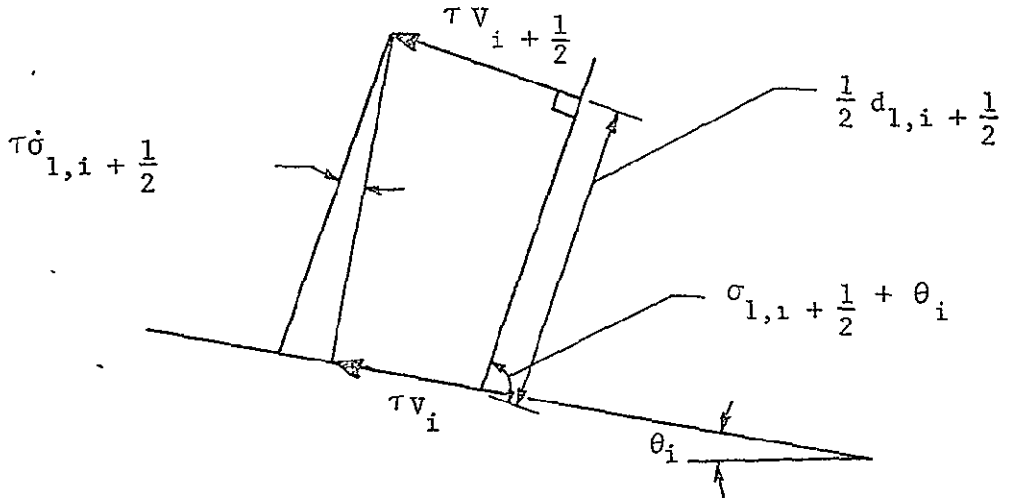

FIGURE 3. RESOLUTION OF SHOCK-RAY NODAL VELOCITY

where the lower or upper signs are used consistently throughout the expression and $d_{1,\imath\pm\frac{1}{2}}$ are the lengths of the bow wave segments above and below ray i. If the expression with the upper sign is multiplied by $\frac{\sin(\sigma_{1,i+\frac{1}{2}}+\theta_i)}{d_{1,i+\frac{1}{2}}}$ and the expression with lower sign by $\frac{\sin(\sigma_{1,\imath-\frac{1}{2}}+\theta_i)}{d_{1,\imath-\frac{1}{2}}}$ and the resulting expressions added, then V_i can be expressed as

$$V_i \doteq \frac{V_{i+\frac{1}{2}}d_{1,\imath+\frac{1}{2}} + V_{\imath-\frac{1}{2}}d_{1,i-\frac{1}{2}}}{d_{1,i-\frac{1}{2}}\sin(\sigma_{1,\imath+\frac{1}{2}}+\theta_i) + d_{1,i+\frac{1}{2}}\sin(\sigma_{1,\imath-\frac{1}{2}}+\theta_i)}$$

$$+ \tfrac{1}{2}(\dot{\sigma}_{1,i+\frac{1}{2}}-\dot{\sigma}_{1,i-\frac{1}{2}}) \cdot O(d_{1,\imath\pm\frac{1}{2}}) \qquad (23)$$

where only the order of the coefficient of $(\dot{\sigma}_{1,\imath+\frac{1}{2}}-\dot{\sigma}_{1,\imath-\frac{1}{2}})$ is indicated. The first term on the right is seen to be O(1) while the last term is $O(d^2_{1,i\pm\frac{1}{2}}) = O(h^2)$ and is to be neglected in a first order scheme. Thus the motion of the shock node on each ray is determined by the motion of the segments adjacent to that ray. The shock shape after τ is found by connecting the new nodal locations. The internal mesh deformation is subsequently found by interpolation on each ray with respect to the new standoff distance found from Equations (22) and (23).

2.1.6 BODY BOUNDARY CONDITION

The cells $J+\frac{1}{2}$, $\imath+\frac{1}{2}$ bordering the body satisfy the condition of zero normal velocity on their body boundary $J=1$, $\imath+\frac{1}{2}$. Let the cell state be denoted by p^+, ρ^+, w_n^+, w_t^+ where w_n^+, w_t^+ are the fluid velocity components normal and tangential to the body. Since the body boundary is stationary, the normal velocity condition is satisfied if a reflecting cell located immediately inside the boundary is imagined with state $p^- = p^+$, $\rho^- = \rho^+$, $w_t^- = w_t^+$ and $w_n^- = w_n^+$.

Since $m^+ = -m^-$ by Equation (25), Equations (26) and (29) require that $w_{n,cd} = 0$ which is the zero normal velocity condition. The pressure at the wall boundary is

$$p_{cd} = w_n^+ m^+ + p^+ \qquad (24)$$

This Riemann problem features a contact discontinuity which remains coincident with the body boundary.

2.1.7 EVALUATION OF THE ACCURACY OF THE INVISCID ANALYSIS

The accuracy of the method given here to compute inviscid flows has been evaluated by carrying out several test calculations. In Figure 4, the surface pressure on a sphere in a $M = 4.0$, $\gamma = 1.4$ free stream is compared with two other numerical calculations. The results of the present code contain some scatter, but the deviation from Belotserkovski's third approximation, scheme I, integral solution is less than 3%. A further confirmation of this estimate of the accuracy is that in the fine and coarse mesh comparisons of the blunt cone in an ideal gas the surface pressure on the cone differs by 2%.

A shock shape comparison with data is shown in Figure 5. On the conical portion the computed shock shape lies outside the data by less than 5%. However in the stagnation region it is difficult to make an accurate assessment from the photograph. In this region, comparison between the fine and coarse mesh computation of the blunt cone flow field again provides the error estimate. The coarser mesh is larger by 3.1% than the fine mesh value for $\gamma = 1.1$. The density along the entire stagnation streamline for the coarse mesh lies about 5% below the values for the fine mesh. If we assume a linear truncation error which is of order 3 to 5% when the mesh width is reduced by $\frac{1}{2}$, then the fine mesh results lie within 3 to 5% of the actual values with no truncation error and the coarse mesh values lie within 6% to 10% of the actual values.

The accuracy of the stagnation point velocity gradient was estimated during the checkout phase of the finite difference program by comparison with existing data,[15,16,17] correlations,[18,19] and numerical solutions.[20,21] Spheres in an ideal gas stream with $\gamma = 1.4$ at Mach numbers of 4.0, 5.0,

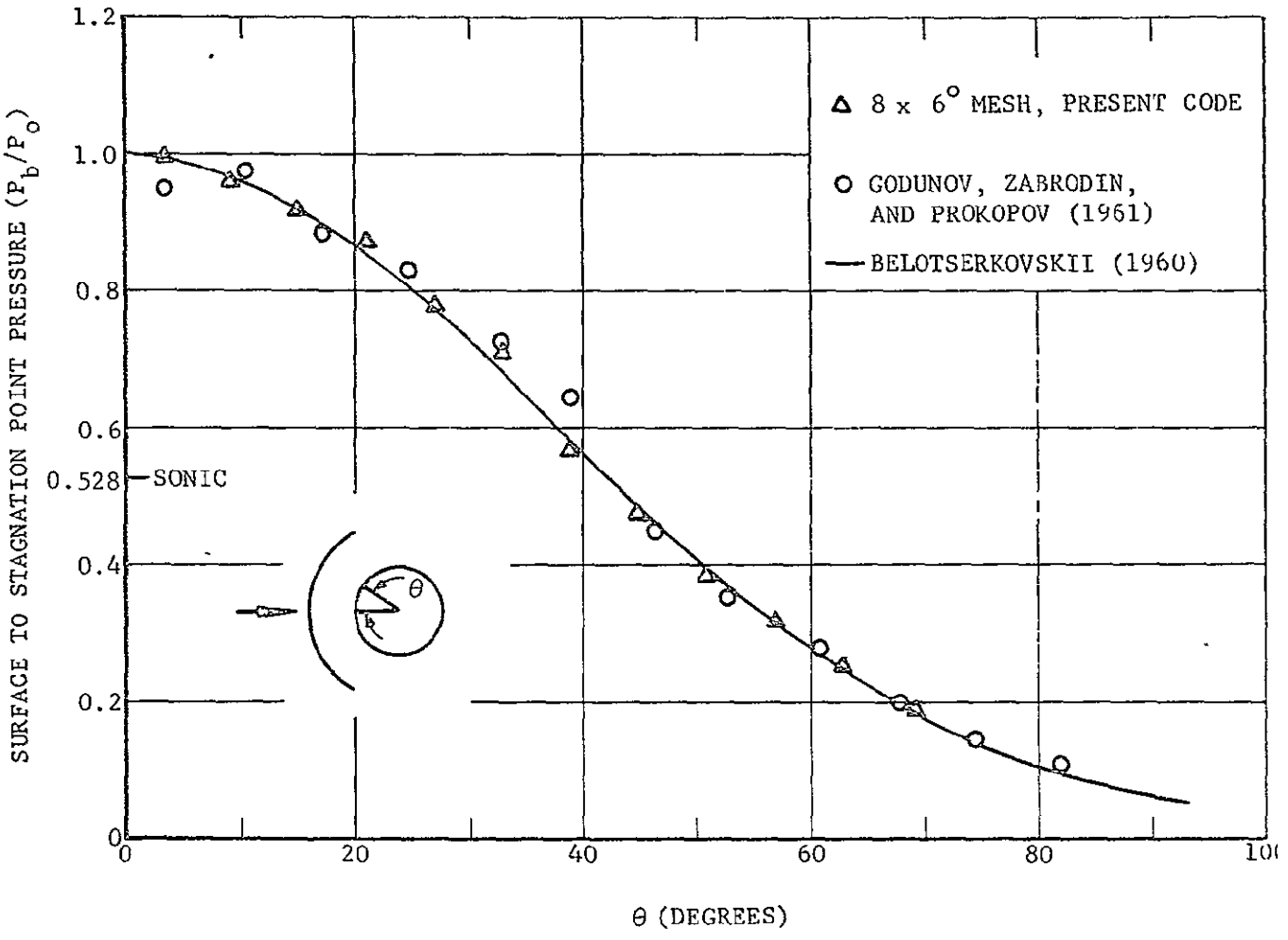

FIGURE 4. PRESSURE DISTRIBUTION ON A SPHERE

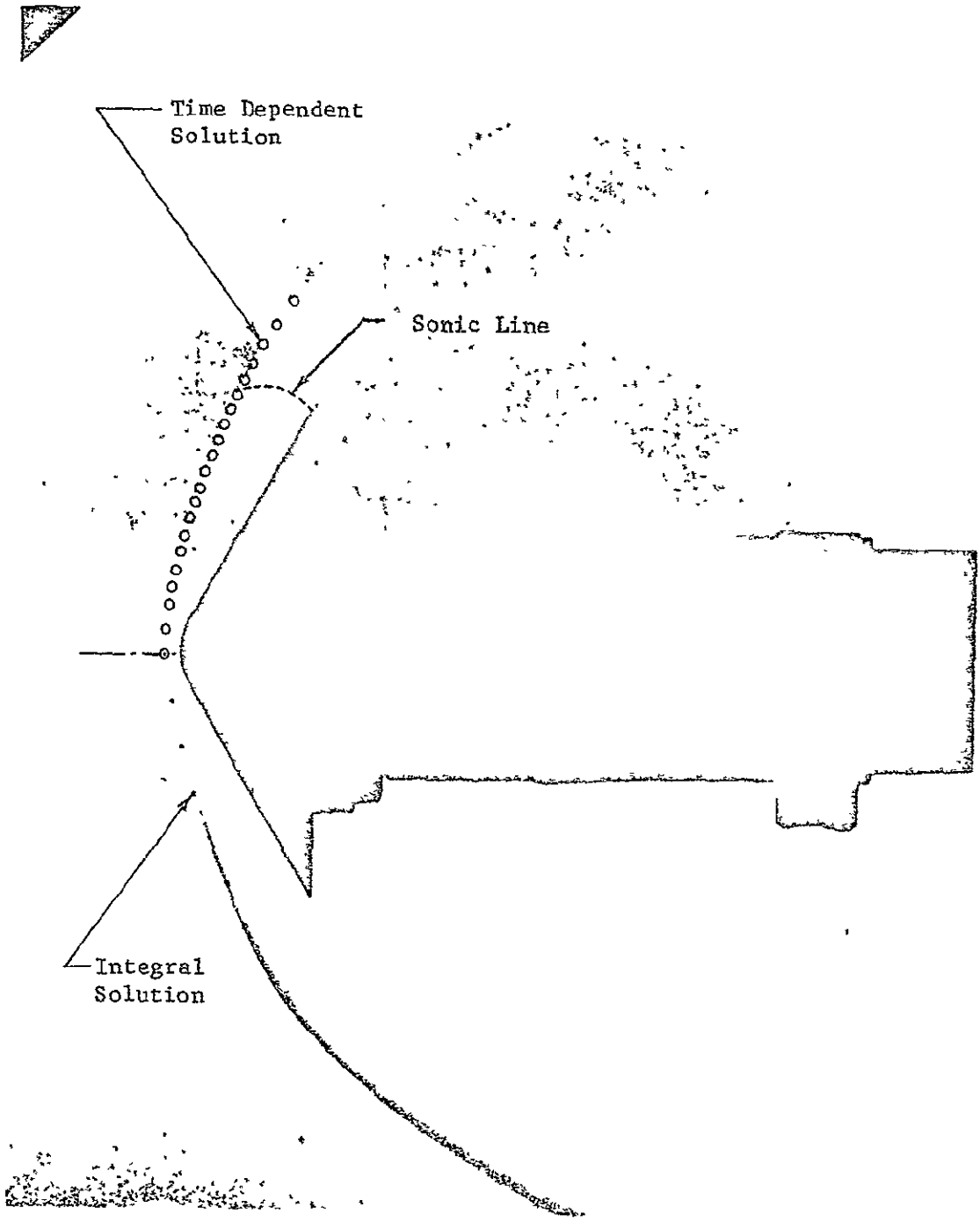

FIGURE 5. BLUNTED CONE SHOCK SHAPE COMPARISON WITH SCHLIEREN. $M_\infty = 9.0$, $\gamma = 1.4$ SCHLIEREN FROM DATA OF NICHOLS AND NIERENGRATEN[82]

8.0, and 10.0 were computed as the check cases. For these runs, the shock layer was covered by a mesh with 7 cells across the layer and 6^{o} increments along the surface. In Figure 6, a compilation of these results is presented, in which it is seen that the stagnation point velocity gradient computed by the Aeronutronic program lies well within the scatter of data for Mach numbers less than 5.0. There is a serious scatter between data correlation and theory at Mach numbers greater than 5.0. However, the Li-Geiger correlation formula, the two Belotserkovskii integral relations solutions (second approximation, scheme I and fifth approximation, scheme III), Manglers inverse method calculation and the Aeronutronic Godunov type program scatter less than 5% at these larger Mach numbers. The Belotserkovskii and Mangler results are inherently the most accurate, in which case, the Godunov finite difference program produces results about 2-4% too low.

For the 60^{o} blunt cone shape, an ideal gas computation was performed to give initial conditions for the required equilibrium solution. Two meshes were used both of which had 7.5^{o} intervals on the spherical portion while 3 and 6 cells were taken across the layer. The free stream conditions were specified by a Mach number of 20.0 and $\gamma = 1.1$. The coarse mesh computation gave

$$\frac{R_o}{q_\infty}\left(\frac{\partial q}{\partial s}\right)_{0,3} = .366 \quad , \gamma = 1.1$$

while the fine mesh yielded

$$\frac{R_o}{q_\infty}\left(\frac{\partial q}{\partial s}\right)_{0,6} = .372 \quad , \gamma = 1.1$$

These results agree closely with the value predicted by the constant density solution for a sphere

$$\frac{R_o}{q_\infty}\left(\frac{\partial q}{\partial s}\right)_{0,10} = \left(\frac{8}{3}\frac{\rho_\infty}{\rho_2}\right)^{\frac{1}{2}} = .365$$

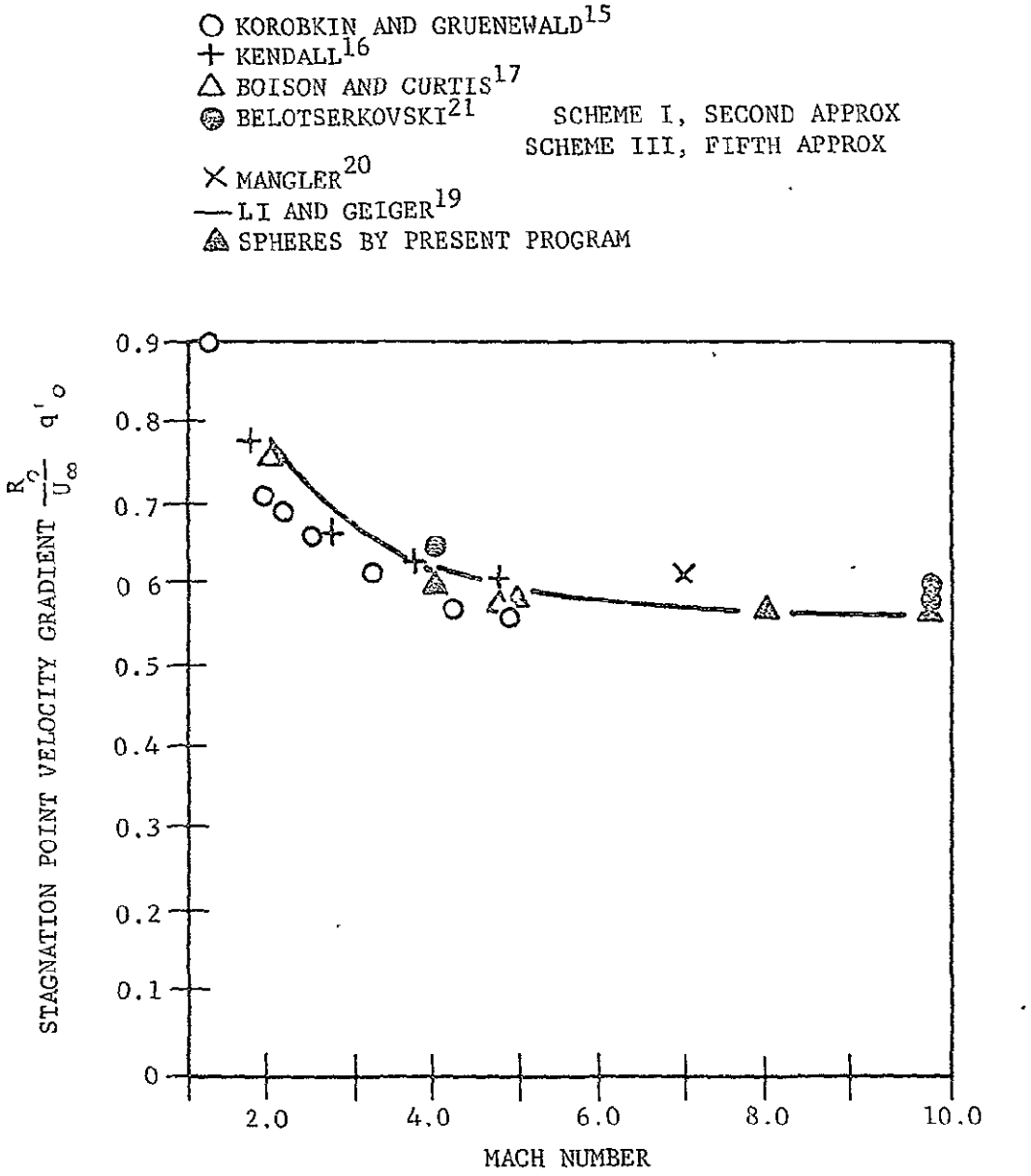

FIGURE 6. STAGNATION POINT VELOCITY GRADIENT ON SPHERES

This agreement with the asymptotic sphere values reflects the weak upstream influence of the conical surface in the $\gamma = 1.1$ case. Since a 60^{o} cone possesses an attached hypersonic shock layer solution, the only upstream influence of the conical portion is due to a narrow entropy layer at the surface. For a larger effective γ or larger cone angle, this phenomenon would not occur and a serious divergence between the spherical prediction and the actual computed value would arise.[20] The Li-Geiger correlation[19] is in error at the large density ratios encountered here as it has the wrong asymptotic limit as $\gamma \rightarrow 1$. Its predicted value is .315.

The equilibrium computation provided a stagnation point velocity gradient of

$$\left(\frac{\partial q}{\partial s}\right)_{0,\ equil} = .388\ \frac{q_\infty}{R_o} = 6340\ sec^{-1},$$

where the mesh is the coarse mesh in the preceding paragraph. This value corresponds to a constant density shock layer on a sphere with effective $\gamma = 1.125$, in agreement with the ratio h/e computed in the flow field. The error in this computed value of the stagnation point velocity gradient is estimated at less than 5%. This error is based on the average 3% error between the $\gamma = 1.4$ computations and those of Mangler and Belotserkovskii and the 1-2% difference noted between the fine and coarse mesh values.

2.2 CONVECTIVE HEAT TRANSFER ANALYSIS

The convective heat transfer calculations are complicated by the presence of low Reynolds number effects, significant quantities of CO_2 in the boundary layer, and dissociation and ionization effects. The following paragraphs outline the analytical methods, including the above considerations, which were utilized in this study.

In the discussion of the flow model in the introduction it was concluded that low Reynolds number effects are primarily manifested as vorticity

corrections to conventional boundary layer theory. At the stagnation point and on the spherical portion of the sphere-cone and the sphere-cap, the vorticity interaction effects have been calculated by using the method presented in Reference 3 and by utilizing the low Reynolds number sphere-cap solutions given in Reference 1. The method of Reference 3 is a solution to the boundary layer equations in which the slope of the boundary layer velocity profile is matched with the slope of the inviscid velocity profile for equal mass flow rates. The input parameters required to obtain a solution are the body Reynolds number, $R_{e_o} = \rho_o R_N^2 (\partial u/\partial x)/\mu_o$ and the normal velocity gradient, $\partial(u/u_o) \Big/ \partial(y/R_N)$. These parameters are given by the inviscid flow field solution. It was found that the method of Reference 3 and that of Reference 1 both give essentially the same results, but that some care must be taken when using the latter results. The low Reynolds number results of Reference 1 are presented as a ratio of the low Reynolds number heating to the classical boundary layer heating and are correlated in terms of shock density ratio and Reynolds number. The results of the correlation are shown in Figure 7. The classical boundary layer solution used to make the low Reynolds number heat transfer results non-dimensional is based on modified Newtonian boundary layer edge properties. High density ratio (ρ_s/ρ_∞) inviscid shock layer property results can differ considerably from modified Newtonian results. Thus the deviation of the low Reynolds number heat transfer from the so-called classical boundary layer result given in Figure 7 includes not only low Reynolds number effects, but also inviscid property effects.

In addition to low Reynolds number effects, the effect of significant concentrations of CO_2 in the ambient gas must be considered in the convective heat transfer calculations. Numerous theoretical and experimental studies of stagnation point convective heat transfer in N_2-CO_2 gas mixtures of interest in planetary entry have been made. The general result is that convective heat transfer increases as the percentage of

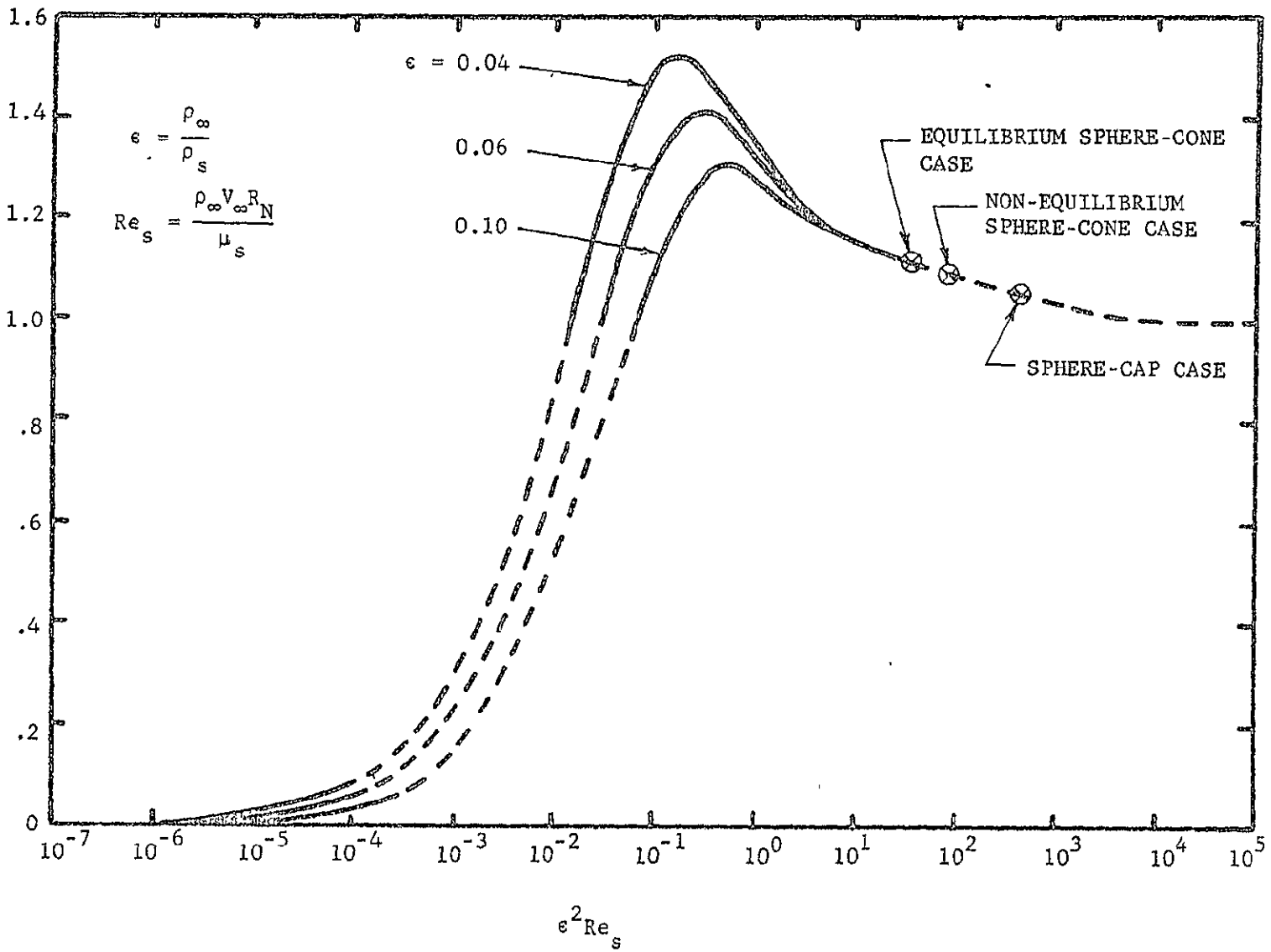

FIGURE 7. COMPARISON OF LOW REYNOLDS NUMBER AND CLASSICAL BOUNDARY LAYER THEORY STAGNATION POINT HEAT TRANSFER (REFERENCE 1)

CO_2 is increased. Predictions of the magnitude of the increase vary considerably, however. In this study the results of Scala and Gilbert[23] have been used to account for the ambient gas composition. In their analysis, an extensive number of gas mixtures has been studied, and their results provide a reasonable upper bound on the effects of CO_2 on convective heat transfer.

The correlation results of Hoshizaki[22] have been utilized to compute the stagnation point convective heat transfer, including the effects of dissociation and ionization. The theory is applicable to either frozen or equilibrium chemistry boundary layers and the results are correlated in terms of shock properties and the inviscid flow stagnation point velocity gradient The results of the analysis correlate closely to the existing experimental data. The blunt body wall has been assumed to be perfectly catalytic, and, for the flight velocities of interest in this study, the convective heat transfer is insensitive to the degree of non-equilibrium in the dissociated boundary layer.[22] The correlation of the numerical solutions given in Reference 22 in terms of flight conditions is accurate to $\pm 1.5\%$ in the flight velocity range of interest in this study The correlation formula in terms of stagnation point velocity gradient is given as

$$q_s(\mathrm{BTU/ft^2 sec}) = 4.32 \times 10^4 \left(\frac{U_\infty}{10{,}000}\right)^{1.69} \left[\frac{dv}{ds}\, \rho_w\, \mu_w \left(\frac{T_w}{500}\right)^{0.4}\right]^{\frac{1}{2}} \qquad (25)$$

where U_∞ is the free-stream speed in ft/sec, dv/ds is the stagnation point velocity gradient in sec^{-1}, ρ_w is the density of air at the body surface in $\mathrm{slug/ft}^3$, μ_w is the viscosity of air at the body surface in slug/sec-ft, and T_w is the body surface temperature in $^\circ$K. A body surface temperature of 300°K is assumed for the present calculations.

The heat transfer distribution around the body can be calculated by conventional boundary layer theory, as long as the appropriate boundary layer edge conditions are used.[3] For the flight conditions given in this study, the shock layer Reynolds number based on the blunt cone nose cap radius is approximately 9,000. At this Reynolds number, the boundary

layer thickness in the nose region is approximately 15% of the shock layer thickness.[1] Since the boundary layer is a significant percentage of the shock layer thickness, the proper boundary layer edge conditions differ considerably from those given by inviscid flow body properties. The magnitude of the velocity at the edge of the boundary layer is increased due to the shock curvature induced vorticity and can produce a significant increase in the convective heat transfer. The viscous and conduction effects due to velocity and temperature gradients in the shock layer, however, have a small effect on convective heat transfer at the wall and can be neglected. It should also be noted that the vehicle wall has been assumed to be cold, and the boundary layer displacement thickness and its interaction with the inviscid flow field is negligible.

Based on a transition momentum thickness Reynolds number criterion of 250, the boundary layer will be laminar for the vehicles considered in this study. The laminar heat transfer distributions have been calculated by Lees' local similarity solution.[25] The Lees' method gives the ratio of the local heat transfer at a body station to the stagnation point value as a function of the local density-viscosity product and velocity at the edge of the boundary layer. Cheng[26] and Ferri[3] have shown that, for spherical bodies at shock layer Reynolds numbers given in this study, the effect of vorticity on the laminar heat transfer distribution is approximately constant over the entire sphere cap. Thus, the inviscid body properties on the sphere-cap can be used in the method of Lees and the vorticity correction is obtained implicitly when the non-dimensionalized heat transfer distribution is multiplied by the low Reynolds number stagnation point heat transfer result.

Lees' analysis is also used to calculate the heat transfer distribution aft of the sphere-cone junction, but the inviscid properties at the edge of the boundary layer, rather than the vehicle wall, are used in the calculation. For the sphere cone cases, the edge of the boundary layer

properties in the conical region differ considerably from the inviscid body properties since the boundary layer edge extends a significant distance into the shock layer.

Ideally, the boundary layer edge properties could be obtained by coupling the boundary layer solution of Ferri et.al.[3] with the detailed inviscid flow field results obtained in this study. Such a calculation requires considerable formulation and computer programming, however, and a simplified method that is estimated to deviate less than 5% from the more exact analysis has been used. The boundary layer thickness in the conical region of the flow is assumed to be the same percentage of the shock layer thickness as the nose cap, namely 15%. The inviscid properties at this station in the shock layer correspond almost identically to the inviscid flow field properties calculated in the cells adjacent to the body. The entropy region along the body induced by the blunt bow shock is completely contained between the body and the first cell and, hence, is swallowed by the boundary layer. Thus, the inviscid flow velocities at the boundary layer edges are more closely characterized by the conical shock entropy rather than the blunt nose normal shock entropy.

2.3 RADIATIVE HEAT TRANSFER ANALYSIS

From the results of the inviscid analysis of Section 2.1 the pressure and enthalpy of the gas throughout the inviscid portion of the flow field are obtained. From this information, three operations are carried out in determining the radiative heat transfer to the vehicle surface. The gas temperature and composition are first determined by the Aeronutronic free-energy-minimization computer program at selected values of enthalpy and pressure that cover the range of these variables in the flow field. The resulting values of composition, temperature, and pressure are then used in the equilibrium radiation opacity program to obtain spectral absorption coefficients and radiation emission per unit volume. The radiation emission from each cell in the flow field is thus tabulated.

Finally the contribution of each cell to the radiation to selected points on the vehicle is computed and summed over all of the cells. In this step self-absorption is evaluated and appropriate corrections are applied. Radiation cooling corrections and radiation-viscous layer coupling corrections are then applied to obtain the final radiative heat transfer distribution.

2.3.1 EQUILIBRIUM GAS COMPOSITION

The free-energy minimization technique used at Aeronutronic to determine equilibrium gas properties has been described by Oliver, Stephanou, and Baier,[27] and is now a commonly used method. The detailed thermodynamic properties of the major species used have been tabulated by Hildenbrand,[28] and have been maintained current with the JANAF Tables. For planetary atmosphere calculations, the program includes the species C, N, O, A, C_2, N_2, O_2, CO_2, CN, CO, NO, C_3, e^-, O^-, O_2^-, A^+, C^+, O^+, N^+, C_2^+, N_2^+, O_2^+, CN^+, CO^+, NO^+, and C (solid). Multiply ionized atoms are also allowed, but are not found in significant concentration in the present calculations. The effects of vibrational anharmonicity, centrifugal stretching, and rotation-vibration coupling are included in the partition functions of the molecules. The known low-lying excited states of all species are also included. The program uses the free-energy minimization principle[27] to determine the temperature and composition for any prescribed gas enthalpy and pressure.

The heat of formation of CN is listed in the JANAF Tables as 109 Kcal/mole, corresponding to a dissociation energy of 7.5 ev. In the present calculations a value of 91 Kcal/mole was used, which corresponds to a dissociation energy of 8.2 ev. The latter value is consistent with the shock tube measurements conducted at Ames, and is consistent with the shock tube measurements of CN red emission carried out by Thomas and Menard[29] at JPL. Although some CN violet measurements[29] suggest a lower

value for the dissociation energy, the higher value has been selected for the present calculations.

The results of the Aeronutronic free-energy-minimization program have been compared with those of JPL and of Ames and are found to be in satisfactory agreement. Species concentrations differ by as much as 10 to 20% in some cases, due to differences in the thermal properties of the species that cannot be resolved on the basis of presently available information.

2.3.2 EQUILIBRIUM RADIATION EMISSION

The equilibrium radiation emission program used for the present study is described in detail in Aeronutronic reports by Bauer and Main.[30,31] The frequency-dependent absorption coefficient of CO_2-N_2 mixtures is computed over the spectral range 1000 cm^{-1} to 67,000 cm^{-1} for equilibrium temperatures from 1000°K to 10,000°K. The volume radiation emission is calculated from the absorption coefficient and the blackbody radiation function.

An extensive search for all known data on equilibrium radiation from N_2-CO_2 mixtures has been carried out specifically for the Martian entry problem. The principal sources of radiation are the electronic band systems of the diatomic and polyatomic molecules, the vibration-rotation bands, and the free-free and free-bound continuum. The techniques and data used in the program are summarized below.

a. Molecular Electronic Transitions. This mechanism contributes most of the radiation emission for the temperatures and pressures associated with significant radiative heat transfer during Martian entry. Here a diatomic or polyatomic molecule in an electronic state E', vibrational state v', and rotational state J', emits a quantum of radiation to go to a state (E", v", J"). The presence of large numbers

of different v- and J-values gives rise to the characteristic structure of these transitions or "band systems" which are usually quasi-continua at the temperatures considered here.

The model used for the band systems of diatomic molecules is called the just overlapping rotational line ("JORL") band model or the smeared rotational line band model.[32] This band model assumes the Born-Oppenheimer separation of electronic and nuclear motions in the molecule[33] and the perturbation treatment of the coupling of its vibrational and rotational degrees of freedom used in spectroscopic work.[33] A profile is assigned to each band of this system corresponding to that of the Q-branch of the band and containing all of the integrated strength of the band. While this model does not give the correct profile of each band, it does give an accurate representation of the total absorption and emission of the band system. A simple extension of this procedure is applied to polyatomic molecules, e.g., CO_2.

To compute the equilibrium radiation emission from each band system, the Franck-Condon factors and the oscillator strength are required in addition to the molecular spectroscopic constants. The Franck-Condon factors are computed using the method of Nichols[34] for those band systems which have not been computed using more rigorous methods.[35] The electronic oscillator strengths are based on published measurements or calculations wherever possible. In the absence of previously published f numbers, values have been estimated using published values for similar allowed transitions in isoelectronic molecules.[36] In other cases the qualitative rules of Mulliken and Rieke[37] are of assistance in arriving at estimates. References and values for the Franck-Condon factor arrays and the system oscillator strengths used in the radiation program are listed in Table 1.

b. Vibration-Rotation Bands. The vibration rotation bands of NO, CO, and CN contribute significantly to the radiation emission at temperatures below 3,000°K. These bands are included in the radiation program

TABLE 1

DATA FOR ELECTRONIC BAND SYSTEMS OF DIATOMIC MOLECULES IN C-N-O MIXTURES

	Band System	System Absorption f-number and References
1.	$N_2(B^3\pi_g - A^3\Sigma_u^+)$ (first positive)	0.0028[57,58]
2.	$N_2(C^3\pi_u - B^3\pi_g)$ (second positive)	0.043[59,60]
3.	$N_2(B'^3\Sigma_u^- - B^3\pi_g)$ ("Y" system)	0.002 (est)
4.	$N_2^+(B^2\Sigma_u^+ - X^2\Sigma_g^+)$ (first negative)	0.035[36,60,61]
5.	$N_2^+(A^2\pi_u - X^2\Sigma_g^+)$ (Meinel)	0.007 (est)
6.	$N_2^+(C^2\Sigma_u^+ - X^2\Sigma_g^+)$ (second negative)	0.10 (est)
7.	$N_2^+(D^2\pi_g - A^2\pi_u)$ (Janin-D'Incan)	0.005 (est)
8.	$O_2(B^3\Sigma_u^- - X^3\Sigma_g^-)$ (Schumann-Runge)	$0.17-(0.34\times10^4)/\omega$ ($\omega \geq 200000$ cm^{-1})[59]
9.	$NO(B^2\pi_r - X^2\pi_r)$ (beta)	0.0053[59]
10.	$NO(A^2\Sigma^+ - X^2\pi_r)$ (gamma)	0.0025[59,62]
11.	$NO(C^2\pi - X^2\pi_r)$ (delta)	0.017[62]
12.	$NO(D^2\Sigma^+ - X^2\pi_r)$ (epsilon)	0.014[62,63]

TABLE 1 (continued)

	Band Systems	System Absorption f-number and References
13.	$NO(E^2\Sigma^+-X^2\pi_r)$ (gamma prime)	0.01 (est)
14.	$NO(B'^2\Delta_1-X^2\pi_r)$ (beta prime)	0.01 (est)
15.	$NO(G^2\Sigma^--X^2\pi_r)$ (Lagerquist-Miescher)	0.01 (est)
16.	$NO(C^2\pi-A^2\Sigma^+)$ (Heath)	0.05 (est)
17.	$NO(D^2\Sigma^+-A^2\Sigma^+)$ (Feast 1)	0.05 (est)
18.	$NO(E^2\Sigma^+-A^2\pi)$ (Feast 2)	0.05 (est)
19.	$NO(E^2\Sigma^+-C^2\pi)$	0.05 (est)
20.	$NO(E^2\Sigma^+-D^2\Sigma^+)$ (Feast-Heath)	0.05 (est)
21.	$NO(B'^2\Delta_1-B^2\pi_r)$ (Ogawa 1)	0.001 (est)
22.	$NO(G^2\Sigma^--B^2\pi_r)$	0.001 (est)
23.	$NO(b^4\Sigma^--a^4\pi_i)$ (Ogawa 2)	0.001 (est)
24.	$NO^+(A^1\pi-X^1\Sigma^+)$ (Miescher-Baer)	0.05 (est)
25.	$CN(B^2\Sigma^+-X^2\Sigma^+)$ ("violet" system)	0.027[64,65]

TABLE 1 (continued)

	Band Systems	System Absorption f-number and References
26.	$CN(A^2\pi_i - X^2\Sigma^+)$ ("red" system)	0.007[66]
27.	$CN(D^2\pi_i - X^2\Sigma^+)$	0.005 (est)
28.	$CN(D^2\pi_i - A^2\pi_i)$	0.005 (est)
29.	$CN(F^2\Delta_r - A^2\pi_i)$	0.01 (est)
30.	$CN(E^2\Sigma^+ - A^2\pi_i)$	0.01 (est)
31.	$CN(J^2\Delta_i - A^2\pi_i)$	0.01 (est)
32.	$CN(E^2\Sigma^+ - X^2\Sigma^+)$	0.10 (est)
33.	$CN(H^2\pi_r - X^2\Sigma^+)$	0.05 (est)
34.	$C_2(A^3\pi_g - X'^3\pi_u)$ (Swan)	0.034[67,68]
35.	$C_2(A'^3\Sigma_g^- - X'^3\pi_u)$ (Ballik-Ramsay)	0.005 (est)
36.	$C_2(b^1\pi_u - x^1\Sigma_g^+)$ (Phillips)	0.0038[69]
37.	$C_2(B^3\pi_g - X'^3\pi_u)$ (Fox-Herzberg)	0.13 (est)
38.	$C_2(d^1\Sigma_u^+ - x^1\Sigma_g^+)$ (Mulliken)	0.10 (est)
39.	$C_2(e^1\Sigma_g^+ - b^1\pi_u)$ (Freymark)	0.10 (est)
40.	$C_2(c^1\pi_g - b^1\pi_u)$ (Deslandres-D'Azambuja)	0.005 (est)

TABLE 1 (continued)

	Band Systems	System Absorption f-number and References
41.	$CO(A^1\pi\text{-}X^1\Sigma^+)$ (fourth positive)	0.15[63]
42.	$CO^+(A^2\pi_i\text{-}X^2\Sigma^+)$ ("comet-tail" system)	0.0022[70]
43.	$CO^+(B^2\Sigma^+\text{-}X^2\Sigma^+)$ (first negative)	0.01 (est)
44.	$CO^+(B^2\Sigma^+\text{-}A^2\pi_i)$ (Baldet-Johnson)	0.001 (est)
45.	$CO(B^1\Sigma^+\text{-}A^1\pi)$ (Angstrom)	0.005 (est)
46.	$CO(C^1\Sigma^+\text{-}A^1\pi)$ (herzberg)	0.005 (est)
47.	$CO(a'^3\Sigma^+\text{-}a^3\pi)$ (Asundi)	0.015 (est)
48.	$CO(b^3\Sigma^+\text{-}a^3\pi)$ (Third positive)	0.009[71]
49.	$CO(d^3\Delta_i\text{-}a^3\pi)$ (Triplet)	0.015 (est)
50.	$CO(e^3\Sigma^-\text{-}a^3\pi)$ (Herman)	0.015 (est)
51.	$O_2^+(A^2\pi_u\text{-}X^2\pi_g)$ (Second negative)	0.005 (est)
52.	$O_2^+(b^4\Sigma_g^-\text{-}a^4\pi_u)$ (First Negative)	0.001 (est)

by the following simple treatment. It has been shown theoretically[38] that the integrated absorption coefficient of the fundamental system of a diatomic molecule is independent of temperature when induced emission is taken into account. This has been demonstrated to be true in experimental measurements for the NO and CO systems.[38,39] Using these data, and an estimate for CN, the average absorption coefficients over the spectral range 1,000 to 3,000 cm^{-1}, $\bar{\mu}'$ (cm^{-1}), are $13.6\gamma_{NO}P/T$, $39.4\gamma_{CO}P/T$, and $24.6\gamma_{CN}P/T$, where γ_i is the mole fraction of the species, i, P is the total gas pressure (atm) and T is the gas temperature (^{o}K).

The integrated intensity of the first overtone system of diatomic molecules has been shown to increase with increasing temperature theoretically[38] and experimentally for NO and CO.[39,40] We take the average absorption coefficients of NO, CO and CN in the spectral range 3,000 to 5,000 cm^{-1} to be

$$\bar{\mu}'(NO) = (0.000228T + 0.182)\,\gamma_{NO}P/T$$

$$\bar{\mu}'(CO) = (0.000195T + 0.0778)\,\gamma_{CO}P/T$$

$$\bar{\mu}'(CN) = 0.346[1-\exp(-2069\ hc/kT)]^{-2}[1-\exp(-4138\ hc/kT)]\gamma_{CN}P/T$$

The value for CN is an average of the measured values for NO and CO at $2,000^{o}K$, and the theoretical expression of Reference 38 is applied.

The absorption coefficients defined above are satisfactory only in computing optically thin emission Each vibration-rotation band actually consists of 50 to 100 rotational lines. All of the lines cover a spectral range that is 5 to 10% of the nominal wavelength of the band. However each rotational line covers a very narrow portion of the spectrum at the conditions of temperature and density associated with these flight calculations. The Doppler broadened linewidth is $(2\pi kT/M)^{\frac{1}{2}}/\lambda$ and is approximately 3×10^{8} cps at the stagnation point for the present flight case. Collision broadening yields a linewidth of about 10^{8} cps, contributing less than Doppler broadening. Since the Doppler linewidth represents only 10^{-6} of the nominal frequency of the vibration-rotation bands, these lines are so sharp that self-absorption is

significant even when the absorption coefficient defined above is much less (about 10^{-3}) than the reciprocal of the thickness of the shock layer. It can be seen by inspecting Tables 6 and 7 that the value of $\bar{\mu}'$ at 2000 and 4000 cm^{-1} approaches, but does not exceed the reciprocal of the shock layer thickness. Thus the infrared emission from the NO, CO, and CN bands approaches being self-absorbed. However, since the magnitude of this emission contributes less than 10% of the total radiation to the body, any errors introduced in the total radiation by the omission of self-absorption corrections in the vibration-rotation bands must be considerably less than 10%.

No provision was made to include the vibration-rotation bands of CO_2. For the equilibrium case, the concentration of CO_2 is so small that the emission is negligible. For the non-equilibrium cases, the CO_2 volume emission is appreciable immediately behind the shock prior to CO_2 dissociation, but when integrated over the shock layer it is found to be negligible in comparison with the integrated emission due to the CN red and CN violet bands.

c. Continuum Emission. Continuum emission due to free-free transitions is computed using the classical Kramers formula[41] for the linear spectral absorption coefficient,

$$\mu'_\omega = 0.738\times10^{21} z_{eff}^2 \frac{\gamma_e \gamma_1 P^2}{\omega^3 T^{5/2}} \left[1-\exp(-hc\omega/kT)\right]$$

which includes allowance for stimulated emission. The species γ_1 is taken here to be either the totality of all positively charged singly ionized atoms and molecules for which we take $z_{eff}^2 = 1$, or the totality of all electrically neutral atoms and molecules, for which we take $z_{eff}^2 = 0.01$ following Keck, Allen and Taylor.[42] The continuum emission from free-bound transitions is determined by using the hydrogenic cross sections for recombination as computed by Bates.[43] The continuum emission is appreciable for CO_2-N_2 mixtures only when the equilibrium temperature exceeds 8,000 to 10,000°K.

2.3.3 SELF-ABSORPTION OF EQUILIBRIUM RADIATION

For equilibrium calculations, self-absorption corrections to the radiative heat transfer are made in two different ways. For bands such as CO(4+) that are very optically thick a blackbody upper limit is set at each wavelength by utilizing the temperature of the shock layer gas at a normal distance of one absorption length from the body surface. The absorption length for each wavelength is printed out directly from the equilibrium radiation program. The blackbody limits at each wavelength are then summed over all wavelengths.

For intermediate optical depth the following model is used to make self-absorption corrections to the radiative heat transfer. The spectral emission (neglecting self-absorption) is computed and integrated progressively from the body surface in each direction defined in Paragraph 2.3.6. Simultaneously the non-equilibrium absorption optical depth is integrated. At a point where the absorption optical depth reaches a value of one, the integration of the optically thin emission is terminated; the total emission thus accumulated closely approximates the net spectral radiative flux with self-absorption.

2.3.4 RADIATION-INVISCID FLOW COUPLING

This is negligible in the equilibrium sphere-cone case and is therefore not included. The radiation cooling of the inviscid fluid by the time it reaches the boundary layer edge adjacent to the stagnation point reduces the enthalpy by about 1% and reduces the total radiation emission by less than 1%.

2.3.5 RADIATION-VISCOUS LAYER COUPLING

Radiation-viscous layer coupling is included by subtracting from the total radiation a contribution from a uniform slab of thickness equal to the thermal boundary layer thickness, defined by a 5% reduction in enthalpy below the value just outside the boundary layer. The radiative properties of the slab were taken to be those in the cell nearest the body. The additional effect of radiation absorption by the boundary layer gas is negligible, because the enthalpy flux through the boundary layer gas is much greater than the radiation absorbed in the boundary layer.

2.3 6 GEOMETRIC INTEGRATION

The radiative properties of the shock layer gas determined from the equilibrium radiation emission program are used in a geometrical integration program to compute the radiative flux to various points on the vehicle surface. For a given point on the body, the shock layer is divided into slabs as shown in Figure 8. These slabs have their normal coincident with the normal to the body through the body point for which the radiative heat transfer is being computed. In the present computation three slabs of equal thickness were used between the body and the shock.

Each slab is divided into rings that subtend equal solid angles from the body point. Each ring in each slab thus contributes equally to the flux to the body point if the radiative properties throughout the slabs are uniform. However, because of the shock curvature, the outermost slab is only partially filled with radiating gas. Furthermore, the shock layer properties are not uniform These two effects are included by summing the radiative contributions from segments of each ring. The contribution from each segment is based on an average radiating volume determined from the geometry of the slabs and the shock layer, and an average radiation emission per unit volume from the segment. The summation of these contributions gives the total radiative flux to the surface. In the present computations each slab was divided into five

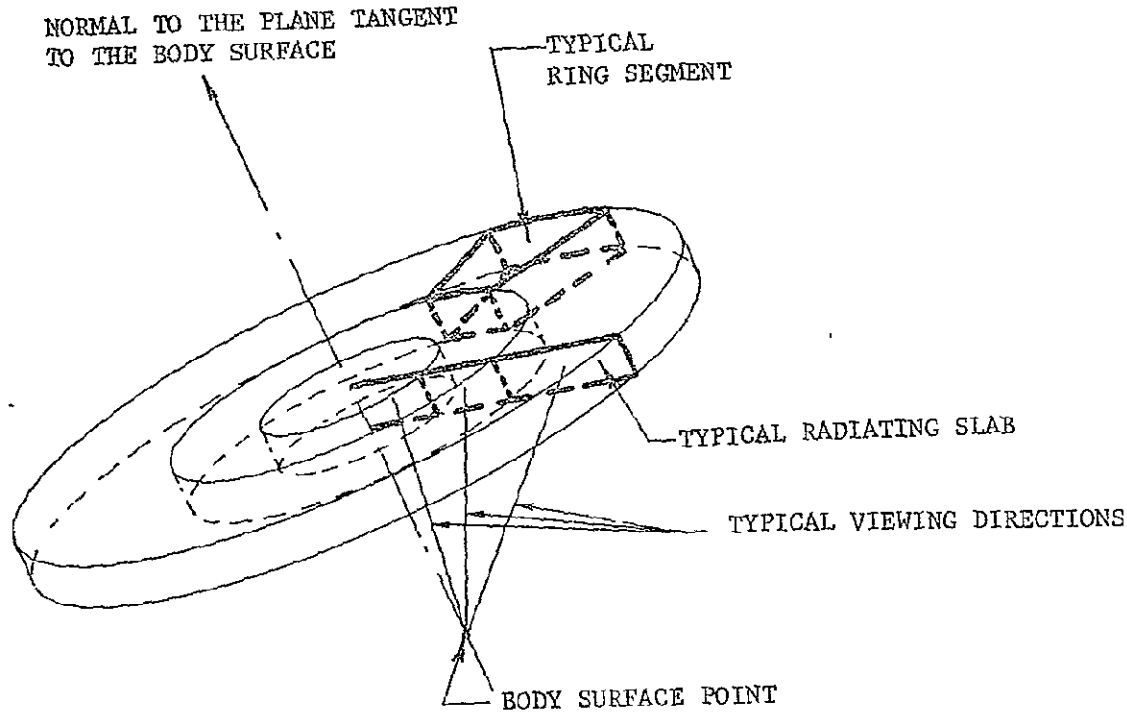

FIGURE 8. GEOMETRY USED IN CARRYING OUT THE VOLUME INTEGRATION OF SHOCK LAYER RADIATIVE HEAT TRANSFER TO SELECTED BODY LOCATIONS

rings, the first two nearest the normal subtending one half the solid angle subtended by the other three. The angles used to compute average radiative properties were 14.5^{o}, 35.25^{o}, 50.75^{o}, 67.75^{o}, and 82.75^{o}.

2.3.7 COLLISION LIMITING

It has been found from the non-equilibrium studies of Section 3.2 that the equilibrium CN violet emission may be reduced by as much as a factor of 2 for the conditions of the present calculations. The other significant sources of radiation do not appear to be affected. However because of the uncertainty in this factor, and because it has not been corroborated by experimental measurements, no correction for collision limiting is made to the equilibrium radiation calculations.

SECTION 3

NON-EQUILIBRIUM FLOW

The flow field analysis used for non-equilibrium conditions is much the same as that used for equilibrium conditions, described in Section 2. The inviscid properties are computed assuming a thin viscous layer, and are then corrected for coupling between the inviscid and viscous regions. The convective heating and radiative heating are then calculated with the use of the uncoupled inviscid results, corrected for radiation cooling and viscous-inviscid coupling.

3.1 INVISCID ANALYSIS

In the inviscid region the flow equations are decoupled from the reaction rate equations by including an ideal gas equation of state in the flow equations. This separation permits an effective γ to be used which is determined through the results of an integration of the reaction rate equations along the stagnation streamline. The variation of γ along the stagnation streamline is found to be representative of that along other normals between the body and the shock throughout the subsonic flow region in the shock layer. In this way the equation of state differs little from that obtained from a rigorous solution of the flow equations coupled with the reaction rate equations. In the present calculations

the γ variation noted above was approximated by a constant value since the variation in γ is not large across the shock layer.

The results of integrating the flow equations with the approximate equation of state are used only to provide the pressure field and the streamline positions. The remaining gas properties are determined by solving the reaction rate equations along with Euler's equation, and the equations of state, on selected streamlines. The errors introduced by this procedure are small since the pressure field and streamline positions are insensitive to non-equilibrium chemistry effects.

In the constant γ flow field solution, the conservation Equations (1)-(5) are solved by the same method used for equilibrium flow (Section 2.1). The thermal and caloric equations of state are different, however, and for constant γ combine to give

$$p = (\gamma-1)\rho e \tag{26}$$

which is used in place of Equation (8).

The streamline positions within the shock layer are determined by locating points of constant stream function, ψ, which by definition are points on a given streamline. Lines of constant stream function were calculated from an integral solution of the continuity equation utilizing the density and velocity profiles obtained from the inviscid shock layer solution.

The non-equilibrium chemistry calculation is initiated at the bow shock wave. Across the bow shock the rotation and the vibration internal energy modes are assumed to be fully equilibrated with translation, while the chemical species are assumed to be frozen at the free stream conditions. The γ utilized in the inviscid flow field solution corresponds to a 70% N_2, 30% CO_2 mixture with equilibrium internal energy modes and frozen free-stream chemistry. Thus, the initial conditions for p, ρ, T, q, γ_j and E_{v_j}

behind the bow shock to start the non-equilibrium species calculation are given by the inviscid solution. With the pressure and streamline field given, the remaining five unknown shock layer properties, ρ, T, q, γ_j, and E_{v_j} are determined from the simultaneous solution of the following five equations:

Euler Equation

$$\frac{dq}{dz} = \frac{-k}{\rho q}\frac{dp}{dz} \tag{27}$$

Integral Energy Equation and the Caloric Equation of State

$$T = \frac{\frac{1}{2k}(1-q^2) - \sum_{j=1}^{s}(\gamma_j-\gamma_{j\infty})h_j^o - \sum_{c+1}^{f}\gamma_j(n_j-1)E_{v_j}}{\sum_{I}^{s}\gamma_j(1.5+n_j)} \tag{28}$$

Thermal Equation of State

$$\rho = \frac{P}{(T\sum_{I}^{s}\gamma_j)} \tag{29}$$

Species Conservation Equation

$$q\frac{d\gamma_j}{dz} = \sum_{i=1}^{s}\frac{Q_{ij}}{\rho} \tag{30}$$

where

$$\frac{Q_{ij}}{\rho} = \beta_{ij}(C\rho)^{\nu_{i-1}}\prod\gamma_\alpha^{\nu_{i\alpha}}\left[1 - \frac{1}{K_i}(C\rho)^{\beta_i}\prod_{\alpha=1}^{s}\gamma_\alpha^{\beta_{i\alpha}}\right]$$

$$\beta_{ij} \equiv \nu'_{i\alpha} - \nu_{i\alpha} .$$

$$\nu_i = \sum_{\alpha=1}^{s} \nu_{i\alpha}$$

$$\beta_i = \sum_{\alpha=1}^{s} \beta_{i\alpha}$$

Equilibrium Vibration Energy Equation

$$E_v = RT\left[\bar{u}(e^{\bar{u}}-1)^{-1} + \frac{u_o}{\bar{u}}\right] \tag{31}$$

where $\bar{u} = \frac{\theta_v}{T}$ and the constants u_o and θ_v are given in Table 2.

3.2 NON-EQUILIBRIUM PROPERTIES OF PLANETARY ATMOSPHERES

An extensive compilation of non-equilibrium processes in CO_2, N_2, A mixtures is included in the Aeronutronic non-equilibrium computer program, specifically for Martian entry calculations. The program includes the processes normally included in all such programs: molecular rotation and vibration, dissociation, ionization, and atom, ion, and charge transfer. In addition, careful consideration has been given to the most important process for computing radiative heat transfer, that of non-equilibrium excited state production.

The non-equilibrium properties of the flow field are obtained from a streamtube integration program which utilizes the pressure field and the streamline locations determined from the flow field integration (Section 3.1). The streamtube program integrates the energy and Euler equations, and the species and excited state rate equations to obtain the chemical composition, the gas density, and the temperature.

The details of the program and the non-equilibrium data used in it are summarized below. The species included in the program are C, N, O, C_2, N_2, O_2, CO_2, CO, CN, NO, C^+, N^+, O^+, C_2^+, N_2^+, O_2^+, CO^+, CN^+, NO^+, e^-, CN*, N_2*, and CO*. The number of reactions included is 31 for pure CO_2, 93 for N_2-CO_2 mixtures, and 27 for air.

TABLE 2

MOLECULAR VIBRATION AND DISSOCIATION CONSTANTS

Molecule	θ_v °K			u_o	D_j, kcal/mole	Refs.
CO_2	$\theta_1 = 1950$	$\theta_2 = 966$	$\theta_3 = 3445$	0	126 (to CO + O)	72,73
CO		3067		.029	256	33
N_2		3337		.032	225	33
O_2		2228		.039	118	33
C_2		2322		.032	140	33,74
CN		2924		.030	172	33,75
NO		2688		.037	150	33

The reaction rate constants are based on an extensive survey of available experimental data. However there are a number of reactions which contribute significantly to the non-equilibrium properties of the flow, for which there is no data available. For these reactions the best methods available have been used to estimate rate constants. The basis for these estimates and the values used in the program are discussed below. The reactions are divided into nine groups, which are identified as rotation relaxation, vibration relaxation, molecular dissociation and atom recombination, atom exchange, neutral atom transfer, electronic excitation, ion production and loss, and ion and charge transfer. The data used in the non-equilibrium program are given here in detail because they are not yet available elsewhere.

3.2.1 REACTION RATE DATA

a. Rotation Relaxation. Rotation is assumed to be fully equilibrated with translation, as has been observed in low density shock thickness studies in CO_2[44] and O_2.[45] The rotational contribution to the heat capacity is RT for all molecules, including CO_2.

b. Vibration Relaxation. For normal shocks above V_∞ = 4.5 km/sec, CO_2 and O_2 vibrational modes are fully relaxed within the translation-rotation shock.[44,45] Vibration relaxation times for N_2 and CO are within a factor of 5 of that for O_2 above 8000°K. Furthermore N_2 vibration is in resonance with the ν_3 mode of CO_2 and will relax even faster in CO_2-N_2 mixtures. Thus for normal shock speeds above 4.5 km/sec vibration is fully relaxed within or very close to the translation-rotation shock, and can be assumed to be fully equilibrated with translation. This applies as well to oblique shocks with a normal component of speed greater than 4.5 km/sec.

The equilibrium vibrational energy is obtained from the spectroscopically determined vibrational constants by $E_v = RT[\bar{u}(e^{\bar{u}} - 1)^{-1} + u_o/\bar{u}]$ where $\bar{u} = \theta_v/T$, (see Reference 46). Values for θ_v and u_o are given in Table 2.

Only the vibrations of the neutral species CO_2, CO, N_2, O_2, C_2, CN, and NO are considered to contribute to the gas heat capacity. The special case of CO_2, having 4 vibrational modes (2 modes at 1 frequency, ν_2), is treated by uncoupled superposition of each mode, neglecting the effects of anharmonicity (u_o) since the constants χ and γ are quite small for CO_2. Because the ν_2 (bending) mode is doubly degenerate it contributes $E_{v_{\nu_2}} = 2RT[u(e^u - 1)^{-1}]$ to the heat capacity.

c. Molecular Dissociation and Atom Recombination. Dissociation of the neutral molecules is included, since these cause the major change in gas temperature. In addition dissociation of the excited electronic states, CN*, CO*, and N_2* is included, since dissociation strongly affects the concentration of these species. Certain rates are estimated because of the lack of experimental data. This is done by assuming that molecules with paired electrons (O_2, N_2, C_2, CO, and CO_2) are less efficient in causing vibrational energy transfer near the dissociation limit than are molecules with unpaired electrons (NO and CN) and free atoms (C, N, and O). The former group is denoted by M_1, the latter by M_2. These rate constants are defined for a reaction of the form $A + A + M \rightarrow A_2 + M$ by $d[A_2]/dt = -1/2\ d[A]/dt = k_f[A]^2[M]$. The reactions and the rate constants used in the Aeronutronic computer program are given as 1 through 14 in Table 3.

d. Atom Exchange. The atom exchange reactions are generally slow and exhibit a high activation energy even for exothermic reaction rates. Because of this, estimates cannot easily be made. Thus only those reactions for which data exist are included. These rate constants are defined for a reaction of the form $AB + AB \rightarrow A_2 + B_2$ by $d[A_2]/dt = -1/2\ d[AB]/dt = k_f[AB]^2$. The reaction and rate constant used is given as 15 in Table 3.

e. Neutral Atom Transfer. The atom transfer reactions are generally fast and exhibit small (if any) activation energy for the exothermic reaction rates. Only a few of these reaction rates have been measured. All

TABLE 3

REACTION RATE SYSTEM FOR C-N-O MIXTURES

	Reaction	Forward Rate Constant, cm^3/mole-sec	Ref	Equilibrium Constant
1.	$CO_2 + M_1 \rightarrow CO + O + M_1$	$0.116\times10^{12}T^{0.5}\exp(-34{,}300/T)$	76	$0.41\times10^{8}T^{-1.45}\exp(-63{,}000/T)$
2.	$CO_2 + M_2 \rightarrow CO + O + M_2$	$3\ k_1$	est	K_1
3.	$O + O + M_1 \rightarrow O_2 + M_1$	$0.80\times10^{20}T^{-1.5}$	77	$0.64\times10^{-5}T^{1.0}\exp(62{,}419/T)$
4.	$O + O + M_2 \rightarrow O_2 + M_2$	$2.75\ k_3$	77	K_3
5.	$N + N + M_1 \rightarrow N_2 + M_1$	$0.22\times10^{17}T^{-0.5}$	78	$0.91\times10^{3}T^{-1.0}\exp(107{,}365/T)$
6.	$N + N + M_2 \rightarrow N_2 + M_2$	$0.22\times10^{22}T^{-1.5}$	78	K_5
7.	$N + O + M_1 \rightarrow NO + M_1$	$0.40\times10^{21}T^{-1.5}$	est	$0.39\times10^{2}T^{-0.5}\exp(71{,}673/T)$
8.	$N + O + M_2 \rightarrow NO + M_2$	$7.5\ k_7$	79	K_7
9.	$C + O + M_1 \rightarrow CO + M_1$	$0.30\times10^{19}T^{-1.0}$	80	$0.23\times10^{-3}T^{0.5}\exp(131{,}119/T)$
10.	$C + O + M_2 \rightarrow CO + M_2$	$10\ k_9$	est	K_9
11.	$C + N + M_1 \rightarrow CN + M_1$	0.25×10^{15}	est	$0.27\exp(92{,}400/T)$
12.	$C + N + M_2 \rightarrow CN + M_2$	$6\ k_{11}$	est	K_{11}
13.	$C + C + M_1 \rightarrow C_2 + M_1$	$0.20\times10^{17}T^{-0.5}$	est	$0.23\exp(66{,}691/T)$
14.	$C + C + M_2 \rightarrow C_2 + M_2$	$3\ k_{13}$	est	K_{13}
15.	$NO + NO \rightarrow N_2 + O_2$	$0.23\times10^{24}T^{-2.5}\exp(-43{,}000/T)$	77	K_3K_5/K_7^2
16.	$CO + O_2 \rightarrow CO_2 + O$	$0.10\times10^{12}T^{0.5}$	est	$1/K_1K_3$

TABLE 3 (continued)

Reaction	Forward Rate Constant, cm^3/mole-sec	Ref	Equilibrium Constant
17. $C_2 + O \rightarrow CO + C$	$0.50\times10^{12}T^{0.5}$	est	K_9/K_{13}
18. $O_2 + C \rightarrow CO + O$	$0.50\times10^{12}T^{0.5}$	est	K_9/K_3
19. $CN + O \rightarrow CO + N$	$0.10\times10^{13}T^{0.5}$	est	K_9/K_{11}
20. $NO + C \rightarrow CO + N$	$0.25\times10^{12}T^{0.5}$	est	K_9/K_7
21. $O_2 + N \rightarrow NO + O$	$0.13\times10^{11}T^{1.0}\exp(-3560/T)$	77	K_7/K_3
22. $CN + N \rightarrow N_2 + C$	$0.125\times10^{12}T^{0.5}$	est	K_5/K_{11}
23. $NO + N \rightarrow N_2 + O$	0.16×10^{14}	77	K_5/K_7
24. $NO + C \rightarrow CN + O$	$0.125\times10^{12}T^{0.5}$	est	K_{11}/K_7
25. $C_2 + N \rightarrow CN + C$	$0.50\times10^{12}T^{0.5}$	est	K_{11}/K_{13}
26. $N + O \rightarrow NO^+ + e^-$	$0.75\times10^{14}T^{-0.5}\exp(-31,900/T)$	24	$0.66\times10^{-7}T^{1.0}\exp(-35,993/T)$
27. $O + O \rightarrow O_2^+ + e^-$	$0.50\times10^{14}T^{-0.5}\exp(-82,300/T)$	24	$0.38\times10^{-13}T^{2.5}\exp(-76,387/T)$
28. $N + N \rightarrow N_2^+ + e^-$	$0.15\times10^{15}T^{-0.5}\exp(-67,500/T)$	24	$0.31\times10^{-6}T^{1.0}\exp(-74,051/T)$
29. $C + N \rightarrow CN^+ + e^-$	$0.80\times10^{14}T^{-0.5}\exp(-69,600/T)$	est	$0.42\times10^{-6}T^{1.0}\exp(-84,122/T)$
30. $C + O \rightarrow CO^+ + e^-$	$0.27\times10^{14}T^{-0.5}\exp(-33,600/T)$	est	$0.32\times10^{-13}T^{2.5}\exp(-29,370/T)$
31. $C + C \rightarrow C_2^+ + e^-$	$0.80\times10^{14}T^{-0.5}\exp(-68,600/T)$	est	$0.30\times10^{-6}T^{1.0}\exp(-75,950/T)$
32. $O^+ + NO \rightarrow O_2^+ + N$	$0.25\times10^{12}T^{0.5}$	est	$0.29\times10^{-6}T^{1.5}\exp(9437/T)$

TABLE 3 (continued)

Reaction	Forward Rate Constant, cm^3/mole-sec	Ref	Equilibrium Constant
33. $O^+ + N_2 \rightarrow NO^+ + N$	$0.50\times10^{12}T^{0.5}$	est	$K_{26}K_{32}/K_{23}K_{27}$
34. $N + N_2^+ \rightarrow N_2 + N^+$	$0.25\times10^{12}T^{0.5}$	est	$0.53\times10^{4}T^{-1.0}\exp(11,113/T)$
35. $O^+ + O_2 \rightarrow O_2^+ + O$	$0.50\times10^{12}T^{0.5}$	est	$K_{21}K_{32}$
36. $N^+ + NO \rightarrow N_2^+ + O$	$0.25\times10^{12}T^{0.5}$	est	K_{23}/K_{34}
37. $O^+ + NO \rightarrow NO^+ + O$	$0.25\times10^{12}T^{0.5}$	est	$K_{23}K_{33}$
38. $N^+ + O_2 \rightarrow O_2^+ + N$	$0.50\times10^{12}T^{0.5}$	est	$K_5K_{27}/K_3K_{28}K_{34}$
39. $C + O_2^+ \rightarrow CO^+ + O$	$0.25\times10^{12}T^{0.5}$	est	K_{30}/K_{27}
40. $C^+ + O_2 \rightarrow CO^+ + O$	$0.50\times10^{12}T^{0.5}$	est	$0.45\times10^{+5}T^{-1.0}\exp(24,943/T)$
41. $O + CO^+ \rightarrow CO + O^+$	$0.25\times10^{12}T^{0.5}$	est	$K_{18}/K_{35}K_{39}$
42. $O^+ + CN \rightarrow CO^+ + N$	$0.25\times10^{12}T^{0.5}$	est	K_{19}/K_{41}
43. $O + CN^+ \rightarrow CO^+ + N$	$0.125\times10^{12}T^{0.5}$	est	K_{30}/K_{29}
44. $C^+ + NO \rightarrow CO^+ + N$	$0.25\times10^{12}T^{0.5}$	est	K_{40}/K_{21}
45. $N + CO^+ \rightarrow NO^+ + C$	$0.125\times10^{12}T^{0.5}$	est	K_{26}/K_{30}
46. $O^+ + C_2 \rightarrow CO^+ + C$	$0.50\times10^{12}T^{0.5}$	est	K_{17}/K_{41}
47. $C + CO^+ \rightarrow CO + C^+$	$0.125\times10^{12}T^{0.5}$	est	K_{20}/K_{44}
48. $O + C_2^+ \rightarrow CO^+ + C$	$0.25\times10^{12}T^{0.5}$	est	K_{31}/K_{32}

TABLE 3 (continued)

Reaction	Forward Rate Constant, cm^3/mole-sec	Ref	Equilibrium Constant
49. $O + C_2^+ \rightarrow CO + C^+$	$0.25 \times 10^{12} T^{0.5}$	est	$K_{18}K_{48}/K_{40}$
50. $C + CN^+ \rightarrow C_2^+ + N$	$0.125 \times 10^{12} T^{0.5}$	est	K_{31}/K_{29}
51. $N + C_2^+ \rightarrow CN + C^+$	$0.25 \times 10^{12} T^{0.5}$	est	K_{49}/K_{19}
52. $C + C_2^+ \rightarrow C_2 + C^+$	$0.25 \times 10^{12} T^{0.5}$	est	K_{51}/K_{25}
53. $O + CN^+ \rightarrow CO + N^+$	$0.125 \times 10^{12} T^{0.5}$	est	$K_{18}K_{27}/K_{29}K_{38}$
54. $O + CN^+ \rightarrow NO^+ + C$	$0.125 \times 10^{12} T^{0.5}$	est	K_{26}/K_{29}
55. $O + CN^+ \rightarrow NO + C^+$	$0.125 \times 10^{12} T^{0.5}$	est	$K_{21}K_{43}/K_{40}$
56. $N^+ + CN \rightarrow CN^+ + N$	$0.25 \times 10^{12} T^{0.5}$	est	K_{19}/K_{53}
57. $N + CN^+ \rightarrow N_2^+ + C$	$0.125 \times 10^{12} T^{0.5}$	est	K_{28}/K_{29}
58. $N + CN^+ \rightarrow N_2 + C^+$	$0.125 \times 10^{12} T^{0.5}$	est	$K_5K_{50}K_{52}/K_{13}$
59. $N^+ + C_2 \rightarrow CN^+ + C$	$0.50 \times 10^{12} T^{0.5}$	est	$K_{25}K_{56}$
60. $C + CN^+ \rightarrow CN + C^+$	$0.125 \times 10^{12} T^{0.5}$	est	K_{58}/K_{22}
61. $N + O_2^+ \rightarrow NO^+ + O$	$0.25 \times 10^{12} T^{0.5}$	est	K_{26}/K_{27}
62. $N^+ + O_2 \rightarrow NO^+ + O$	$0.50 \times 10^{12} T^{0.5}$	est	$K_{38}K_{61}$
63. $N^+ + NO \rightarrow NO^+ + N$	$0.25 \times 10^{12} T^{0.5}$	est	K_{62}/K_{21}
64. $O + N_2^+ \rightarrow NO^+ + N$	$0.25 \times 10^{12} T^{0.5}$	est	K_{26}/K_{28}
65. $O^+ + CN \rightarrow NO^+ + C$	$0.25 \times 10^{12} T^{0.5}$	est	K_{37}/K_{24}

TABLE 3 (continued)

Reaction	Forward Rate Constant, $cm^3/mole\text{-}sec$	Ref	Equilibrium Constant
66. $N^+ + CO \rightarrow NO^+ + C$	$0.25\times10^{12}T^{0.5}$	est	K_{62}/K_{18}
67. $N^+ + CN \rightarrow N_2^+ + C$	$0.25\times10^{12}T^{0.5}$	est	K_{22}/K_{34}
68. $C + O_2^+ \rightarrow CO + O^+$	$0.25\times10^{12}T^{0.5}$	est	K_{18}/K_{35}
69. $N + N_2 \rightarrow N_2^* + N$	$0.114\times10^{19}T^{-1.5}\exp(-71,600/T)$	50	$0.68\exp(-71,600/T)$
70. $N + CN \rightarrow N_2^* + C$	$0.57\times10^{18}T^{-1.5}\exp(-53,400/T)$	est	$K_{22}K_{69}$
71. $N + NO \rightarrow N_2^* + O$	$0.57\times10^{18}T^{-1.5}\exp(-33,800/T)$	est	$K_{23}K_{69}$
72. $C + CO \rightarrow CO^* + C$	$0.57\times10^{18}T^{-1.5}\exp(-69,700/T)$	est	$0.86\exp(-69,700/T)$
73. $O + CO \rightarrow CO^* + O$	$0.57\times10^{18}T^{-1.5}\exp(-69,700/T)$	est	K_{72}
74. $C + O_2 \rightarrow CO^* + O$	$0.25\times10^{12}T^{0.5}$	est	$K_{18}K_{72}$
75. $O + C_2 \rightarrow CO^* + C$	$0.25\times10^{12}T^{0.5}\exp(-11,400/T)$	est	$K_{17}K_{72}$
76. $C + CN \rightarrow CO^* + N$	$0.30\times10^{15}T^{-0.5}\exp(-16,100/T)$	est	$K_{20}K_{72}$
77. $O + CN \rightarrow CO^* + N$	$0.30\times10^{15}T^{-0.5}\exp(-27,800/T)$	est	$K_{19}K_{72}$
78. $C + CO_2 \rightarrow CO^* + CO$	$0.25\times10^{12}T^{0.5}\exp(-4600/T)$	est	K_{72}/K_{16}
79. $N_2^* + CO \rightarrow CO^* + N_2$	$0.50\times10^{12}T^{0.5}$	est	K_{72}/K_{69}
80. $C + O + M_1 \rightarrow CO^* + M_1$	$0.50\times10^{19}T^{-1.0}$	est	K_9K_{72}
81. $C + O + M_2 \rightarrow CO^* + M_2$	$0.20\times10^{20}T^{-1.0}$	est	K_{80}

TABLE 3 (continued)

Reaction	Forward Rate Constant, cm^3/mole-sec	Ref	Equilibrium Constant
82. N $N + M_1 \rightarrow N_2^* + M_1$	$0.104 \times 10^{18} T^{-015}$	est	$K_5 K_{69}$
83. $N + N + M_2 \rightarrow N_2^* + M_2$	$0.48 \times 10^{22} T^{-1.5}$	est	K_{82}
84. $C + N + M_1 \rightarrow CN^* + M_1$	0.25×10^{15}	est	$K_{11} K_{86}$
85. $C + N + M_2 \rightarrow CN^* + M_2$	0.15×10^{16}	est	K_{85}
86. $N + CN \rightarrow CN^* + N$	$0.384 \times 10^{16} T^{-0.5} \exp(-36,900/T)$	est	$1.08 esp(-36,900/T)$
87. $C + CN \rightarrow CN^* + C$	k_{86}	est	K_{86}
88. $N + CO \rightarrow CN^* + O$	$0.57 \times 10^{18} T^{-1.5} \exp(-68,800/T)$	est	K_{86}/K_{19}
89. $N + CO^* \rightarrow CN^* + O$	$0.35 \times 10^{15} T^{-0.5} \exp(-900/T)$	est	K_{88}/K_{72}
90. $C + N_2 \rightarrow CN^* + N$	$0.114 \times 10^{19} T^{-1.5} \exp(-53,800/T)$	est	K_{86}/K_{22}
91. $N + C_2 \rightarrow CN^* + C$	$0.10 \times 10^{15} T^{-0.5} \exp(-11,300/T)$	est	$K_{25} K_{86}$
92. $N + CN^* \rightarrow N_2^* + C$	$0.10 \times 10^{15} T^{-0.5} \exp(-17,800/T)$	est	K_{69}/K_{90}
93. $C + NO \rightarrow CN^* + O$	$0.10 \times 10^{15} T^{-0.5} \exp(-16,00/T)$	est	K_{24}/K_{86}

possibilities are included in Table 3, and are written in exothermic form. Four possibilities were excluded because of spin conservation requirements or geometrical configuration. These are $C_2 + O_2 \rightarrow CO_2 + C$, $CO_2 + C \rightarrow CO + CO$, $CN + O_2 \rightarrow CO_2 + N$, and $CO_2 + N \rightarrow CO + NO$.

The basic estimated rate constant used here is $5 \times 10^{11} T^{\frac{1}{2}}$ cm^3/mole-sec, or about 1/6 the gas kinetic value. Many of the reactions considered can go to a number of different products, for example NO + C goes to either CO + N or CN + O. The estimated rate constants for such reactions are chosen to be smaller than the basic value by a factor equal to the number of possible sets of products. The reactions and rate constants used are given as 16 through 25 in Table 3.

Two of the reaction rates listed above are an additional factor of 2 and 5 slower, respectively, than the original estimate; a second is an additional factor of 4 faster. This was done to improve the comparison between computed and measured values for non-equilibrium radiation (see Section 3.2.4).

f. Ion Production and Loss. In air the rate of production of molecular ions behind strong shock waves is predicted satisfactorily by including only the associative ionization reactions, i.e., $A + B \rightarrow AB^+ + e^- + M$. Because of the lack of knowledge concerning molecular impact ionization, i.e., $A_2 + M \rightarrow A_2^+ + e^- + M$, this process is neglected here. Similarly electron impact ionization is neglected because of the uncertainty in electron temperature. If the analysis carried out for monatomic gases is used,[47] the electron impact rate is slower than the associative ionization rate for normal shock speeds up to 9 km/sec. Too little information is available on the electron temperature in an ionizing diatomic gas; hence the electron impact ionization process is neglected here. The rate constant is defined for reactions of the form $A + A \rightarrow A_2^+ + e^-$ by $d[A_2^+]/dt = -1/2\ d[A]/dt = k_f[A]^2$. The reactions and rate constants used are given as 26 through 31 in Table 3.

g. Ion and Charge Transfer. In a three atom system there is a multitude of possible ion and charge transfer reactions involving atomic or molecular ions. Unfortunately none of these has been measured at low energies and we must rely on estimates. Only binary reactions involving one ion and one neutral are included here: reactions involving 2 ions are much less frequent because of the generally low degree of ionization.

Most direct charge transfer reactions exhibit an appreciable energy defect and, based on higher energy measurements,[48] are expected to be much slower than gas kinetic. In a careful evaluation of the energy defect in direct charge transfer reactions in the C, N, O system, including low excited electronic levels, only two reactions were found which showed a sufficiently small energy defect (< 0.2 ev) to be considered near-resonant. However ion charge is readily passed around through atom transfer reactions involving atomic or molecular ions for which there is no restriction on reaction rate other than the gas kinetic upper limit for exothermic reactions. The basic estimated rate constant used for these reactions is $5 \times 10^{11} T^{\frac{1}{2}}$ cm^3/mole-sec, or about 1/6 the gas kinetic value, reduced by the number of possible sets of products. The reactions and rate constants used are given as 32 through 68 in Table 3.

h. Electronic Excitation. The low electronic states (up to 2.5 ev) of all molecules and atoms are assumed to be in equilibrium with the ground states at the local translational temperature. This is justified on the basis that there are no known low excited states of N_2 or CO_2 or A and that the low excited states of newly formed atoms and molecules are produced as rapidly as the ground states. Since some of these low excited states contribute appreciably to the heat capacity the required data is given in Table 4.

The excitation mechanism of the electronic states is not well understood, but C_2 and CN impurity radiation is frequently observed immediately behind the shock front in noble gas shock tube experiments, long before

TABLE 4

FACTOR BY WHICH THE INTERNAL ENERGY IS INCREASED
DUE TO EXCITATION OF LOW ELECTRONIC STATES

Species	Factor
CO_2	1
N_2	1
O_2	$1 + \dfrac{\frac{2}{3}(\frac{11,390}{T})\exp(-11,390/T) + \frac{1}{3}(\frac{18,990}{T})\exp(-18,990/T)}{1 + \frac{2}{3}\exp(-11,390/T) + \frac{1}{3}\exp(-18,990/T)}$
C_2	$1 + \dfrac{(\frac{27,750}{T})\exp(-27,750/T)}{1 + \exp(-27,750/T)}$
NO	1
CO	1
CN	$1 + \dfrac{2(\frac{13,300}{T})\exp(-13,300/T)}{1 + 2\exp(-13,300/T)}$
N	$1 + \dfrac{2.5(27,700/T)\exp(-27,700/T)}{1 + 2.5\exp(-27,700/T)}$
O	$1 + \dfrac{.555(\frac{22,850}{T})\exp(-22,850/T)}{1 + .555\exp(-22,850/T)}$
C	$1 + \dfrac{.555(14,650/T)\exp(-14,650/T)}{1 + .555\exp(-14,650/T)}$

excitation or ionization of the noble gas is seen. This indicates that the rate of excitation of low electronic levels of molecules by neutral impact is very high. Large cross-sections have been observed for quenching of upper electronic states by neutral impact,[49] indicating high excitation rates for levels requiring only small electronic energy changes. This is extrapolated to low electronic levels of molecules, which require no change in total spin, by recognizing that the energy defect can be supplied through vibrational excitation of the molecule. Atoms in low excited states are then produced by atom transfer reactions. Low electronic states of molecules which require a change in electronic spin may be excited primarily by free atom impact exchange reactions, as found for the high electronic levels of N_2.[50] Because most of the low electronic levels significant in radiation heating by the CNO system involve no spin change from the ground state, it was originally planned that the quasi-equilibrium assumption would be used. However, it was found that the results of this assumption did not fit the experimental data on CN violet emission. Subsequently a finite rate of production of the $B^2\Sigma^+$ state of CN was introduced into the reaction rate system.

In addition, the upper levels of N_2 and CO, which require a change in spin from those of the ground states, cannot be assumed to be in equilibrium with the ground states. The only direct experimental evidence available[50] is for the reaction $N + N_2 \rightarrow N_2^* + N$ for which $k = 1.14 \times 10^{18} T^{-3/2} \exp(-71,600/T)$ cm^3/mole-sec. This rate constant was found[50] to be at least 100 times higher than that for the reaction $N_2 + N_2 \rightarrow N_2^* + N_2$. It is not known if other free atoms, O for example, will cause electronic excitation of N_2, even though a direct atom transfer does not occur, but it is assumed here that they will not. In making estimates, all atom transfer reactions which can produce excited N_2 or CO without violating the spin conservation rule are assumed to be at least as effective as N is in exciting N_2. The exponential is changed to the actual energy defect; the pre-exponential

is assumed to be the same as for N in exciting N_2 if the energy defect exceeds 3 ev, a value 10 times larger is used if the energy defect is less than 3 ev. Excitation by neutral molecules is not included because of the lack of direct experimental evidence. Excitation by electron impact, although very efficient, cannot readily be included because of the lack of information concerning the electron temperature. Excited states above the first of N_2 and CO are assumed to be in equilibrium with the first, denoted by N_2* and CO*, at the local translational temperature. Excitation transfer between N_2* and CO* is also included, assuming 1/4 the gas kinetic rate.

Originally the rate constants for the atom transfer reactions that produce CN* were estimated to be the same as for N in exciting N_2. However with these estimates, we found that the peak in CN* occurred much later than is seen experimentally. To obtain a good fit between theory and experiment, the reactions producing CN* were assumed to have rates approaching the gas kinetic value.

Dissociation of excited molecules is also an important process, particularly near peak radiation, and is included in the reaction rate system for N_2*, CO*, and CN*. The reactions and rate constants used are given as 69 through 93 in Table 3.

1. Equilibrium Constants. Not all of the reactions listed above are independent. A set of independent reactions which uniquely defines the equilibrium concentration of all species is formed. Equilibrium constants for this set are obtained by fitting the analytic expression $aT^b\exp(c/T)$ to the results of the Aeronutronic equilibrium species computer program (Section 2.3.1). These expressions reproduce the computer results within a few percent over the temperature range $4000^{\circ}K \leq T \leq 10,000^{\circ}K$. Equilibrium constants for the remaining reactions are computed from combinations of the basic set. The values used in the computer program are listed in Table 3.

3.2.2 COLLISION LIMITING

Some of the excited electronic states responsible for radiative heating in planetary entry may be de-excited by radiation more rapidly than they are excited by collision. This is known as "collision limiting". It requires that the radiative loss be included as a term in the reaction rate equation for the excited states affected by the radiation. Thus

$$\frac{dN^*}{dt} = \sum_{ij} Q_{p_{ij}} \gamma_i \gamma_j - \sum_k Q_{\ell_k} \gamma_k N^* - AN^* \qquad (32)$$

if the radiation is optically thin.

If the radiation is optically thick, the radiation loss term is reduced by absorption. However this leads to a difficult integration problem because the solution at any point depends on the final solution at all points. To avoid this difficulty the radiation loss for any optically thick transition often can be neglected. As will be seen this difficulty does not occur for the present calculations.

In order to determine which transitions are subject to collision limiting, the ratio $AN^*/\sum_{ij} Q_{p_{ij}} \gamma_i \gamma_j$ is computed for the specific conditions of interest. If it approaches or exceeds 1, collision limiting must be included. For the present case and equilibrium conditions at the stagnation point, this ratio is about 1 for CN violet, 0.01 for CN red, 0.05 for CO(4+), and 0.001 for CO (vib-rot). This ratio is about the same at conditions of peak non-equilibrium radiation. From this, we conclude that collision limiting is significant only for CN violet emission. Since the CN violet emission is essentially optically thin for the present cases, the radiation loss term can be included directly in the rate equation for CN*. This was done for the present calculations, using $A = 1.06 \times 10^7$ sec^{-1}.

3.2.3 INTEGRATION SCHEME

A Runge-Kutta numerical integration scheme, modified by Treanor,[51] is used to compute the non-equilibrium species concentrations. Most of the details of the numerical method are identical to those described by Treanor[51] and are not repeated here. However the method by which the step size is chosen is considerably different, offering an appreciable gain in computer time. The allowable step size at each point is taken as a definite fraction of the shortest of the relaxation distances of each species. Based on experience a value for this fraction of 0.5 or less provides sufficient accuracy. However the step size must be reduced when one or more species approaches equilibrium or quasi-equilibrium conditions. Under these conditions the rate equations become "stiff"[52] and the modified Runge-Kutta numerical integration scheme leads to divergent oscillations if the step size is too large. Tests are applied which require that the species production rate computed within the modified Runge-Kutta sequence must not exceed a value which would result in a relaxation distance shorter by a prescribed factor than the relaxation distance used in selecting the step size. If this test is failed, the step size is reduced by a factor of 2. If this is passed on 2 succeeding steps the step size is increased by a factor of 2 for the next step, and on up to the original value of 0.5 times the minimum relaxation distance.

The method permits integration of the non-equilibrium equations to within a few percent of equilibrium, requiring about 10 minutes on the Philco 2000 computer for the CO_2 system containing 13 species and 31 reactions, and 20 to 30 minutes for the N_2-CO_2-A system containing 24 species and 93 reactions.

3.2.4 COMPARISON WITH EXPERIMENT

The reaction rate system described in the preceding paragraphs has been evaluated by calculating non-equilibrium radiation profiles behind normal shocks in CO_2-N_2-A mixtures and comparing the results with experimental

measurements. In Section 3.4 a description is given of the methods used in computing non-equilibrium radiation profiles from the species profiles that are obtained from integrating the reaction rate equations.

Four comparisons are shown in Figures 9, 10, 11, and 12. It is seen that the agreement is generally good. The CN violet profile behind a 20,400 fps shock in a mixture of 25% CO_2, 75% N_2 at 0.175 torr shows particularly good agreement (Figure 9). Since these conditions are close to those of the present flight case, very little extrapolation error is introduced.

The CN red profile shown in Figure 10 is also in satisfactory agreement with the experimental data. The theoretical curve shows a somewhat sharper overshoot than the data shows: this is probably due in part to the finite slit width and the shock curvature present in the experiment. No other CN red comparisons are available.

The CN red and CN violet profiles of Figures 10 and 11 indicate that the $B^2\Sigma^+$ excited state of CN is not in thermal equilibrium with the ground state. The peak experimental ratio of I to I_{eq} is 4 for CN red and 5 for CN violet at $t \approx 0.4$ μsec. If the excited states are both in equilibrium with the ground state, the translational temperature must be within 6% of its equilibrium value to yield I/I_{eq} ratios this close to each other. However at the experimental peak, the translational temperature is predicted to be 28% higher than the equilibrium value. For comparison, the CN violet emission predicted on the basis of equilibrium with the ground state is shown in Figure 11. The non-equilibrium profile fits the data more closely.

The CN violet comparison shown in Figures 9, 11 and 12 are satisfactory in terms of computing the integrated non-equilibrium radiation. However the differences in profile shapes are sufficient to indicate that the

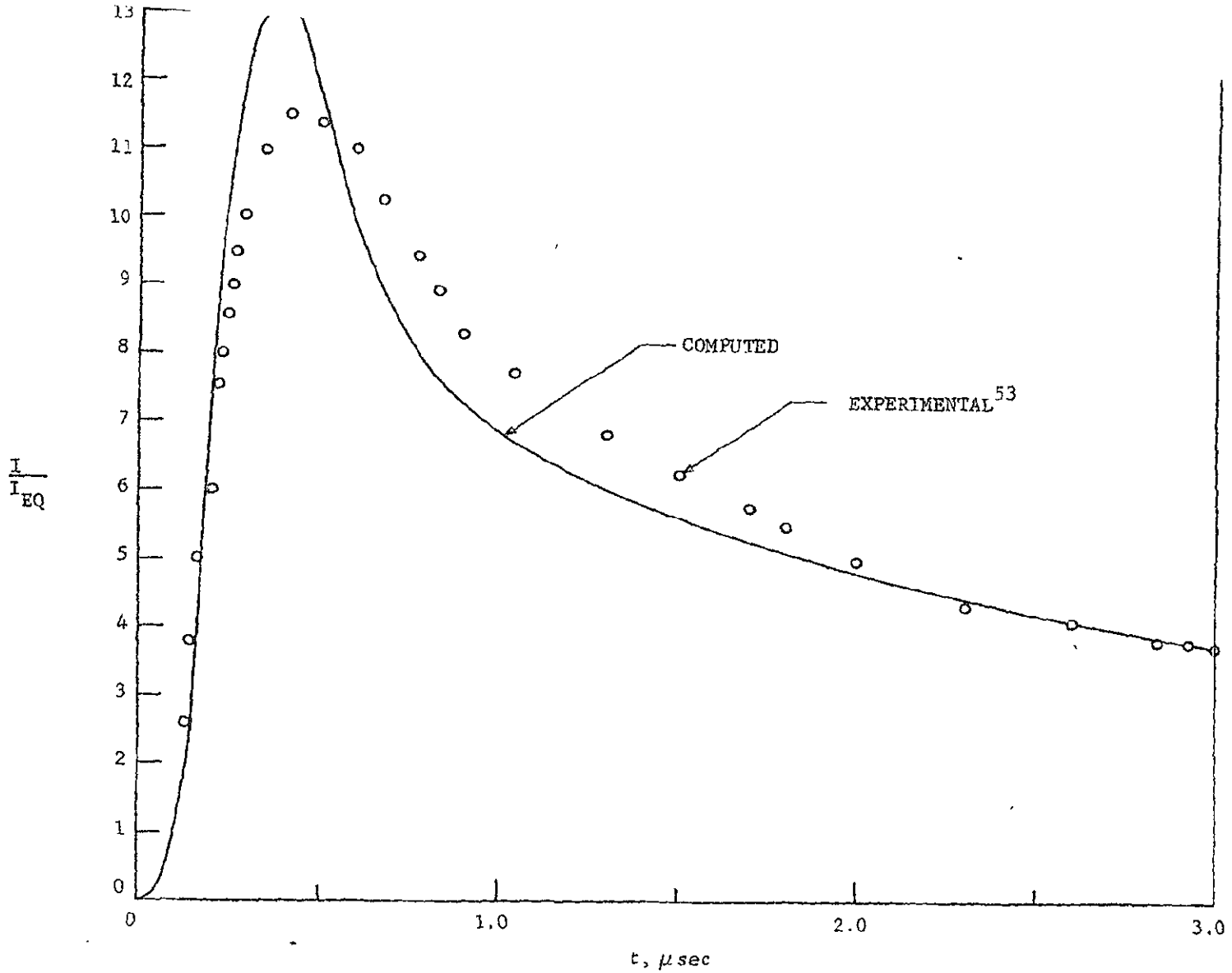

FIGURE 9. COMPARISON OF COMPUTED NON-EQUILIBRIUM CN VIOLET RADIATION PROFILE WITH THAT OBTAINED EXPERIMENTALLY BY ARNOLD[53] BEHIND A NORMAL SHOCK TRAVELING AT 20,400 FPS THROUGH A 25% CO_2, 75% N_2 MIXTURE AT AN INITIAL PRESSURE OF 175 μHG.

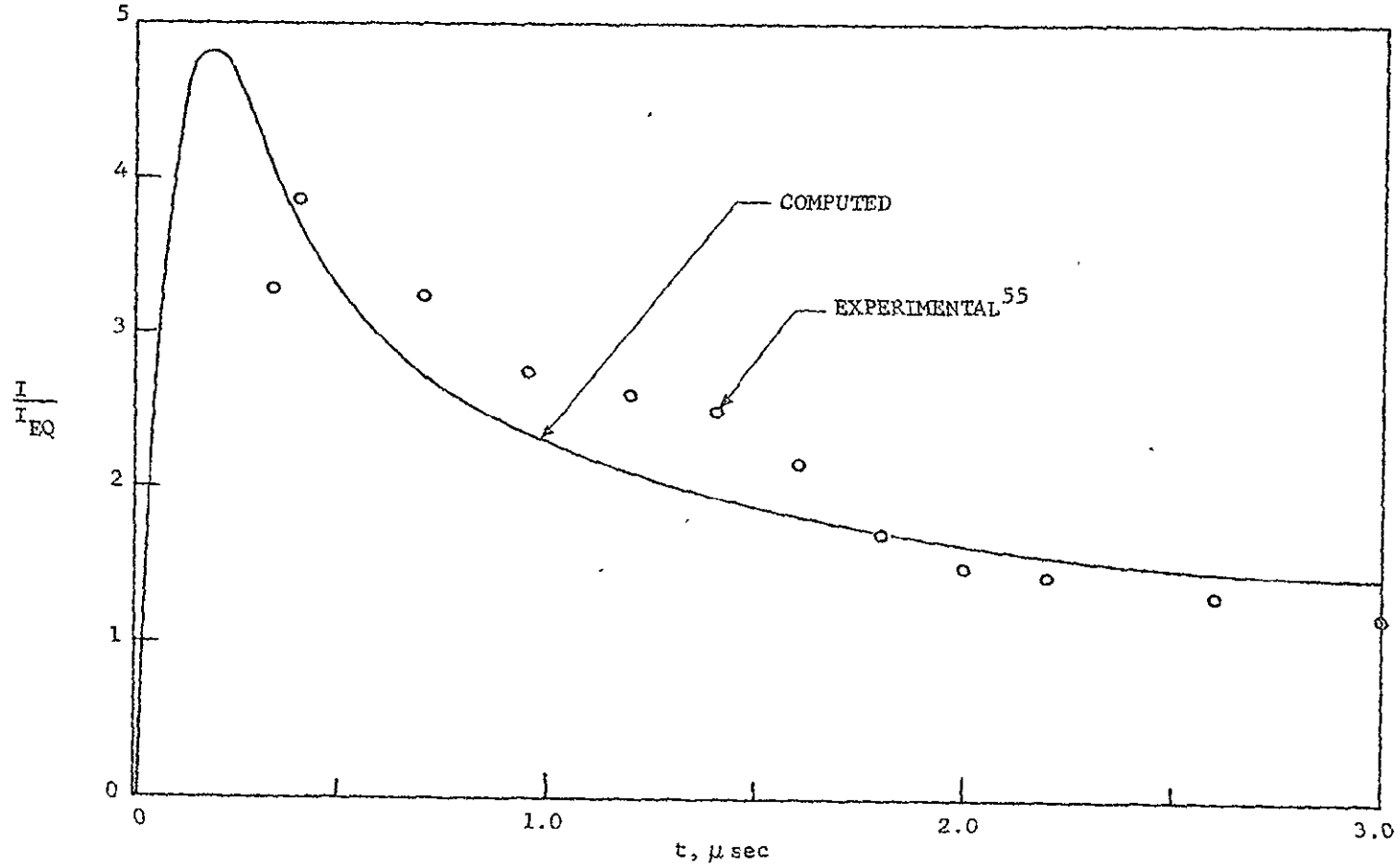

FIGURE 10. COMPARISON OF COMPUTED NON-EQUILIBRIUM CN RED RADIATION PROFILE WITH THAT OBTAINED EXPERIMENTALLY BY THOMAS AND MENARD[55] BEHIND A NORMAL SHOCK TRAVELING AT 24,600 FPS IN A 9% CO_2, 90% N_2, 1% A MIXTURE AT AN INITIAL PRESSURE OF 250 μ Hg.

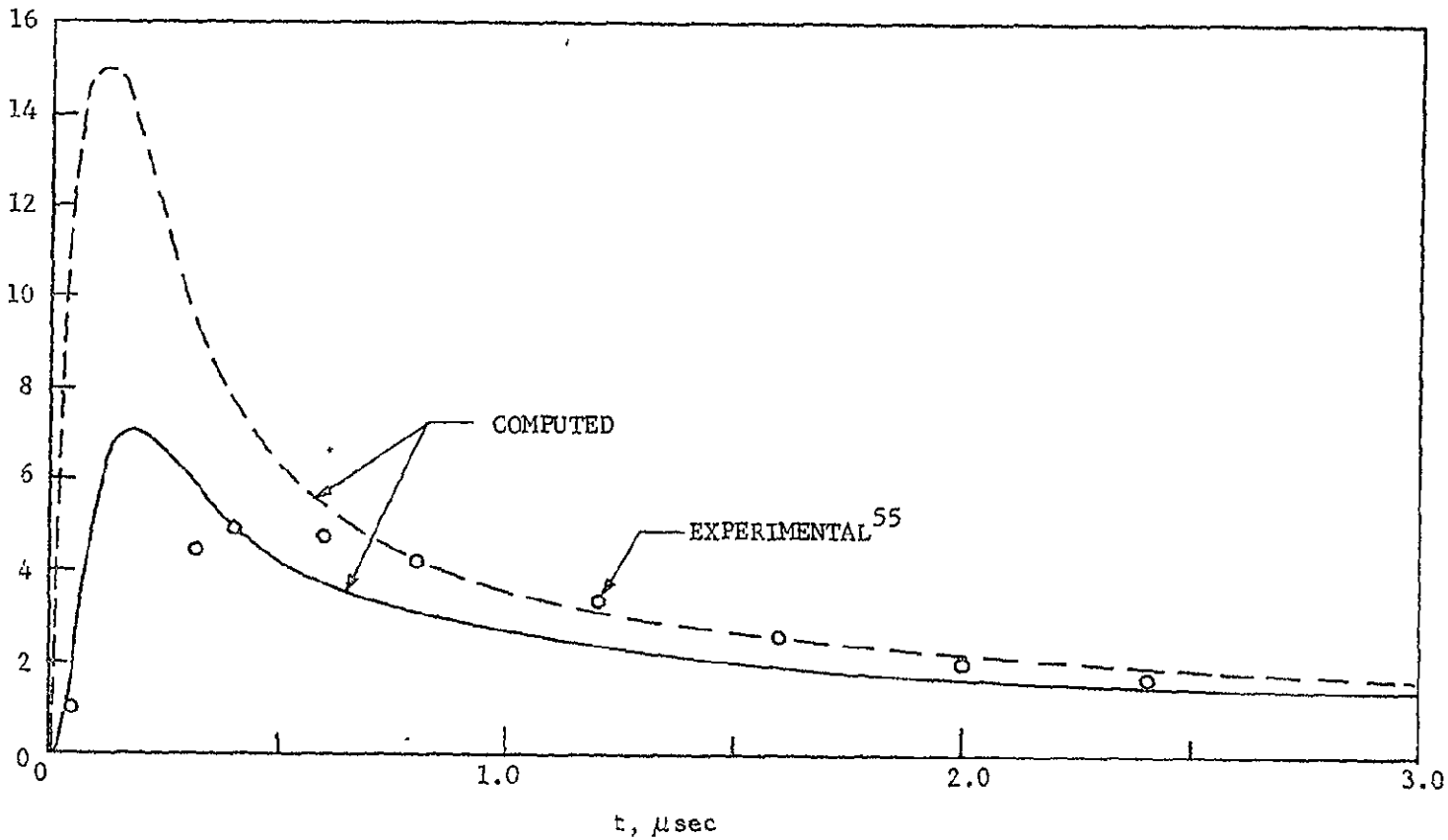

FIGURE 11. COMPARISON OF COMPUTED NON-EQUILIBRIUM CN VIOLET RADIATION PROFILE WITH THAT OBTAINED EXPERIMENTALLY[55] FOR THE CONDITIONS OF FIGURE 10. DASHED CURVE IS THE NON-EQUILIBRIUM CN VIOLET RADIATION PROFILE COMPUTED ASSUMING THE RADIATING STATE IS IN EQUILIBRIUM WITH THE GROUND STATE OF CN AT THE NON-EQUILIBRIUM TRANSLATIONAL TEMPERATURE

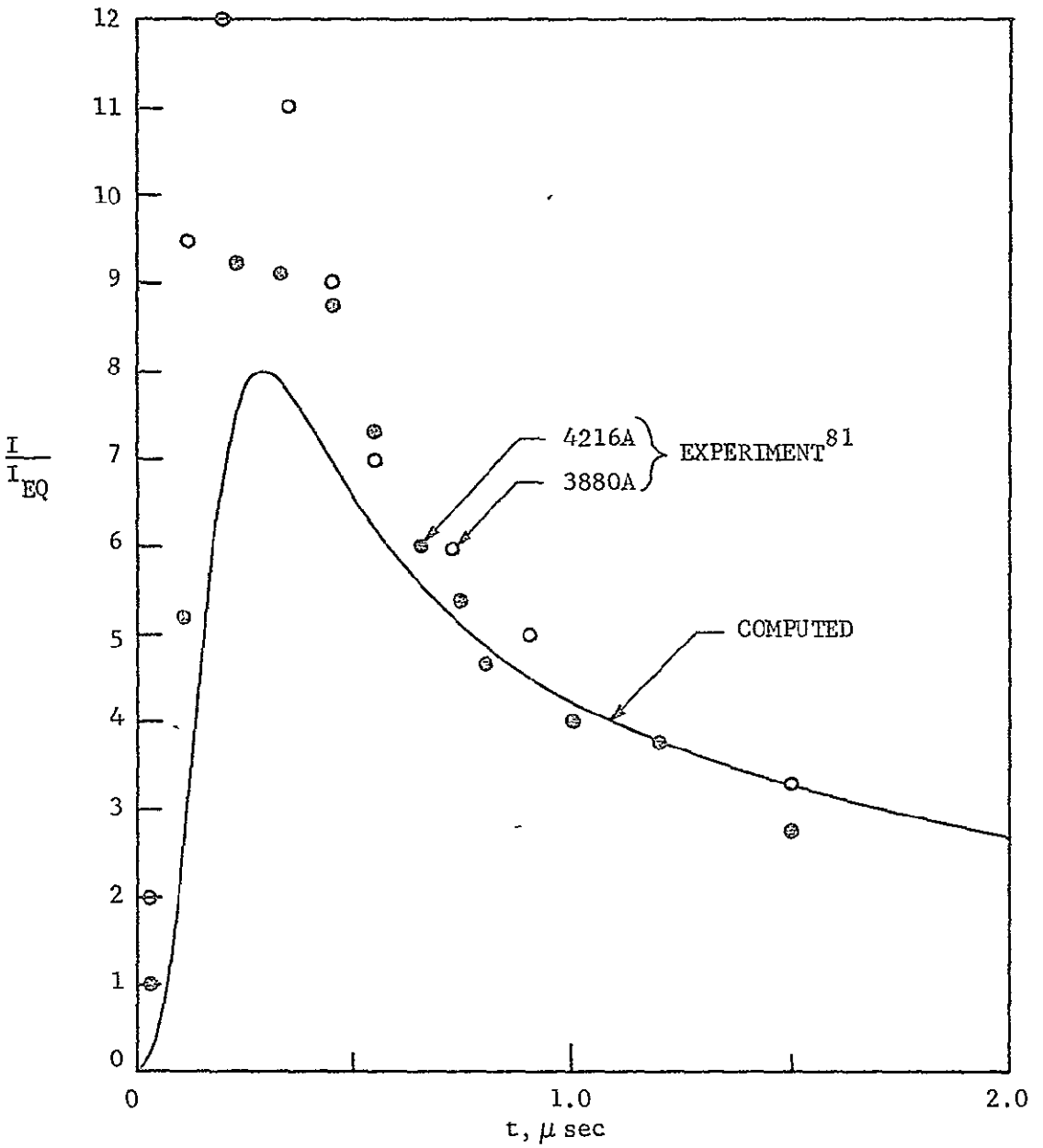

FIGURE 12. COMPARISON OF COMPUTED NON-EQUILIBRIUM CN VIOLET RADIATION PROFILE WITH THAT OBTAINED EXPERIMENTALLY BY ARNOLD[81] BEHIND A NORMAL SHOCK TRAVELING AT 20,600 FPS IN A 9.6% CO_2, 90.4% N_2 MIXTURE AT 350μ Hg.

reaction rate system used here is not fully satisfactory. Significant improvements can be made in the future only with a great deal more experimental and analytical study.

The approach and the reaction rate constants adopted here differ significantly from those used by McKenzie.[53] In his work the excited states of CN are assumed to be in equilibrium with the ground state. This makes it difficult to fit both CN red and CN violet data. His comparison with CN violet data is excellent, but no comparison with CN red is made. His prediction of the CN red peak is a factor of about 2.5 less than that using our reaction rate system. This question bears further study.

McKenzie's choice for the rate constant of one of the critical reactions, $CO + N \rightarrow CN + O$, is less than a factor of 2 smaller than ours, showing good agreement. However his choice for $N_2 + C \rightarrow CN + N$ is a factor of 7 smaller than ours at 9000°K. In addition his choice for the rate of dissociation of CN exceeds our estimate by a factor of 15 (at 9000°K) for O, C, N, NO, and CN as collision partner and by a factor of 90 (at 9000°K) for N_2, CO_2, CO, O_2, and C_2 as collision partner. McKenzie's choice appears quentionable until further support is obtained through direct experimental measurement.

In summary, although the present reaction rate system is not wholly satisfactory, it can be expected to provide adequate accuracy for flight calculations of non-equilibrium radiative heat transfer.

3.3 NON-EQUILIBRIUM CONVECTIVE HEAT TRANSFER ANALYSIS

The convective heat transfer analysis utilized for non-equilibrium flow calculations is the same as described in Section 2.2 for equilibrium flows. The assumption made is that the heat transfer for frozen, non-equilibrium and equilibrium chemistry boundary layers is identical even

for Lewis numbers slightly different than unity. This assumption is valid if (1) the edge of the boundary layer flow properties are at equilibrium, (2) the boundary layer gases are dissociated species that can be approximated as a binary mixture and (3) the wall is fully catalytic. The assumption of equilibrium edge properties is valid for the sphere cap, since the non-equilibrium property layer extends from the bow shock to a distance of only about 30% of the shock layer thickness; thus the properties at the boundary layer edge are very close to equilibrium. In the sphere-cone case the non-equilibrium region extends throughout the shock layer, but the boundary layer edge properties are not far from equilibrium conditions.

The dissociated gas in the boundary layer is accurately approximated by a binary mixture. Because of the binary nature of the boundary layer gas, the convective heat transfer is independent of the chemical kinetics.[54]

Radiation cooling of the inviscid gas is insignificant in the sphere-cone case, but must be included in the sphere-cap calculation. The radiation cooling effect is included in the stagnation-point convective heat transfer calculation by using the actual radiation-cooled boundary layer edge enthalpy rather than the adiabatic stagnation enthalpy. The convective heat transfer distribution over the whole body is thereby reduced by this correction factor. This is consistent with the result that radiation cooling reduces the boundary layer edge enthalpy by a factor that is nearly the same over the whole sphere-cap body.

3.4 NON-EQUILIBRIUM RADIATIVE HEAT TRANSFER ANALYSIS

3.4.1 NON-EQUILIBRIUM RADIATION

The non-equilibrium species and excited state populations obtained as outlined in Section 3.2 are combined with the equilibrium radiation program described in Section 2.3 to provide non-equilibrium volume

radiation emission. The chemical model used in computing the excited state populations has been described in Sections 3.2.1 and 3.2.2. The upper excited states of N_2 and CO are assumed to be in equilibrium with the lowest excited state, N_2*, and CO*, at the local non-equilibrium translational temperature. The $A^2\Pi$ state of CN is assumed to be in equilibrium with the ground state. The $B^2\Sigma^+$ state is computed directly as CN* in the integration of the reaction rate equations. The non-equilibrium excited state populations and the non-equilibrium temperature are used as inputs to the equilibrium radiation program to compute spectral absorption coefficients and non-equilibrium radiation emission. In this model the populations of the vibrational and rotational states of the excited band radiators are assumed to be in local thermodynamic equilibrium with the non-equilibrium translational temperature. This assumption is justified on the basis of shock tube measurements which show that the vibrational and rotational degrees of freedom are equilibrated immediately behind normal shock waves for shock speeds above 13,000 to 15,000 ft/sec. Free-bound emission and absorption is computed on the basis of non-equilibrium species compositions and excited state populations in equilibrium with the nearest continuum of states at the local translational temperature. The infrared vibration-rotation band emission of CO and NO and CN is assumed to be at the local non-equilibrium translational temperature; this emission is only weakly dependent on temperature.

Comparisons between calculations using the Aeronutronic non-equilibrium radiation program and the shock tube measurements of Thomas and Menard[55] and Arnold[53] are shown in Figures 9, 10, 11, and 12 and are described in Section 3.2.4. These intensity-time profiles indicate that the overall behavior of non-equilibrium radiation from CN is satisfactorily reproduced by the computer program. No comparison such as this can be made for the CO(4+) band, because there is no published data. For this reason, the

CO(4+) band was assumed to reach its equilibrium value rapidly, but to exhibit no overshoot. This assumption may be in error by one to two orders of magnitude.

When the non-equilibrium integration along streamlines approaches equilibrium it is economical to shift from non-equilibrium radiation to equilibrium radiation. This is done at a point on the streamline for which the non-equilibrium radiation reaches within 10% of the local equilibrium value. When this shift is made on each streamline it is retained throughout the remainder of the flow field. Subsequent expansion of the streamline is treated as equilibrium, an approximation that is well justified in the present calculations on the basis of the non-equilibrium analysis.

3.4.2 SELF-ABSORPTION OF NON-EQUILIBRIUM RADIATION

The method used to account for self-absorption of non-equilibrium radiation is the same as that used for equilibrium radiation (see Section 2.3.3). This method involves the integration of the radiation emission out to a distance of one absorption length from the surface point. This is done in each direction along which the integration is made. The non-equilibrium absorption coefficient is the same as the equilibrium value at the same temperature and pressure, since the absorption arises from the ground electronic state of each molecule, and we have assumed equilibration of the rotational and vibrational states with the translational temperature. Fortunately the self-absorption corrections are small, affecting the CO fourth positive band strongly and the CN violet band slightly. The CO band contributes less than 10% of the radiation in the present non-equilibrium cases.

3.4.3 RADIATION-INVISCID FLOW COUPLING

The cooling of the inviscid flow due to radiation losses is included in these calculations by the following approximate method. Throughout most of the non-equilibrium region the effect reduces the enthalpy very little

and affects the total emission from the non-equilibrium layer by no more than 10%. Because of the difficulty of including this effect in the integration of the rate equations, it has been neglected here. However beyond the point on each streamline at which the radiation is assumed to be the equilibrium value the effects of radiation cooling are included. This is done by utilizing the values of pressure, velocity, and density obtained from the flow field calculation (which neglected radiation cooling) and computing a first order correction to the enthalpy and the volume emission. This correction is found by integrating the (corrected) radiation loss along streamlines. In this integration self-absorption is included, although only minor effects arise in the present cases. Corrections to the volume emission are as large as 30% in the sphere-cap case. Numerical results are given in Section 4.2.

3.4.4 RADIATION-VISCOUS LAYER COUPLING

This is included in the same manner as described for equilibrium radiation in Section 2.3.5. A portion of the CO(4+) band is self-absorbed within the thermal boundary layer thickness for the sphere-cap case and is therefore omitted in the radiation integration. Radiation absorption in the boundary layer has negligible effect on the convective heat transfer.

3.4.5 GEOMETRIC INTEGRATION

This is carried out in much the same manner as in the equilibrium case described in Section 2.3 6. However the integration over the non-equilibrium layer for the sphere-cap case was simplified by determining the total emission from the non-equilibrium slab at each radial position. This was then used at each intersection of the viewing rays with the non-equilibrium slab when carrying out the geometric integration.

SECTION 4

NUMERICAL RESULTS

The flow field and the convective and radiative heat transfer have been computed for equilibrium flow over a sphere-cone and for non-equilibrium flow over a sphere-cone and sphere-cap for the following flight condition

Mach Number	31
Flight Velocity	19,600 ft/sec
Ambient Density	10^{-6} slugs/ft^3
Ambient Temperature	180^{o}R
Ambient Composition	70% N_2, 30% CO_2
Angle of Attack	0^{o}
Base Diameter	12 ft

Results of the equilibrium calculations are presented in Section 4.1; results of the non-equilibrium calculations are presented in Section 4 2.

4.1 EQUILIBRIUM FLOW OVER A SPHERE-CONE

4.1.1 EQUILIBRIUM SPHERE-CONE INVISCID FLOW PROPERTIES

It was originally anticipated that the inviscid flow field calculations would be made with a first approximation integral relation computer program. In order to verify the accuracy of the integral method, the

theoretical shock shape for a 60° half-angle cone in a Mach 9, $\gamma = 1.4$, air flow was computed and compared with experiment. The results are shown in Figure 5. It is seen that the first approximation solution provides an accurate calculation of the shock shape. It was determined, however, midway through the present program that real gas effects ($\gamma-1 \ll 1$) significantly influence the character of the 60° cone flow field, and that a higher order solution of the inviscid conservation equations is required to obtain an accurate shock shape and shock layer properties. It was decided that the Philco-Ford time dependent finite difference program should be used to make the inviscid flow field calculations.

The sphere-cone shock shape obtained from both the time dependent finite difference equilibrium solution and a low γ ($\gamma = 1.18$) first approximation integral relation solution are shown in Figure 13. Although the integral solution is accurate in the sphere cap region, the shock layer thickness in the conical flow region is overestimated by as much as a factor of 2 in some places. The first approximation integral relation solution is accurate for blunt body flow field calculations in which the shock layer flow is predominantly subsonic. When a large portion of the shock layer is supersonic as it is in the case of the equilibrium blunt 60° cone problem, however, the first approximation exaggerates the influence of the body properties on the shock layer calculation and overestimates the shock detachment distance.

The time dependent solution indicates that the equilibrium shock layer in the conical region is predominantly supersonic and that the compression waves at the sphere cone junction travel without significant dispersion outward to the bow shock. The interaction produces a concave region in the bow shock where it regains strength. This concavity is observed in the shock shape plot presented in Figure 13. The subsequent reflections of the compression wave are negligible, but theoretically there is an entire series of alternating compression

TABLE 5

EQUILIBRIUM INVISCID SHOCK LAYER PROPERTIES ON SPHERE-CONE

Body Station	Arc Length on Surface, Ft	Standoff Distance, Ft	x, Ft	y, Ft	Pressure, Psia	Enthalpy Kcal/100 GM	Speed, 10^4 ft/sec	Radiation, watts/cm^3 ster
1.Shock	.0785	.0677	-.0622	.0825	2.33	338	.211	.920
Midpoint			-.0282	.0804	2.44	341	.111	.990
Body			+.00513	.0783	2.53	342	.0497	1.038
2	.235	.0694	-.0422	.247	2.35	332	.313	.878
			-.00786	.240	2.40	335	.255	.930
			.0256	.234	2.45	339	.183	.980
3	.392	.0733	-.00297	.408	2.07	301	.612	.538
			.0320	.396	2.17	321	.442	.723
			.0661	.385	2.20	334	.287	.828
4	.549	.0733	.0605	.562	1.91	269	.817	.306
			.0937	.546	1.92	299	.628	.480
			.126	.530	1.95	326	.388	.673
5	.706	.0767	.134	.706	1.85	251	.911	.246
			.167	.687	1.84	282	.738	.362
			.200	.668	1.83	315	.496	.555
6	.863	.0821	.207	.845	1.87	247	.931	.204
			.243	.824	1.90	273	.793	.332
			.279	.804	1.93	309	.550	.546
7	1.021	.0889	.280	.985	1.91	248	.922	.216
			.319	.962	1.94	267	.825	.304
			.357	.940	1.97	302	.607	.508
8	1.346	.1083	.426	1.277	1.95	255	.889	.254
			.473	1.249	1.98	261	.857	.287
			.520	1.222	1.99	284	.726	.410

Table 5 (continued)

Body Station	Arc Length on Surface, Ft	Standoff Distance, Ft	x, Ft	y, Ft	Pressure, Psia	Enthalpy Kcal/100 GM	Speed, 10^4 ft/sec	Radiation, watts/cm^3 ster
9	1.841	.1412	.644	1.722	1.96	258	.876	.262
			.706	1.686	1.99	260	.863	.284
			.767	1.651	2.00	275	.779	.362
10	2.336	.1805	.860	2.168	1.97	260	.862	.282
			.938	2.123	2.00	264	.862	.308
			1.015	2.079	2.00	270	.808	.340
11	2.830	.2127	1.076	2.615	1.97	259	.868	.277
			1.170	2.561	1.99	260	.864	.285
			1.262	2.507	2.00	267	.825	.323
12	3.325	.2536	1.293	3.061	1.97	260	.861	.282
			1.402	2.998	1.99	260	.863	.285
			1.509	2.939	2.00	265	.836	.313
13	3.820	.2895	1.508	3.508	1.97	260	.863	.282
			1.634	3.435	1.99	260	.864	.285
			1.757	3.364	2.00	264	.844	.308
14	4.314	.3251	1.726	3.953	1.96	250	.871	.275
			1.866	3.872	1.99	259	.866	.280
			2.004	3.793	2.00	262	.850	.298
15	4.809	.3671	1.942	4.400	1.97	261	.858	.288
			2.098	4.310	1.99	260	.865	.285
			2.251	4.221	2.00	261	.856	.292
16	5.304	.3979	2.159	4.845	1.96	257	.876	.267
			2.331	4.746	1.99	259	.869	.280
			2.499	4.649	2.00	260	.860	2.87
17	5.798	.441	2.379	5.289	1.97	259	.866	.277
			2.567	5.181	1.99	259	.868	.280
			2.746	5.078	2.00	260	.864	.287

Table 5 (continued)

Body Station	Arc Length on Surface, Ft	Standoff Distance, Ft	x, Ft	y, Ft	Pressure, Psia	Enthalpy Kcal/100 GM	Speed, 10^4 ft/sec	Radiation, watts/cm^3 ster
18	6.124	.468	2.522	5.584	1.98	261	.860	.289
			2.721	5.468	2.00	259	.868	.282
			2.909	5.360	2.00	250	.866	.282
19	6.281	.478	2.590	5.726	1.97	261	.860	.288
			2.798	5.606	1.99	259	.868	.280
			2.988	5.496	2.00	259	.867	.282
20	6.438	.487	2.657	5.868	1.97	261	.857	.288
			2.881	5.739	1.99	259	.870	.280
			3.066	5.632	2.00	259	.869	.282
21	6.595	.520	2.759	6.069	1.93	257	.879	.258
			2.982	5.895	1.88	256	.883	.244
			3.153	5.762	1.70	253	.899	.200
22	6.752	.608	2.909	6.348	1.87	250	.913	.215
			3.113	6.073	1.62	250	.911	.177
			3.263	5.872	1.16	245	.940	.102
23	6.909	.784	3.117	6.663	1.66	233	.995	.123
			3.282	6.241	1.29	244	.944	.115
			3.397	5.950	..713	238	.971	.047
24	7.065	1.072	3.434	7.052	1.42	199	1.137	.0364
			3.502	6.400	.970	237	.975	.0680
			3.547	5.990	.435	239	.967	.0262
25	7.222	1.617	3.945	7.532	1.17	186	1.190	.0171
			3.787	6.545	.690	230	1.007	.0366
			3.703	5.990	.264	238	.973	.0135
26	7.378	2.581	4.788	8.054	.821	193	1.162	.0151
			4.157	6.646	.449	221	1.047	.0171
			3.853	5.950	.157	234	.991	.0064

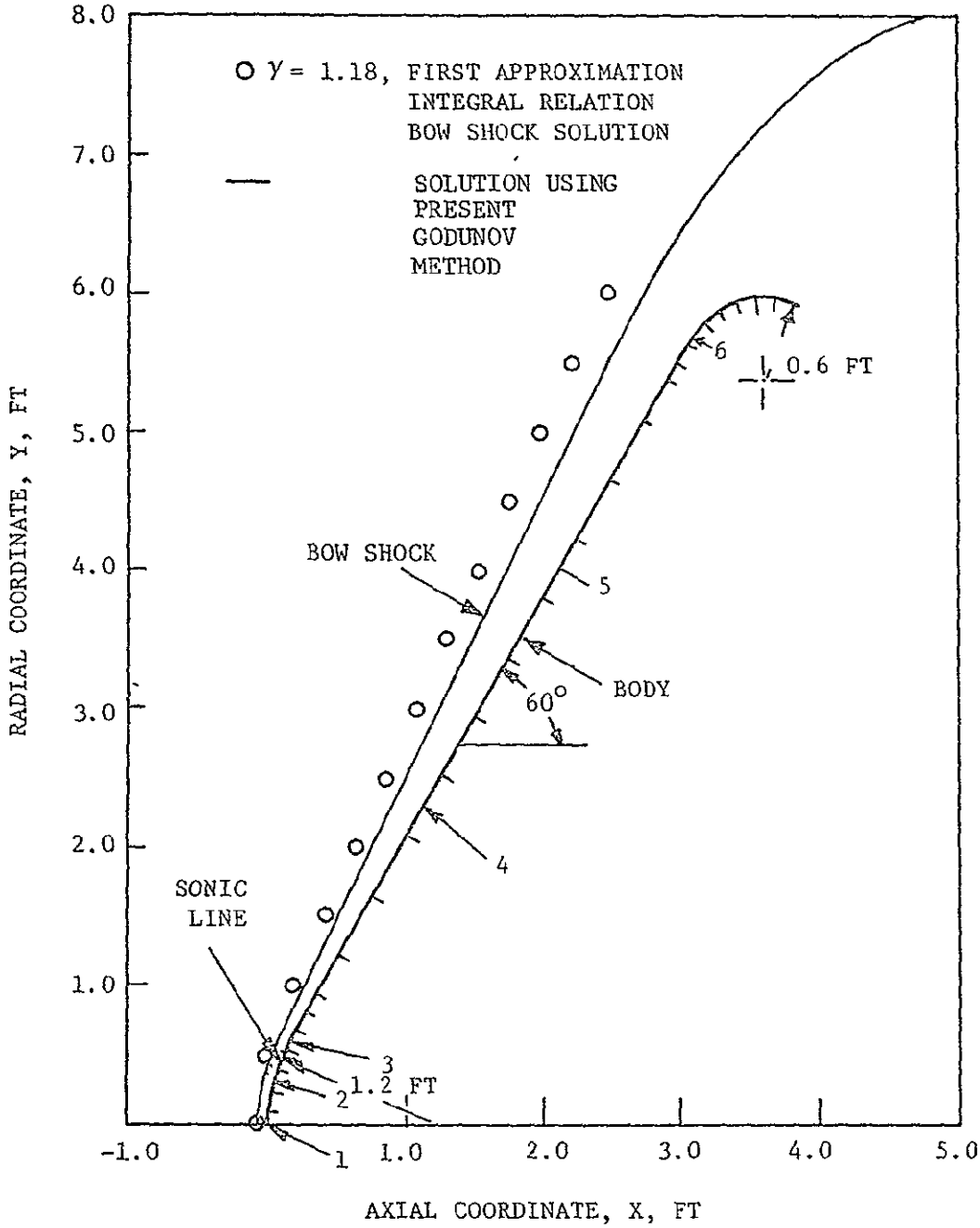

FIGURE 13. BLUNT SPHERE-CONE BODY AND EQUILIBRIUM SHOCK SHAPE

and expansion waves along the layer. In the higher γ cases, the subsonic shock layer disperses the compression and there is no concavity to the shock. At higher γ's, the concavity has been observed on sharper cones.[56]

The flow over the 60^{o} sphere-cone in air (γ = 1.4) shown in Figure 5 contains a subsonic shock layer with a sonic line running approximately normal to the cone surface and starting at the outer corner of the cone. In contrast, the equilibrium flow of a 30% CO_2, 70% N_2 mixture over a similar body shape displays a shock layer that is almost entirely supersonic. The velocity on the entire conical surface is subsonic, but, as seen in Figure 15, it rapidly becomes supersonic away from the surface. The sonic line runs from the rounded shoulder of the base roughly parallel to the cone surface at about 10% of the standoff distance, finally crossing the shock layer below the sphere-cone junction to reach the bow shock.

In Figure 14, the cone surface pressure as a function of the ratio of body surface distance to base radius is shown. The two prominent features of the pressure distribution a re the rapid decrease in pressure on the spherical portion of the sphere-cone and the pressure recovery at the sphere-cone junction to a pressure plateau in the conical region. The pressure distribution in the nose region is similar to a hemispherical shock layer result and the pressure plateau in the conical region is similar to a pointed cone supersonic flow result. In Figure 14 it is seen that the Newtonian flow model, which is a low γ limit of the hypersonic inviscid flow field equations, provides a useful approximation to the detailed flow field pressure distribution result.

In Table 5, the properties of the shock layer gas on 26 normals to the body surface are tabulated. For reference, the location of the body normals, in which the shock layer properties are specified, are shown on the body in Figure 13. The arc length, s, along the body to the intersection with each normal and the shock standoff distance on each normal

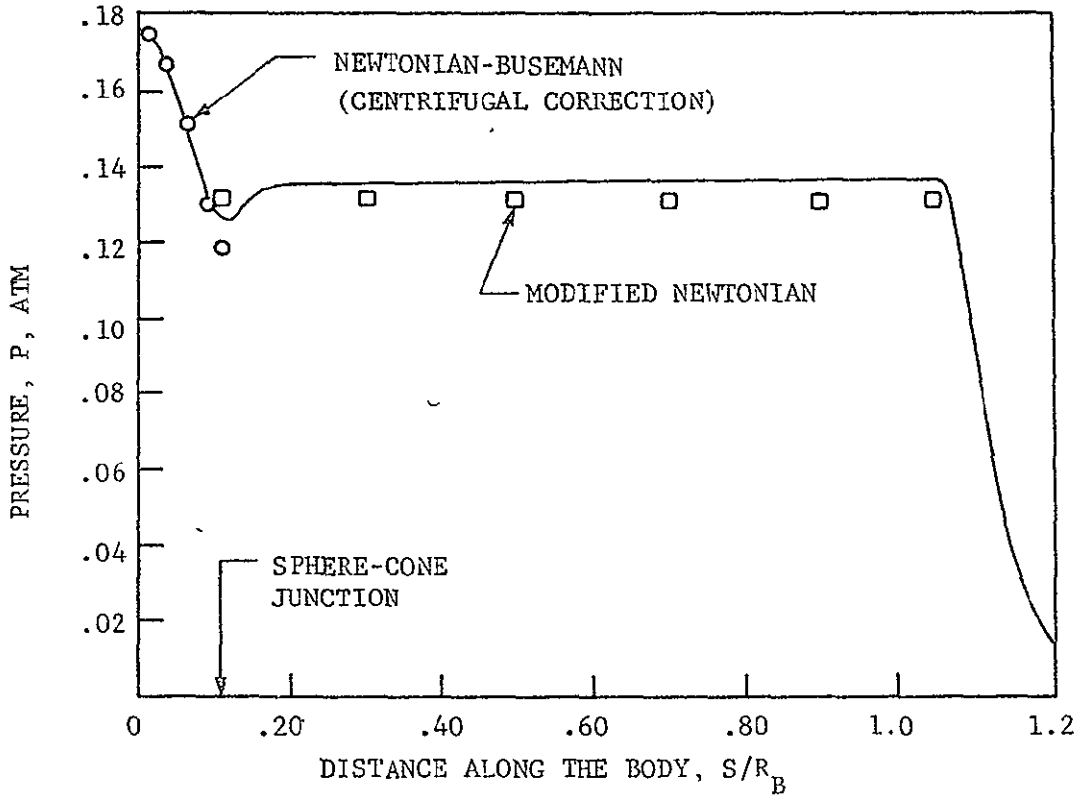

FIGURE 14. EQUILIBRIUM SURFACE PRESSURE ON THE SPHERE-CONE

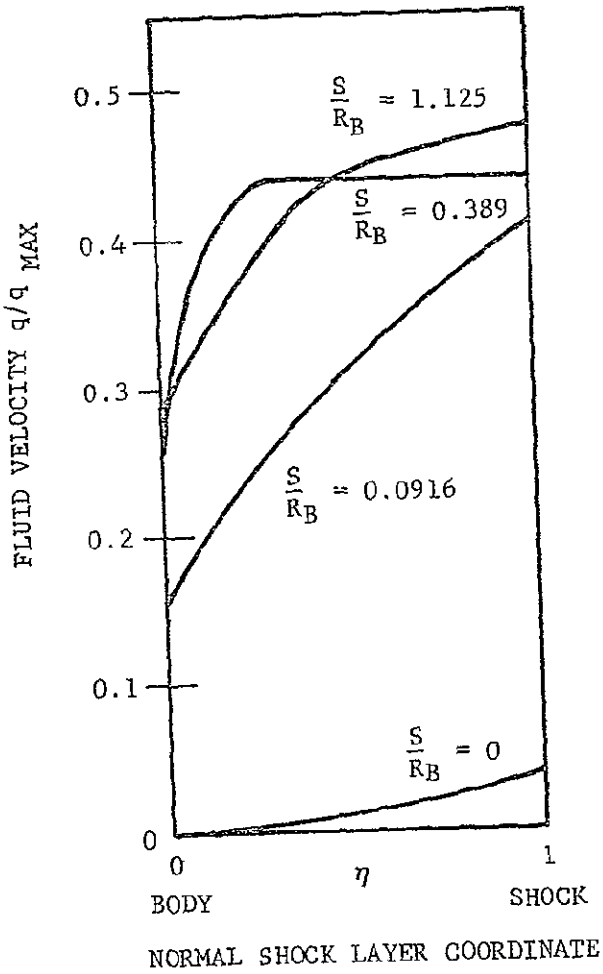

FIGURE 15. FLUID VELOCITY PROFILES ON BODY NORMALS OF THE SPHERE-CONE

are given in the second and third columns. The axial and radial coordinates of the intersections of each normal with the shock, with the half-way point, and with the body surface are specified in the vertical grouping in the next two columns. The origin of the coordinate system is at the nose of the sphere. The pressure, enthalpy, temperature, fluid velocity and radiation flux at the three points on each normal are listed in the subsequent columns.

In this tabulation, the presence of an actual inviscid entropy layer on the conical portion has been neglected. This layer contains the fluid that entered the shock layer in the blunt nose region An estimate of the width of the layer can be obtained from the fine mesh computation discussed earlier for $\gamma = 1.1$, $M = 20$. A typical velocity profile along a normal to the conical portion is presented in Figure 15. The normal is located near the onset of the region of constant pressure on the body surface, where the entropy layer has its largest extent. It is seen that the layer comprises at most 25% of the entire shock layer. Since the viscous boundary layer can be expected to comprise 15% of the shock layer width, there should be only a minor entropy layer. The coarse mesh, which averages quantities along each one-third of the normal, adequately portrays the flow encountered by the outer edge of the boundary layer.

4.1.2 EQUILIBRIUM SPHERE-CONE CONVECTIVE HEAT TRANSFER

The equilibrium sphere-cone laminar convective heat flux versus distance along the body is shown in Figure 16. For comparison purposes the heat flux obtained from modified Newtonian pressure distribution and normal shock entropy is also plotted. In the spherical region of the body, the equilibrium laminar convective heat transfer exceeds the modified Newtonian result because of the vorticity interaction effects. In the region aft of the sphere-cone junction, the detailed flow field solution predicts higher heat transfer because the boundary layer edge velocity

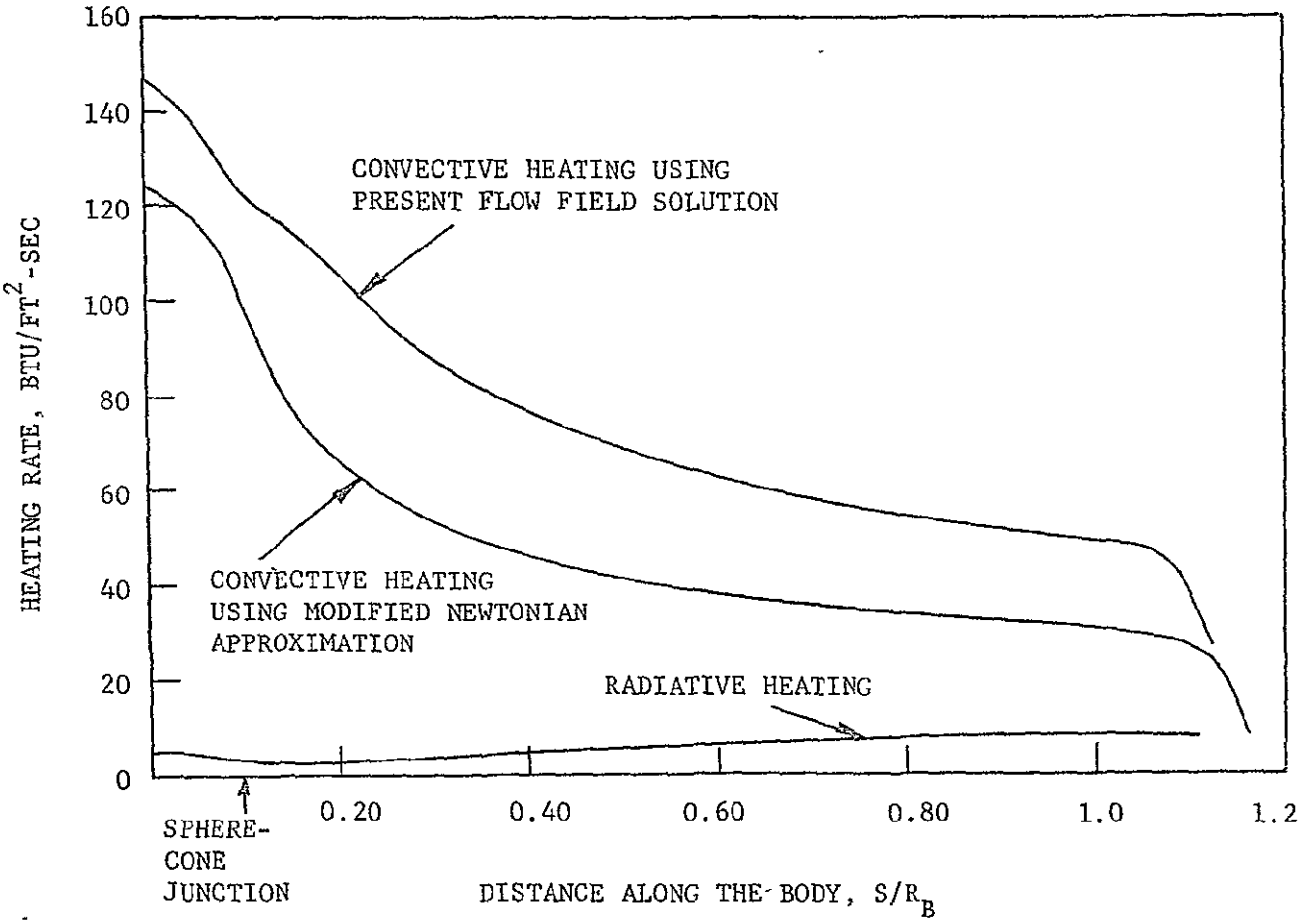

FIGURE 16. SPHERE-CONE EQUILIBRIUM CHEMISTRY CONVECTIVE AND RADIATIVE HEAT TRANSFER DISTRIBUTIONS

conditions in this region are characterized by the conical shock entropy rather than the normal shock entropy. As a result the boundary layer edge velocities and hence the heat transfer are higher than those given by the Newtonian normal shock entropy calculation. On the sphere, the combined effects of vorticity interaction (12%) and ambient composition (8%) increase the stagnation point heat transfer approximately 20% over an equivalent high Reynolds number air calculation.

4.1.3 EQUILIBRIUM SPHERE-CONE RADIATIVE HEAT TRANSFER

The optically thin spectrally integrated radiative emission from volume elements of the shock layer gas is included in Table 5. The spectral distribution is given in Table 6 for the gas adjacent to the stagnation point and in Table 7 for the gas adjacent to point 5 on the sphere-cone (see Figure 13). The species concentrations for each of these points are also given in the respective tables. The major radiation arises from the CN violet and red bands and from the 4th positive band of CO. Minor contributions arise from the E-X and H-X bands of CN and the vibration-rotation bands of CO.

Because self-absorption of the CN violet band may be greater than inferred from the course frequency interval used in obtaining the results of Table 6, a much finer frequency interval was also used. These results are given in Table 8, and show a higher maximum absorption coefficient by a factor of 2.5. However even with this value, there is negligible self-absorption of the CN violet band in the equilibrium sphere-cone flow field.

The radiative heat transfer to the seven body points shown in Figure 13 is given in Table 9. In the final column the predicted radiation

TABLE 6

EQUILIBRIUM RADIATION FROM FLOW ADJACENT TO SPHERE-CONE STAGNATION POINT
($T = 5735^{\circ}K$, $P = 0.172$ atm)

Mole-Fraction for CN VLT = 0.37560-002
Mole-Fraction for CN RED = 0.37560-002
Mole-Fraction for CN E-X = 0.37560-002
Mole-Fraction for CN H-X = 0.37560-002
Mole-Fraction for CO(4+) = 0.18280+000

Wave Number	Band System Opacity, CM^{-1}				
CM^{-1}	CN VLT	CN RED	CN E-X	CN H-X	CO(4+)
0.20000+004	0.	0.14312-004	0.49105-025	0.81808-028	0.72822-033
0.40000+004	0.	0.93002-004	0.74936-024	0.15086-026	0.22247-031
0.60000+004	0 46148-014	0.28116-003	0.91666-023	0.22371-025	0.55076-030
0.80000+004	0.30425-012	0.40538-003	0.10280-021	0.30441-024	0.12539-028
0.10000+005	0.65861-011	0.55264-003	0.11050-020	0.39716-023	0.27394-027
0.12000+005	0.57831-010	0 30772-003	0.11610-019	0.50658-022	0.58535-026
0.14000+005	0.90560-010	0.16743-003	0.12042-018	0.63792-021	0.12351-024
0.16000+005	0 26066-008	0.65912-004	0.12396-017	0.79735-020	0.25872-023
0.18000+005	0.19210-006	0.20172-004	0.12704-016	0.99223-019	0.53958-022
0.20000+005	0.43475-005	0.54522-005	0.12986-015	0.12315-017	0.11224-020
0.22000+005	0.63090-004	0.13089-005	0.13254-014	0.15261-016	0.23313-019
0.24000+005	0.63983-003	0.27540-006	0.13616-013	0.18893-015	0.48375-018
0.26000+005	0.62833-002	0.46057-007	0.13876-012	0.23376-014	0.10032-016
0.28000+005	0.13411-002	0.66029-008	0.14142-011	0.28913-013	0.20798-015
0.30000+005	0.35291-004	0.78125-009	0.14422-010	0.35754-012	0.43109-014
0.32000+005	0.31430-005	0.72126-010	0.14714-009	0.44208-011	0.89343-013
0.34000+005	0.56086-007	0.48608-011	0.14984-008	0.54657-010	0.18515-011
0.36000+005	0.93277-008	0.21443-012	0.15266-007	0.67576-009	0.38366-010
0.38000+005	0.11921-009	0.	0.15585-006	0.83854-008	0.79500-009
0.40000+005	0.38280-010	0.	0.15861-005	0.10369-006	0.16475-007
0.42000+005	0.20920-011	0.	0.13578-004	0.12685-005	0.34179-006
0.44000+005	0.30676-013	0.	0.62911-004	0.10738-004	0.70090-005
0.46000+005	0.16939-014	0.	0.14935-003	0.40411-004	0.12631-003
0.48000+005	0.24141-015	0.	0.30665-003	0.86559-004	0.13621-002
0.50000+005	0.11412-016	0.	0.59595-003	0.17406-003	0.52959-002
0.52000+005	0.67236-018	0.	0.11861-002	0.36963-003	0.12400-001
0.54000+005	0.43838-021	0.	0.20201-002	0.94194-003	0.24544-001

Table 6 (continued)

Wave Number CM^{-1}	Band System Opacity, CM^{-1}				
	CN VLT	CN RED	CN E-X	CN H-X	CO(4+)
0.56000+005	0.13550-026	0.	0.29352-002	0.80197-003	0.46001-001
0.58000+005	0.41882-032	0.	0.41230-002	0.11818-002	0.94080-001
0.60000+005	0.12946-037	0.	0.48172-002	0.15242-002	0.16549+000
0.62000+005	0.40015-043	0.	0.54684-002	0.19009-002	0.24254+000
0.64000+005	0.12369-048	0.	0.38690-002	0.22547-002	0.34075+000
0.66000+005	0.38231-054	0.	0.23734-002	0.20347-002	0.38584+000

Wave Number, cm^{-1}	Total Absorption Coefficient, cm^{-1}	B(W,T), $watts/cm^2$-ster	Emission, $watts/cm^3$-ster
0.20000+004	0.23336-003	0.14620-001	0.34119-005
0.40000+004	0.99729-004	0.44110-001	0.43990-005
0.60000+004	0.28117-003	0.73381-001	0.20632-004
0.80000+004	0.40538-003	0.94660-001	0.38374-004
0.10000+005	0.55264-003	0.10548+000	0.58292-004
0.12000+005	0.30772-003	0.10663+000	0.32812-004
0.14000+005	0.16743-003	0.10047+000	0.16821-004
0.16000+005	0.65915-004	0.89711-001	0.59133-005
0.18000+005	0.20364-004	0.76780-001	0.15636-005
0.20000+005	0.97998-005	0.63492-001	0.62221-006
0.22000+005	0.64399-004	0.51032-001	0.32864-005
0.24000+005	0.64011-003	0.40051-001	0.25637-004
0.26000+005	0.62834-002	0.30801-001	0.19353-003
0.28000+005	0.13411-002	0.32379-001	0.31220-004
0.30000+005	0.35292-004	0.17329-001	0.61159-006
0.32000+005	0.31432-005	0.12731-001	0.40016-007
0.34000+005	0.57626-007	0.92445-002	0.53272-009
0.36000+005	0.25291-007	0.66436-002	0.16803-009
0.38000+005	0.16514-006	0.47306-002	0.78119-009
0.40000+005	0.17063-005	0.33406-002	0.56999-008

Table 6 (continued)

Wave Number, cm^{-1}	Total Absorption Coefficient, cm^{-1}	B(W,T), $watts/cm^2$-ster	Emission, $watts/cm^3$-ster
0.42000+005	0.15188-004	0.23414-002	0.35561-007
0.44000+005	0.80658-004	0.16299-002	0.13147-006
0.46000+005	0.31607-003	0.11276-002	0.35641-006
0.48000+005	0.17553-002	0.77571-003	0.13616-005
0.50000+005	0.60659-002	0.53085-003	0.32201-005
0.52000+005	0.13956-001	0.36154-003	0.50456-005
0.54000+005	0.27506-001	0.24514-003	0.67428-005
0.56000+005	0.49738-001	0.16553-003	0.82333-005
0.58000+005	0.99385-001	0.11135-003	0.11067-004
0.60000+005	0.17183+000	0.74637-004	0.12825-004
0.62000+005	0.24991+000	0.49861-004	0.12461-004
0.64000+005	0.34687+000	0.33206-004	0.11518-004
0.66000+005	0.39024+000	0.22049-004	0.86046-005

Total Emission = 0.10376+001 $watts/cm^3$-ster

TABLE 7

EQUILIBRIUM RADIATION FROM FLOW ADJACENT TO BODY POINT 5 ON SPHERE-CONE
($T=5342^{O}K$, $P = 0.136$ atm)

Mole-Fraction for CN VLT = 0.16110-002 Mole-Fraction for CN RED = 0.16110-002
Mole-Fraction for CN E-X = 0.16110-002 Mole-Fraction for CN H-X = 0.16110-002
Mole-Fraction for CO(4+) = 0.20980+000

Wave Number, CM^{-1}	Band System Opacities, CM^{-1}				
	CN VLT	CN RED	CN E-X	CN H-X	CO(4+)
0.40000+004	0.	0.32935-004	0.81258-026	0.10980-028	0.13753-033
0.60000+004	0.13256-014	0.10525-003	0.11653-024	0.19363-027	0.42056-032
0.80000+004	0.87773-013	0.15728-003	0.15368-023	0.31431-026	0.11865-030
0.10000+005	0.19116-011	0.21970-003	0.19472-022	0.49034-025	0.32197-029
0.12000+005	0.16889-010	0 11603-003	0.24158-021	0.74917-024	0.85602-028
0.14000+005	0.26356-010	0.61615-004	0.29627-020	0.11315-022	0.22504-026
0.16000+005	0.77793-009	0.23787-004	0.36097-019	0.16980-021	0.58786-025
0.18000+005	0.58768-007	0.70934-005	0.43816-018	0.25386-020	0.15301-023
0.20000+005	0.13788-005	0.18701-005	0.53070-017	0.37872-019	0.39740-022
0.22000+005	0.21010-004	0.44494-006	0.64198-016	0.56430-018	0.10309-020
0.24000+005	0.22749-003	0.93808-007	0.77604-015	0.84020-017	0.26723-019
0.26000+005	0.23798-002	0.15902-007	0.93769-014	0.12505-015	0.69245-018
0.28000+005	0.48813-003	0.23180-008	0.11327-012	0.18606-014	0.17938-016
0.30000+005	0.12414-004	0.28053-009	0.13682-011	0.27681-013	0.46464-015
0.32000+005	0.10138-005	0.26606-010	0.16621-010	0.41178-012	0.12034-013
0.34000+005	0.17910-007	0.18454-011	0.20081-009	0.61254-011	0.31167-012
0.36000+005	0.30806-008	0.84607-013	0.24309-008	0.91117-010	0.80716-011
0.38000+005	0.37406-010	0.19589-014	0.29371-007	0.13588-008	0.20904-009
0.40000+005	0.13010-010	0.	0.35397-006	0.20216-007	0.54134-008
0.42000+005	0.69667-012	0.	0.34702-005	0.29609-006	0.14020-006
0.44000+005	0.10166-013	0.	0.17425-004	0.28210-005	0.35745-005
0.46000+005	0.60152-015	0.	0.43643-004	0.11376-004	0.77036-004
0.48000+005	0.88512-016	0.	0.94267-004	0.25640-004	0.93021-003
0.50000+005	0.43113-017	0.	0.19301-003	0.54188-004	0.38329-002
0.52000+005	0.26177-018	0.	0.40350-003	0.11940-003	0.94365-002
0.54000+005	0.10114-021	0.	0.71894-003	0.31936-003	0.19582-001

Table 7 (continued)

Wave Number, CM^{-1}	Band System Opacities, CM^{-1}				
	CN VLT	CN RED	CN E-X	CN H-X	CO(4+)
0.56000+005	0.	0.	0.10803-002	0.28494-003	0.38632-001
0.58000+005	0.	0.	0.15562-002	0.43117-003	0.83060-001
0.60000+005	0.	0.	0.18525-002	0.57078-003	0.15327+000
0.62000+005	0.	0.	0.21381-002	0.72359-003	0.23249+000
0.64000+005	0.	0.	0.14899-002	0.87851-003	0.33524+000
0.66000+005	0.	0.	0.90220-003	0.78894-003	0.38462+000
0.68000+005	0.	0.	0.48915-003	0.69110-003	0.47296+000

Wave Number, cm^{-1}	Total Absorption Coefficient, cm^{-1}	B(W,T), watts/cm^2-ster	Emission, watts/cm^3-ster
0.40000+004	0.43746-003	0.39350-001	0.17214-004
0.60000+004	0.11704-003	0.63781-003	0.74651-005
0.80000+004	0.15731-003	0.79962-001	0.12579-004
0.10000+005	0.21972-003	0.86412-001	0.18986-004
0.12000+005	0.11608-003	0.84575-001	0.98177-005
0.14000+005	0.61695-004	0.77049-001	0.47536-005
0.16000+005	0.23883-004	0.66460-001	0.15872-005
0.18000+005	0.72562-005	0.54905-001	0.39840-006
0.20000+005	0.33335-005	0.43804-001	0.14602-006
0.22000+005	0.21500-004	0.33956-001	0.73007-006
0.24000+005	0.22759-003	0.25695-001	0.58480-005
0.26000+005	0.23799-002	0.19051-001	0.45339-004
0.28000+005	0.48828-003	0.13879-001	0.67770-005
0.30000+005	0.12617-004	0.99589-002	0.12566-006
0.32000+005	0.12398-005	0.70518-002	0.87427-008
0.34000+005	0.25483-006	0.49352-002	0.12577-008
0.36000+005	0.24834-006	0.34184-002	0.84892-009
0.38000+005	0.27713-006	0.23459-002	0.65010-009
0.40000+005	0.62899-006	0.15966-002	0.10042-008
0.42000+005	0.41577-005	0.10785-002	0.44840-008

TABLE 7 (conintued)

Wave Number, cm^{-1}	Total Absorption Coefficient, cm^{-1}	B(W,T), $watts/cm^2$-ster	Emission, $watts/cm^3$-ster
0.44000+005	0.24073-004	0.72355-003	0.17418-007
0.46000+005	0.13232-003	0.48244-003	0.63834-007
0.48000+005	0.10504-002	0.31985-003	0.33597-006
0.50000+005	0.40803-002	0.21095-003	0.86076-006
0.52000+005	0.99597-002	0.13847-003	0.13791-005
0.54000+005	0.20621-001	0.90484-004	0.18658-005
0.56000+005	0.39998-001	0.58886-004	0.23553-005
0.58000+005	0.85048-001	0.38176-004	0.32467-005
0.60000+005	0.15569+000	0.24661-004	0.38395-005
0.62000+005	0.23535+000	0.15878-004	0.37368-005
0.64000+005	0.33760+000	0.10191-004	0.34405-005
0.66000+005	0.38632+000	0.65217-005	0.25194-005
0.68000+005	0.47414+000	0.41621-005	0.19734-005

Total Emission = 0.31484+000 $watts/cm^3$-ster

TABLE 8

DETAILED SPECTRAL DISTRIBUTION OF OPACITY
OF CN VIOLET BAND
($T = 5735^{\circ}K$, $P = 0.172$ atm)

Mole-Fraction for CN VLT = 0.37560-002

Wave Number, cm^{-1}	Opacity, cm^{-1}
0.21000+005	0.
0.21400+005	0.
0.21800+005	0.70214-004
0.22200+005	0.17970-003
0.22600+005	0.61393-004
0.23000+005	0.49035-005
0.23400+005	0.38785-006
0.23800+005	0.12719-002
0.24200+005	0.16983-002
0.24600+005	0.21432-003
0.25000+005	0.16950-004
0.25400+005	0.13405-005
0.25800+005	0.16090-001
0.26200+005	0.14051-001
0.26600+005	0.11970-002
0.27000+005	0.94659-004
0.27400+005	0.74856-005
0.27800+005	0.13008-002
0.28200+005	0.49598-002
0.28600+005	0.39264-003
0.29000+005	0.31049-004
0.29400+005	0.34936-005
0.29800+005	0.37815-004

TABLE 9

EQUILIBRIUM SPHERE-CONE RADIATIVE HEAT TRANSFER

Position (Figure 13)	R_1, watts/cm^2 (optically thin)	R_2, watts/cm^2 (with self-absorption)	R_3, watts/cm^2 (with self-absorption) and boundary layer correction)
1	5.6	5.4	4.6
2	5.2	5.1	4.3
3	3.1	3.0	2.6
4	5.6	5.2	4.8
5	9.2	8.1	7.6
6	10.0	8.5	8.0

is given and includes the effects of self-absorption and viscous-inviscid coupling. It was found that only CO(4+) emission was subject to significant self-absorption. The magnitudes of the self-absorption and boundary-layer coupling are seen by comparing the three columns.

4.2 NON-EQUILIBRIUM FLOW OVER A SPHERE-CONE AND A SPHERE-CAP

4.2.2 NON-EQUILIBRIUM INVISCID FLOW PROPERTIES

a. Sphere Cone. The bow shock and shock layer streamline positions for the non-equilibrium sphere cone flow field are shown in Figure 17. For comparison, the bow shock positions for the equilibrium solution and for a first approximation method of integral relation non-equilibrium solution are also shown. It is seen that the non-equilibrium shock layer detachment distance exceeds the equilibrium result by a factor of two in some regions. The difference between these two cases arises from the lower shock layer densities and the more extensive region of subsonic flow in the non-equilibrium case. In the equilibrium calculation the temperature is lower throughout the flow field. This causes the gas density to be high and it also causes almost all of the flow to be supersonic at the sphere-cone junction. In the non-equilibrium calculation, the temperature is higher and an extensive region of subsonic flow exists aft of the sphere-cone junction. Since the standoff distance varies inversely with density and velocity, the non-equilibrium standoff distance is larger than the equilibrium value. Note also that the integral relation solution for the non-equilibrium shock layer thickness somewhat exceeds the time-dependent result, but that the errors are not nearly as large as in the equilibrium case (Figure 13). The reason that the integral solution is more accurate in the non-equilibrium case is that the sonic line in the one strip integral approximation, which extends linearly from the bow shock in the sphere-cone junction region to the rounded corner in the base region of the body, more closely approximates the actual flow conditions.

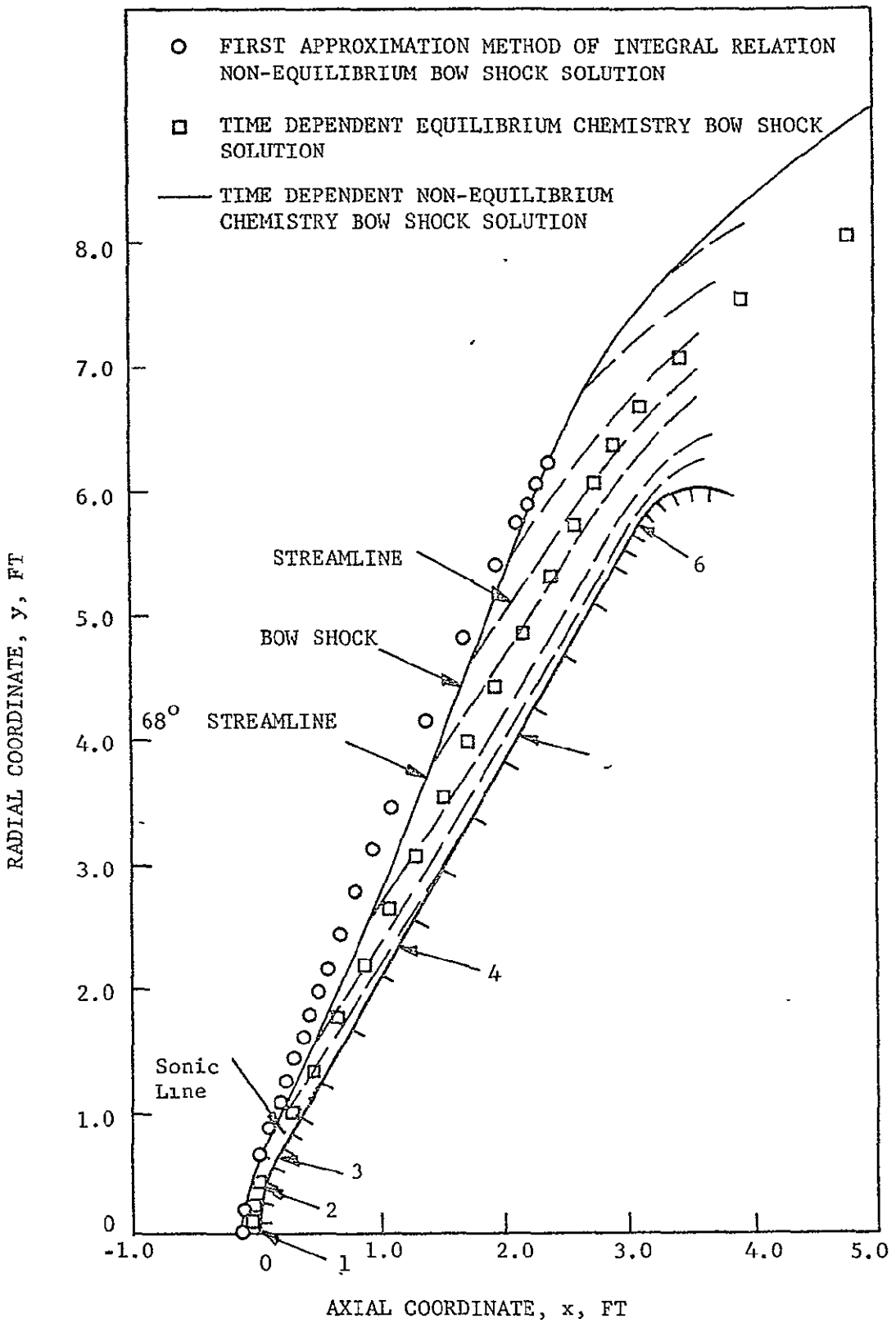

FIGURE 17. BLUNT SPHERE-CONE BODY, NON-EQUILIBRIUM SHOCK SHAPE, AND STREAMLINE POSITIONS

The body pressure distribution is shown in Figure 18. A Newtonian result is also shown for comparison. As in the case of the equilibrium flow, the two prominent features of the pressure distribution are the rapid decrease in pressure on the sphere-cone and the pressure recovery at the sphere-cone junction to a pressure plateau in the conical region. Even though the subsonic flow region extends beyond the sphere-cone junction, the non-equilibrium pressure distribution is very similar to the equilibrium result, although the actual pressure level is somewhat lower. Note also that the Newtonian model provides a useful approximation to the non-equilibrium pressure distribution.

The flow properties throughout the inviscid region of the non-equilibrium sphere-cone flow field are given in further detail in Table 10. The notation follows that used in Table 5 and discussed in Section 4.1.1. Each body point is shown in Figure 17. Data is given along rays normal to the body surface. The non-equilibrium species distributions are discussed in Section 4.2.3.

b. Sphere-Cap. The sphere-cap bow shock and streamline field obtained from the time dependent finite difference solution are shown in Figure 19. The bow shock is nearly concentric with the body except in the region of the corner. At the corner position, the sonic line extends in a normal direction from the body curving downstream slightly and then upstream to the bow shock.

The inviscid result is based in a constant $\gamma = 1.225$, which corresponds to a shock layer with fully equilibrated rotational and vibrational energy modes and frozen free stream chemical species. In the course of performing the non-equilibrium streamline integrations, it was found that the non-equilibrium chemical species relaxation zone is only 30% of the shock layer thickness. Thus more than two-thirds of the shock layer is nearly in thermochemical equilibrium and the assumption of frozen chemical species shock layer is in error. This error in shock layer chemistry model causes

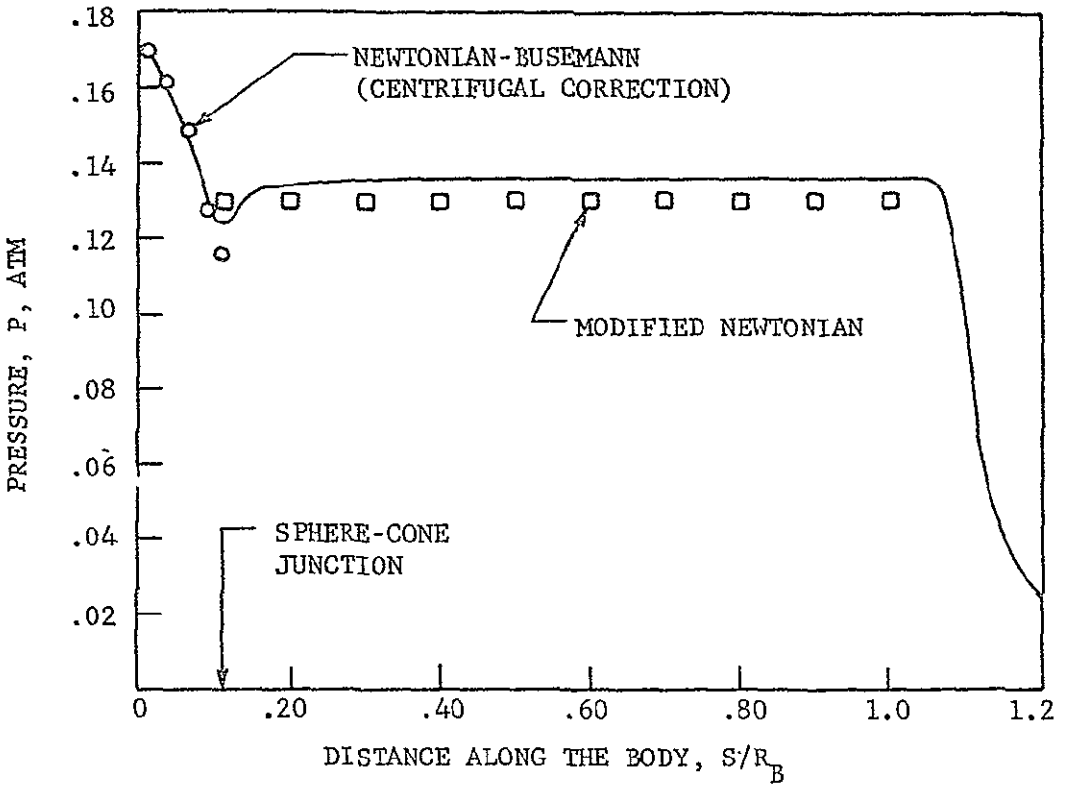

FIGURE 18. NON-EQUILIBRIUM SURFACE PRESSURE ON THE SPHERE-CONE

TABLE 10

NON-EQUILIBRIUM INVISCID SHOCK LAYER PROPERTIES ON THE SPHERE-CONE

Body Station	Arc Length on Surface, Ft	Standoff Distance, Ft	x, Ft	y, Ft	Pressure, atm	Enthalpy Kcal/100 gm	Flow Speed, fps
1.Shock	.0785	0.107	-.1015	0.0854	0.1452	338	2268.6
.625 ε			-.0605	.0827	0.1526	341	1460.0
.375 ε			-.0338	.0809	0.1559	342	1021.1
Body			.0051	.0783	0.1612	343	653.2
2.	.235	0.108	-.0799	.2545	.1381	322	4348.3
			.0393	.2465	.1457	332	3215.0
			.0130	.2412	.1488	336	2573.5
			.0256	.2336	.1516	340	1823.9
3.	.392	0.110	-.0365	.4210	.1367	309	5580.0
			.1835	.4070	.1403	319	4700.0
			.0280	.3980	.1419	325	4051.2
			.06612	.3849	.1435	333	3024.1
4.	.549	0.110	.02227	.5841	.1181	268	8230.3
			.06221	.5638	.1214	293	6700.0
			.0895	.5499	.1226	308	5662.6
			.1261	.5296	.1230	324	4151.5
5.	.706	0.113	.0949	.7287	.1163	252	9046.8
			.1353	.7054	.1172	276	7760.0
			.1616	.6902	.1174	294	6685.7
			.2000	.6680	.1183	319	4663.1
6.	.863	0.130	.1663	.8689	.1194	253	8995.6
			.2093	.8440	.1220	270	8120.1
			.2374	.8278	.1233	286	7150.1
			.2786	.8040	.1253	317	4895.3

TABLE 10 (continued)

Body Station	Arc Length on Surface, Ft	Standoff Distance, Ft	x, Ft	y, Ft	Pressure, atm	Enthalpy Kcal/100 gm	Flow Speed, fps
7.	1.021	0.132	.2352	1.010	.1224	258	8779.2
			.2819	.9835	.1254	267	8261.7
			.3123	.9659	.1267	281	7502.3
			.3571	.9401	.1283	312	5347.8
8.	1.346	0.177	.3666	1.311	.1268	272	8039.4
			.4253	1.277	.1290	271	8057.1
			.4637	1.255	.1300	275	7828.9
			.5200	1.222	.1305	295	6583.4
9.	1.841	0.232	.5657	1.7671	.1269	261	8139.7
			.6429	1.723	.1292	271	8045.3
			.6933	1.693	.1301	274	7915.4
			.7674	1.651	.1306	288	7049.7
10.	2.336	0.300	.7541	2.229	.1311	284	7280.0
			.8539	2.172	.1328	280	7582.9
			.9190	2.134	.1334	278	7689.2
			1.015	2.079	.1336	284	7278.0
11.	2.830	0.368	.9433	2.691	.1260	272	7998.1
			1.065	2.621	.1287	276	7781.7
			1.145	2.575	.1297	276	7771.8
			1.262	2.507	.1302	282	7451.1
12.	3.325	0.437	1.131	3.154	.1316	286	7217.0
			1.276	3.070	.1330	282	7437.3
			1.371	3.016	.1336	280	7549.5
			1.509	2.936	.1339	282	7411.8

TABLE 10 (continued)

Body Station	Arc Length on Surface, Ft	Standoff Distance, Ft	x, Ft	y, Ft	Pressure, atm	Enthalpy Kcal/100 gm	Flow Speed, fps
13.	3.820	0.508	1.317	3.618	.1257	275	7852.5
			1.485	3.521	.1286	278	7649.8
			1.595	3.457	.1296	278	7653.8
			1.757	3.364	.1303	281	7516.2
14.	4.314	0.571	1.509	4.078	.1295	280	7563.3
			1.699	3.969	.1314	281	7508.2
			1.822	3.897	.1322	280	7525.9
			2.004	3.793	.1328	282	7405.9
15.	4.809	0.644	1.694	4.543	.1282	280	7549.5
			1.907	4.420	.1300	280	7551.4
			2.047	4.339	.1308	280	7567.2
			2.251	4.221	.1313	282	7433.4
16.	5.304	0.718	1 885	5.004	.1265	275	7846.6
			2.122	4.866	.1294	279	7604.6
			2.276	4.778	.1305	280	7565.2
			2.499	4.644	.1315	283	7346.8
17.	5.798	0.776	2.074	5.465	.1301	281	7478.7
			2.339	5.312	.1313	281	7510.1
			2.507	5.216	.1319	280	7525.9
			2.746	5.078	.1327	285	7252.4
18.	6.124	0.821	2.194	5.773	.1291	281	7462.9
			2.481	5.607	.1306	280	7527.8
			2.659	5.504	.1314	280	7545.5
			2.909	5.360	.1327	285	7222.9

TABLE 10 (continued)

Body Station	Arc Length on Surface, Ft	Standoff Distance, Ft	x, Ft	y, Ft	Pressure, atm	Enthalpy Kcal/100 gm	Flow Speed, fps
19.	6.281	0.851	2.252	5.920	.1273	280	7557.3
			2.557	5.745	.1298	280	7561.3
			2.740	5.639	.1308	280	7567.2
			2.988	5.496	.1323	286	7191.4
20.	6.438	0.881	2.311	6.068	.1270	279	7608.5
			2.651	5.872	.1293	280	7581.0
			2.836	5.765	.1302	280	7553.4
			3.066	5.632	.1307	286	7213.0
21.	6.595	0.920	2.428	6.326	.1213	270	8106.3
			2.775	6.055	.1219	275	7856.4
			2.951	5.918	.1187	274	7901.7
			3.153	5.762	.1079	275	7858.4
22.	6.752	1.060	2.628	6.720	.1130	256	8863.8
			2.938	6.305	.1062	265	8395.5
			3.091	6.100	.0967	262	8535.2
			3.263	5.872	.0734	258	8757.6
23.	6.909	1.308	2.914	7.169	.0968	225	1030.4
			3.157	6.552	.08613	252	9050.7
			3.273	6.260	.07353	246	9200.3
			3.397	5.950	.0470	244	9440.3
24.	7.065	1.698	3.356	7.686	.0794	184	11954.8
			3.454	6.793	.0657	238	9725.6
			3.500	6.393	.0533	236	9826.0
			3.547	5.990	.0291	234	9946.0

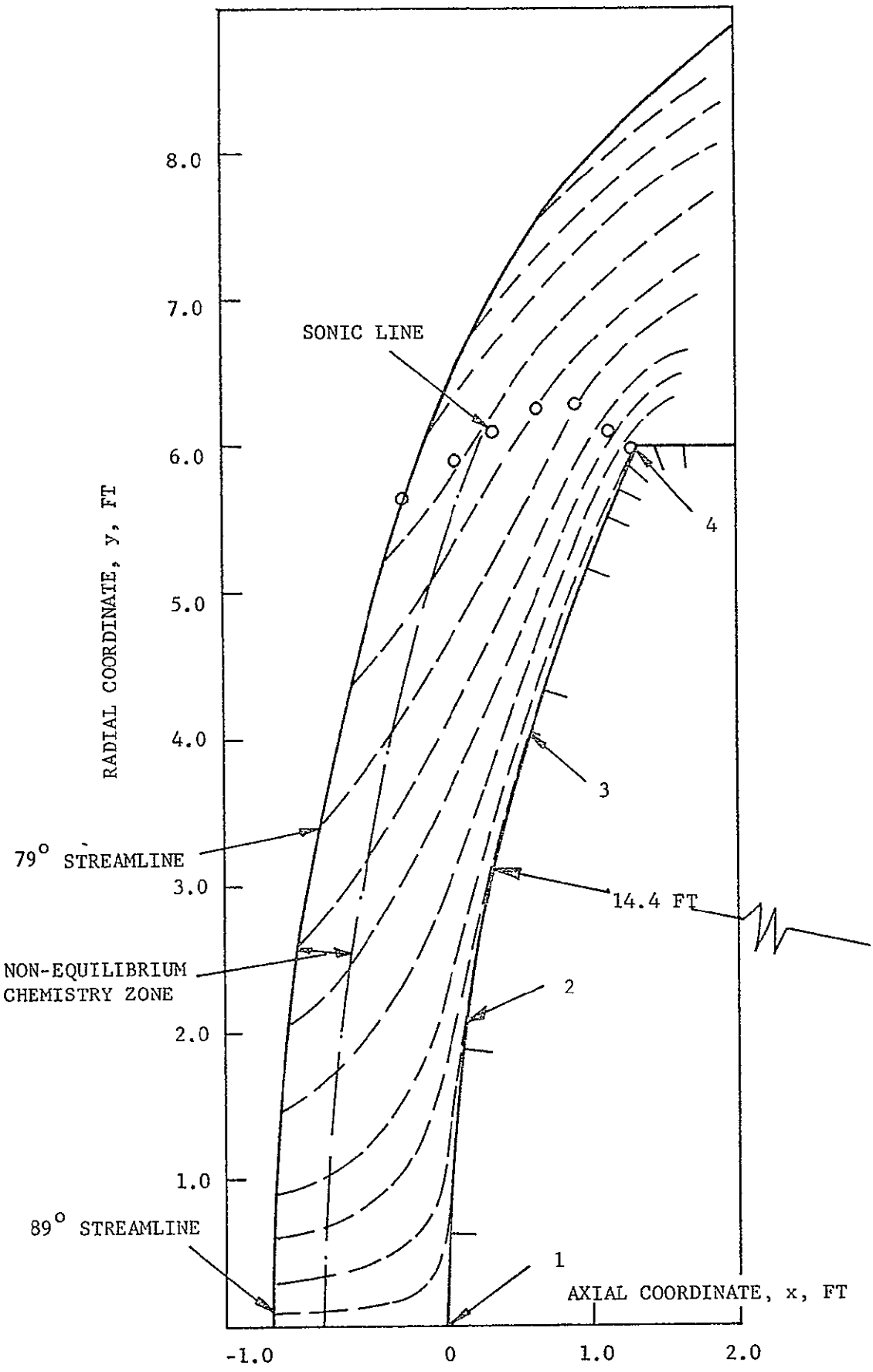

FIGURE 19. SPHERE-CAP BODY, NON-EQUILIBRIUM SHOCK SHAPE AND STREAMLINE POSITIONS

the shock layer densities to be underestimated and the shock layer thickness to be overestimated. Since the shock layer volume is an important radiative heat transfer variable, the shock detachment distance has been adjusted in the radiation calculation to include the influence of the equilibrium property zone. This adjustment was accomplished by multiplying the existing detachment distance by a weighted average of equilibrium and $\gamma = 1.225$ sphere-cap solutions. The error in the inviscid chemistry model does not significantly affect the pressure field nor the relative location of the streamlines.

This error in chemistry also affects the stagnation point convective heat transfer and the convective heat transfer distribution. The only heat transfer variables significantly influenced are the boundary layer edge velocity and the stagnation point velocity derivative. These variables have been adjusted to account for the equilibrium chemistry effects. The stagnation point velocity gradient is reduced by 21% from 697 sec^{-1} to 547 sec^{-1}. The stagnation point pressure, on the other hand, is increased only 1% by the equilibrium chemistry effect.

In Figure 20, the sphere-cap surface pressure as a function of the ratio of body surface distance to base radius is shown. For comparison, the Newtonian-Busemann and the modified Newtonian pressure distributions are also indicated. The Newtonian-Busemann model is a better approximation of the sphere-cap pressure distribution than is the modified Newtonian result. Both of these approximate models, however, are in error in the region of the corner where a local acceleration of the flow occurs.

The flow field properties throughout the sphere-cap inviscid shock layer are given in further detail in Table 11. The notation follows that used in Table 5 and discussed in Section 4.1.1. The location of each body point is shown in Figure 19. Data is given along rays normal to the body surface. The final column in Table 11 is the enthalpy of the

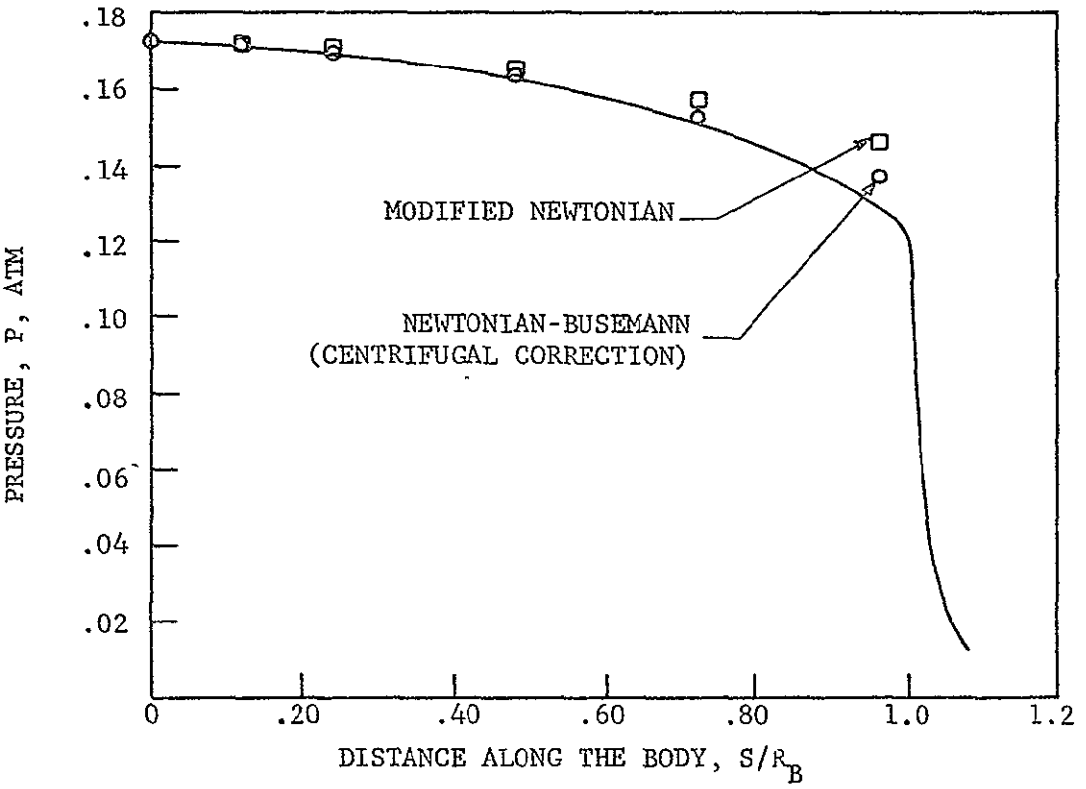

FIGURE 20. NON-EQUILIBRIUM SURFACE PRESSURE ON THE SPHERE-CAP

TABLE 11

NON-EQUILIBRIUM INVISCID SHOCK LAYER PROPERTIES ON THE SPHERE-CAP

Body Station	Arc Length on Surface, Ft	Standoff Distance, Ft	x, Ft	y, Ft	Pressure, atm	Enthalpy Kcal/100gm	Flow Speed, fps	Enthalpy, with Radiation Loss Kcal/100gm
1.Shock	0.04	1.190	-1.190	0.0	.161	339	1987.2	339
.625e			- .734	0.0	.153	342	1042.8	325
.375e			- .436	0.0	.157	343	500.0	316
Body			0	0.0	.163	343	110.2	307
2.	0.629	1.201	-1.187	0.683	.144	338	2184	338
			- .718	0.662	.152	341	1298	324
			- .423	0.648	.155	342	807	316
			.014	0.628	.160	343	433	307
3.	1.888	1.233	-1.100	2.044	.142	331	3325	331
			- .628	1.981	.149	338	2282	320
			- .325	1.940	.152	340	1771	313
			.123	1.880	.155	342	1259	306
4.	3.147	1.243	- .870	3.395	.137	322	4403	322
			- .402	3.288	.147	332	3207	318
			- .108	3.219	.150	335	2754	309
			.341	3.117	.152	338	2105	304
5.	4.406	1.270	- .550	4.700	.133	307	5686	307
			- .113	4.583	.138	321	4506	309
			.205	4.483	.140	327	3817	307
			.668	4.337	.142	334	2951	302
6.	5.296	1.336	- .288	5.655	.126	294	6690	294
			.193	5.470	.129	312	5273	303
			.505	5.350	.129	321	4625	303
			.961	5.174	.128	329	3640	302

TABLE 11 (continued)

Body Station	Arc Length on Surface, Ft	Standoff Distance, Ft	x, Ft	y, Ft	Pressure, atm	Enthalpy Kcal/100gm	Flow Speed, fps	Enthalpy, with Radiation Loss Kcal/100gm
7.	5.665	1.337	- .142	6.020	.1225	287	7142	287
			.334	5.823	.124	308	5647	300
			.643	5.695	.123	317	4879	299
			1.09	5.508	.1226	326	3935	300
8.	5.868	1.349	.005	6.348	.1188	275	7870	275
			.458	6.297	.1215	303	6040	297
			.751	5.935	.1219	314	5116	298
			1.176	5.699	.1212	325	4073	300
9.	6.048	1.395	.230	6.812	.1153	263	8559	263
			.630	6.441	.1165	290	6591	285
			.886	6.205	.1183	311	5391	297
			1.253	5.865	.1179	323	4289	298
10.	6.163	1.546	.514	7.285	.1004	234	9901	234
			.843	6.768	.0835	269	8185	264
			1.051	6.443	.0659	270	8120	255
			1.353	5.982	.0368	244	9466	219
11.	6.300	1.871	.830	7.756	.0837	198	11451	198
			1.123	7.063	.0671	253	9031	249
			1.270	6.635	.0544	260	8677	245
			1.475	6.000	.0281	243	9523	218
12.	6.475	2.307	1.350	8.288	.068	155	13025	155
			1.516	7.370	.0514	234	9916	230
			1.572	6.812	.0402	245	9385	231
			1.650	6.000	.0119	221	1047	197

TABLE 11 (continued)

Body Station	Arc Length on Surface, Ft	Standoff Distance, Ft	x, Ft	y, Ft	Pressure, atm	Enthalpy Kcal/100gm	Flow Speed, fps	Enthalpy, with Radiation Loss Kcal/100gm
13.	6.825	2.850	2.000	8.850	.0630	137	13615	137
			2.000	7.638	.0356	220	10566	217
			2.000	6.961	.0249	226	10290	211
			2.000	6.000	.0150	186	11900	164

fluid, corrected for radiation cooling, which is discussed in further detail in Section 4.2.3. The non-equilibrium species distributions are also discussed in Section 4.2.3.

4.2.2 NON-EQUILIBRIUM CONVECTIVE HEAT TRANSFER

a. Sphere-Cone. The non-equilibrium sphere-cone convective heat flux versus distance along the body is shown in Figure 21. For comparison, the equilibrium convective heat transfer distribution is also shown. The stagnation point convective heat transfer for the non-equilibrium case is slightly larger than the equilibrium result. This increase is an inviscid effect, arising from a higher stagnation point velocity gradient in the non-equilibrium case (7570 sec^{-1}), than in the equilibrium case (6340 sec^{-1}). The sphere-cap vorticity interaction effect is actually smaller in the non-equilibrium case (1.06) than in the equilibrium case (1.12). The CO_2 composition effect is the same for both cases. The convective heat transfer in the conical region of the body is slightly less for non-equilibrium flow than for equilibrium flow because the boundary layer edge velocities are slightly lower.

b. Sphere-Cap. The non-equilibrium sphere-cap convective heat flux distribution is shown in Figure 22. The heat transfer distribution is quite flat over most of the body, but drops sharply in the corner region. The vorticity interaction effect for the sphere-cap case is negligible because of the large nose radius.

It was found that the stagnation point velocity gradient exceeds the modified Newtonian result by approximately 19%; hence the sphere-cap stagnation point heat transfer rate is 9% larger than the modified Newtonian result. The effect of the CO_2 composition on the convective heat transfer is assumed to be solely dependent on the free stream molecular weight and increases the convective heat transfer rate by approximately 8% over that for air at the same flight conditions. Radiation absorption in the boundary layer has a negligible influence on convective heat transfer.

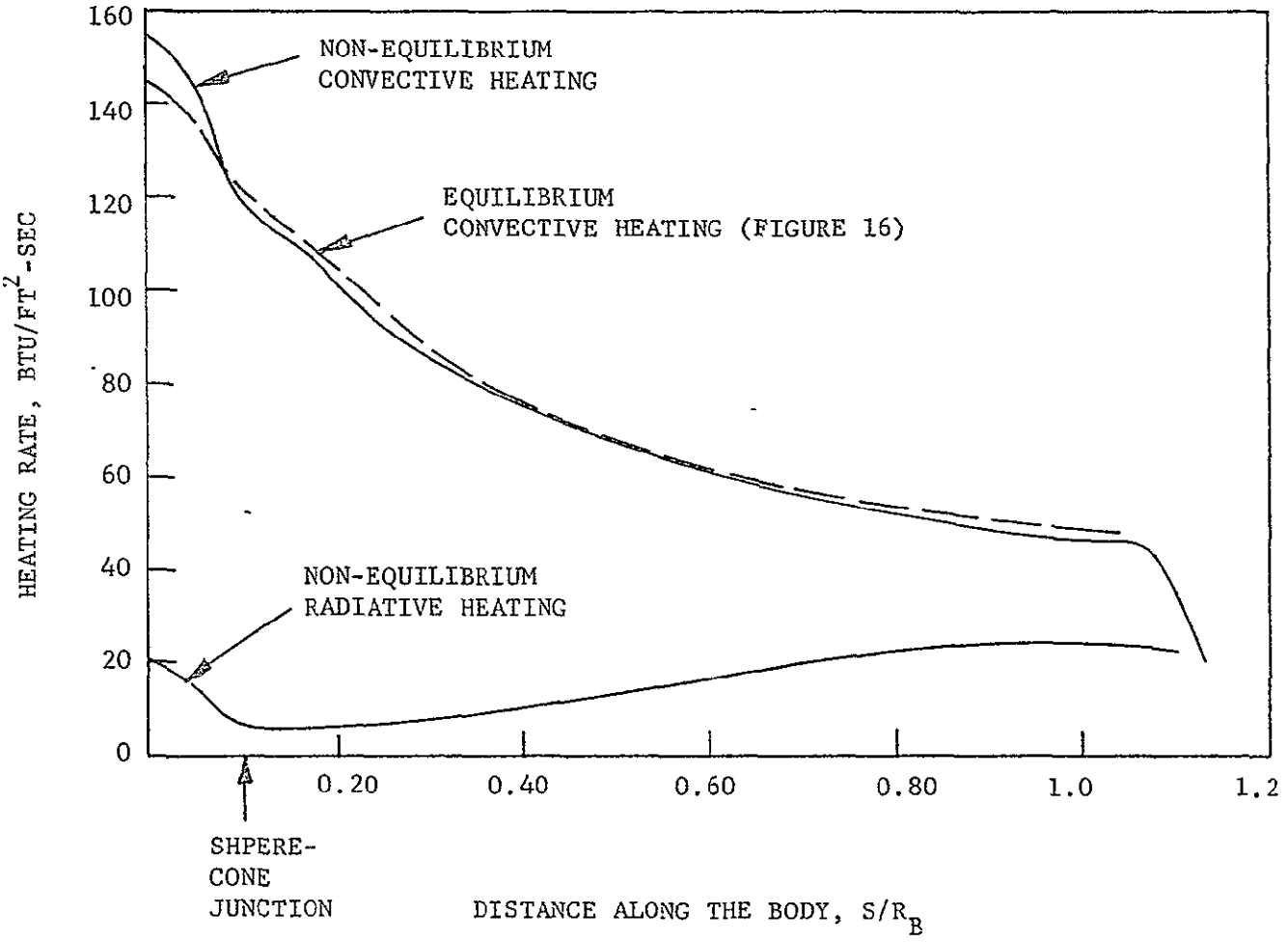

FIGURE 21. SPHERE-CONE NON-EQUILIBRIUM CHEMISTRY CONVECTIVE AND RADIATIVE HEAT TRANSFER DISTRIBUTIONS

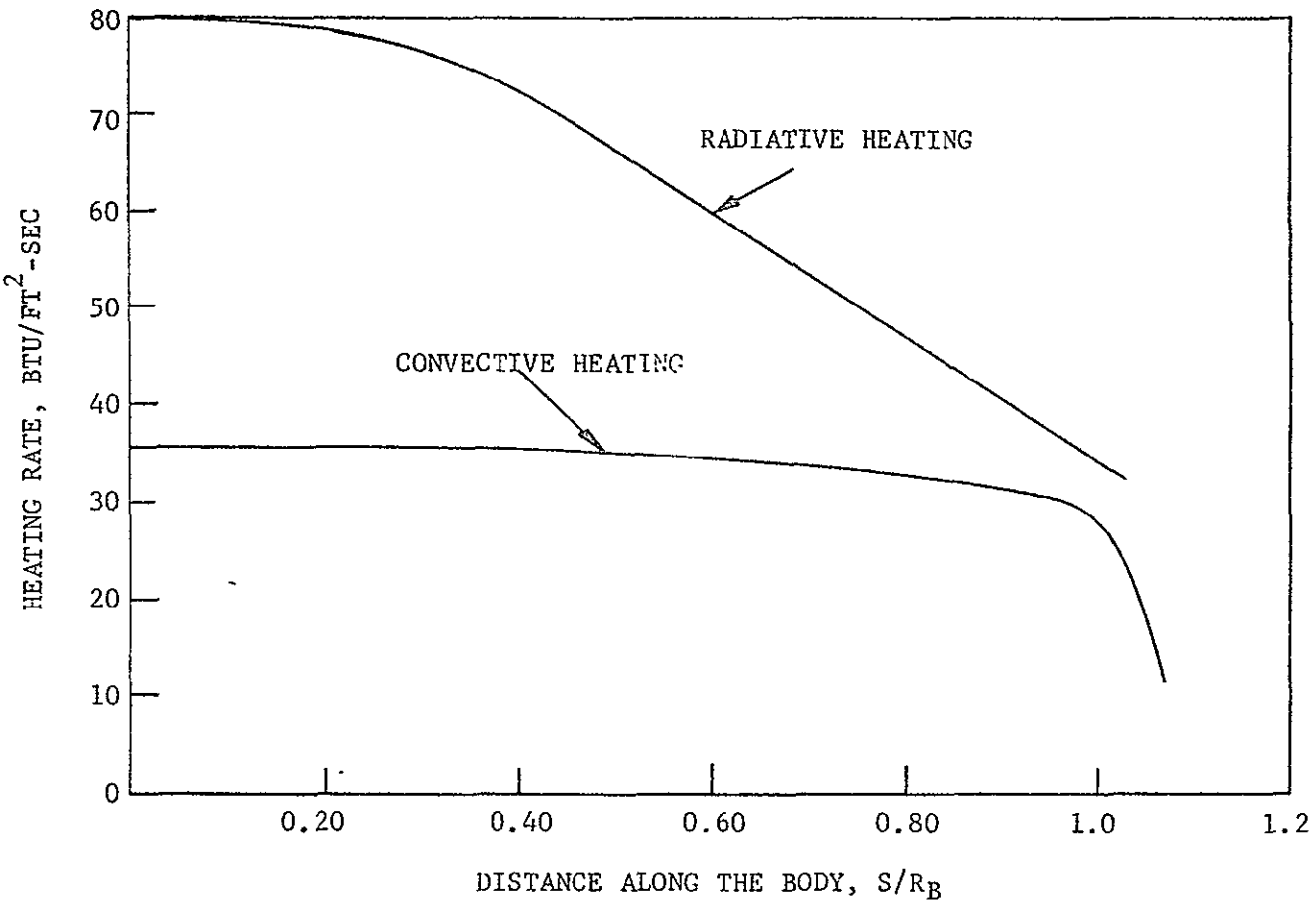

FIGURE 22. SPHERE-CAP NON-EQUILIBRIUM CHEMISTRY CONVECTIVE AND RADIATIVE HEAT TRANSFER DISTRIBUTIONS

4.2.3 NON-EQUILIBRIUM RADIATIVE HEAT TRANSFER

a. Non-Equilibrium Concentrations of Significant Species. The non-equilibrium species profiles on three streamlines are shown in Figures 23, 24, and 25 as a function of distance along the streamline. Gas temperature and density profiles are also shown. The three streamlines originate at shock angles of 89°, 79°, and 68°, respectively to the flow direction. The 89° and 79° streamlines correspond to the sphere-cap streamlines indicated by arrows on Figure 19; the 68° streamline corresponds to the sphere-cone streamline indicated by the arrow on Figure 17. The 89° and 79° streamline results are also representative of the non-equilibrium flow in the nose region of the sphere-cone, but with a change in scale that correctly transforms the convective derivative (a scale change by a factor of about 12).

In Figures 23, 24, and 25, the overshoot in CN concentration is seen to be moderate; The CN emission, Figures 26 and 27, overshoots more strongly than does the CN concentration because of the high non-equilibrium gas temperature ($\sim 9000^{\circ}K$) near the peak in the CN concentration. The CN* concentration is seen to overshoot by a factor of about 10. The CO* concentration is not shown because the rates are too uncertain. The electron-density profile is also shown, although its contribution to the radiation heat transfer is negligible. However, the information may be useful in communication black-out studies. It is seen that a slight electron density overshoot occurs; the location of the peak electron density is a factor of 5 to 10 further from the shock than is the peak CN radiation emission.

b. Sphere-Cone Non-Equilibrium Radiative Heat Transfer. From the results of Figures 23, 24, and 25, it is seen that non-equilibrium gas properties extend over the full shock layer on the sphere-cone.

The major radiation to the sphere-cone originates from the non-equilibrium overshoot of the CN red and CN violet bands. The volume emission from these bands along each of the streamlines noted above is shown in

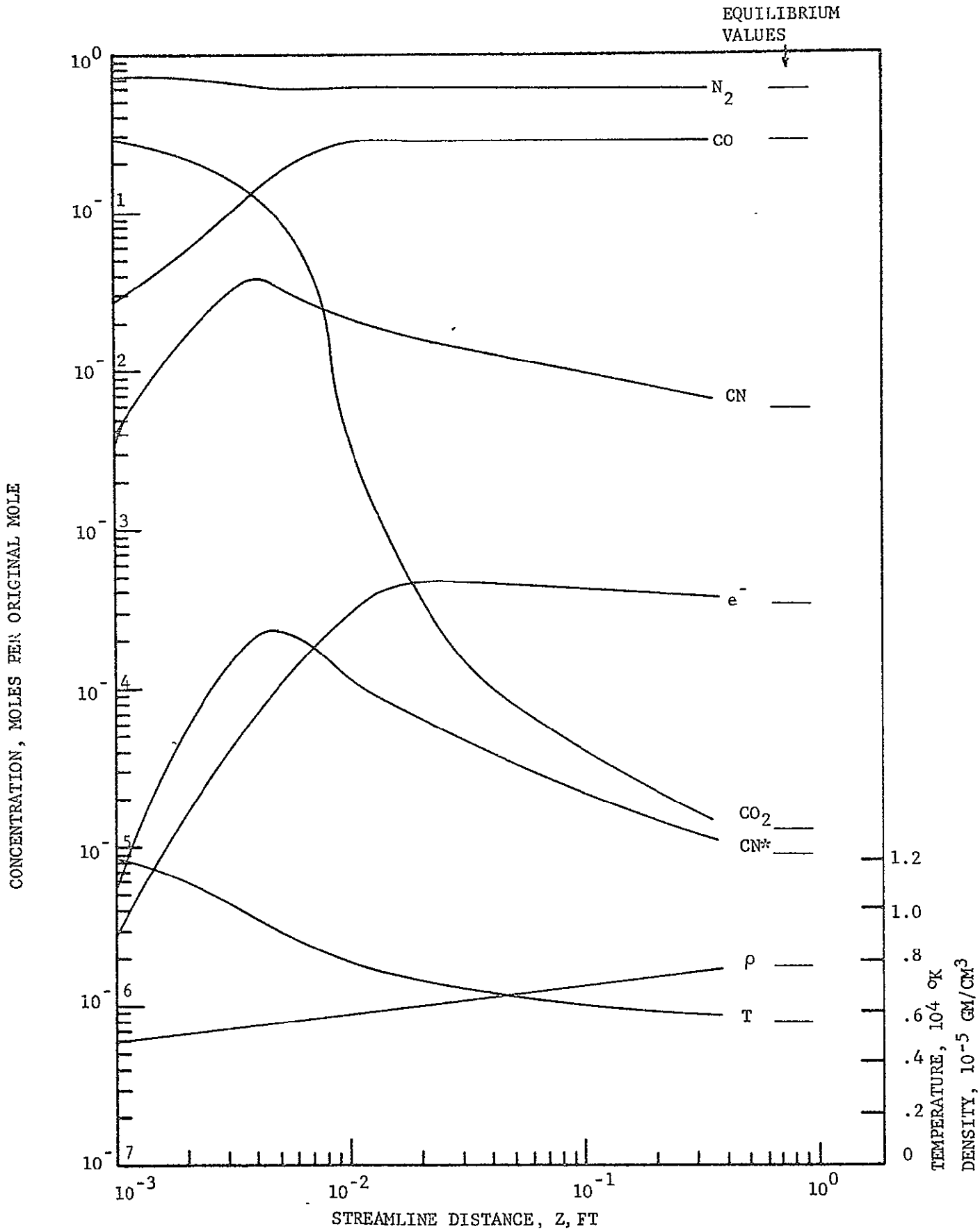

FIGURE 2?. NON-EQUILIBRIUM SPECIES AND TEMPERATURE AND DENSITY PROFILES ALONG THE 89° SPHERE CAP STREAMLINE. EQUILIBRIUM VALUES ARE ALSO SHOWN.

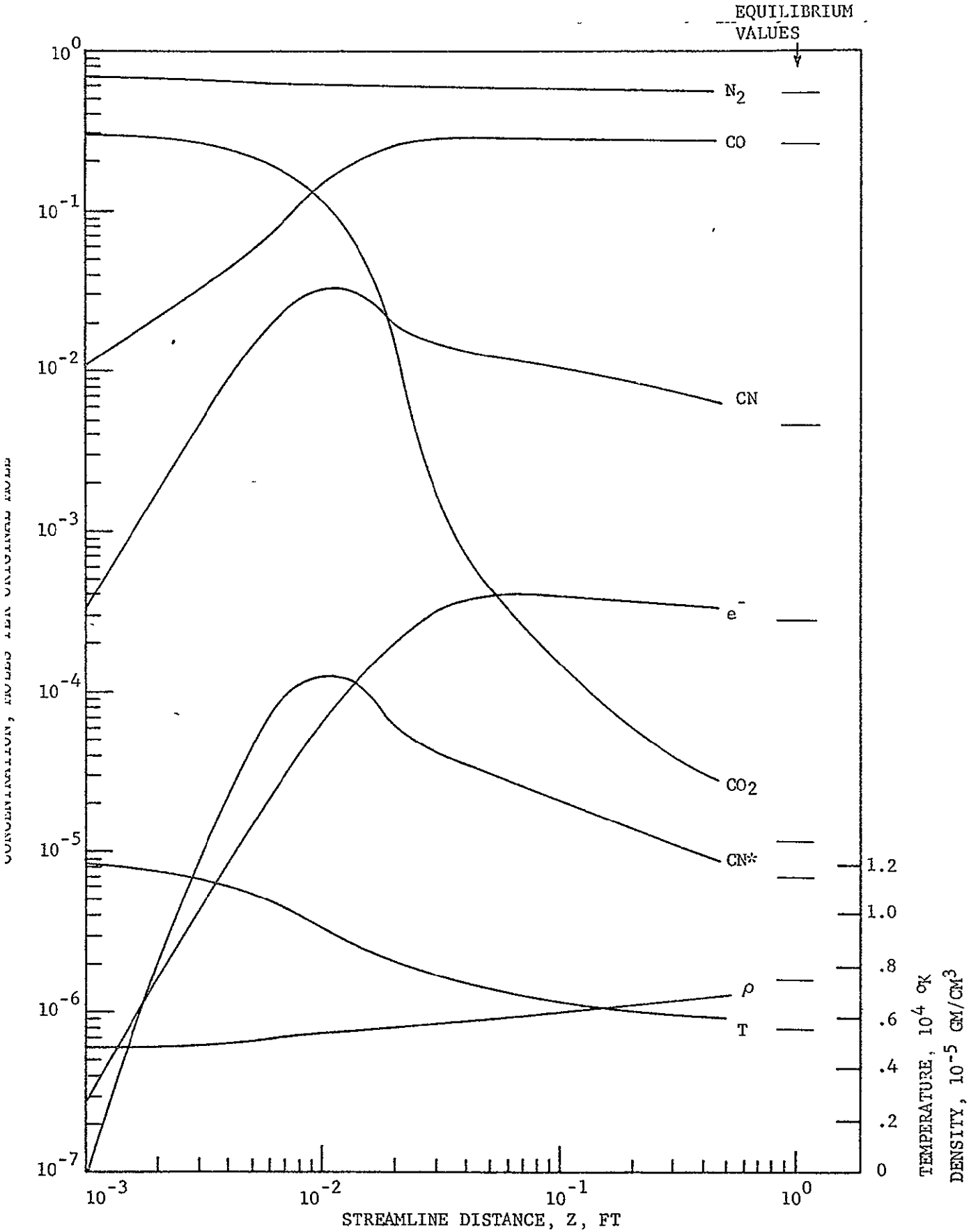

FIGURE 24. NON-EQUILIBRIUM SPECIES AND TEMPERATURE AND DENSITY PROFILES ALONG THE 79° SPHERE-CAP STREAMLINE. EQUILIBRIUM VALUES ARE ALSO SHOWN.

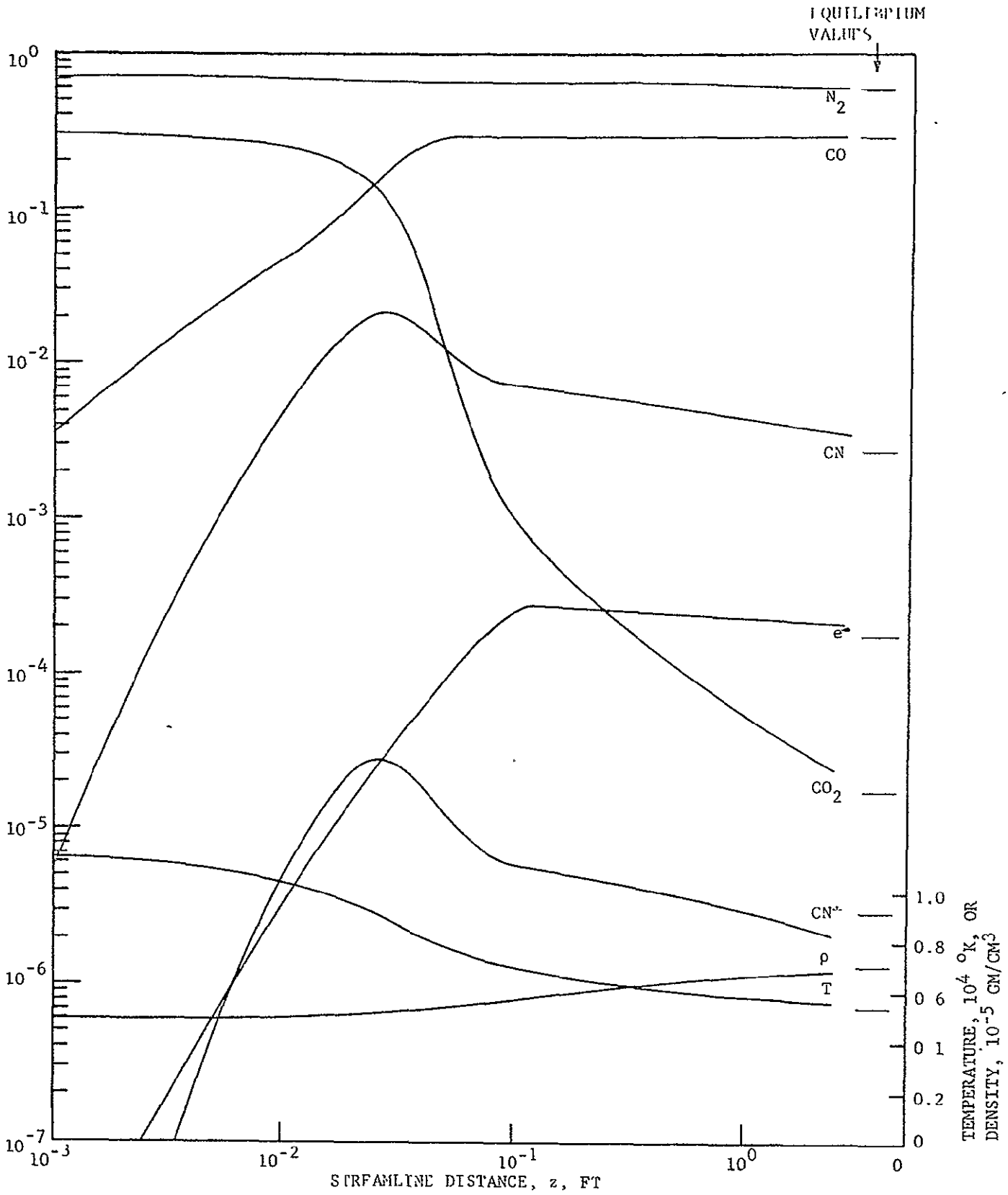

FIGURE 25. NON-EQUILIBRIUM PROFILES OF SPECIES CONCENTRATION AND TEMPERATURE AND DENSITY ALONG THE 68° STREAMLINE INDICATED IN FIGURE 17. EQUILIBRIUM VALUES ARE ALSO SHOWN.

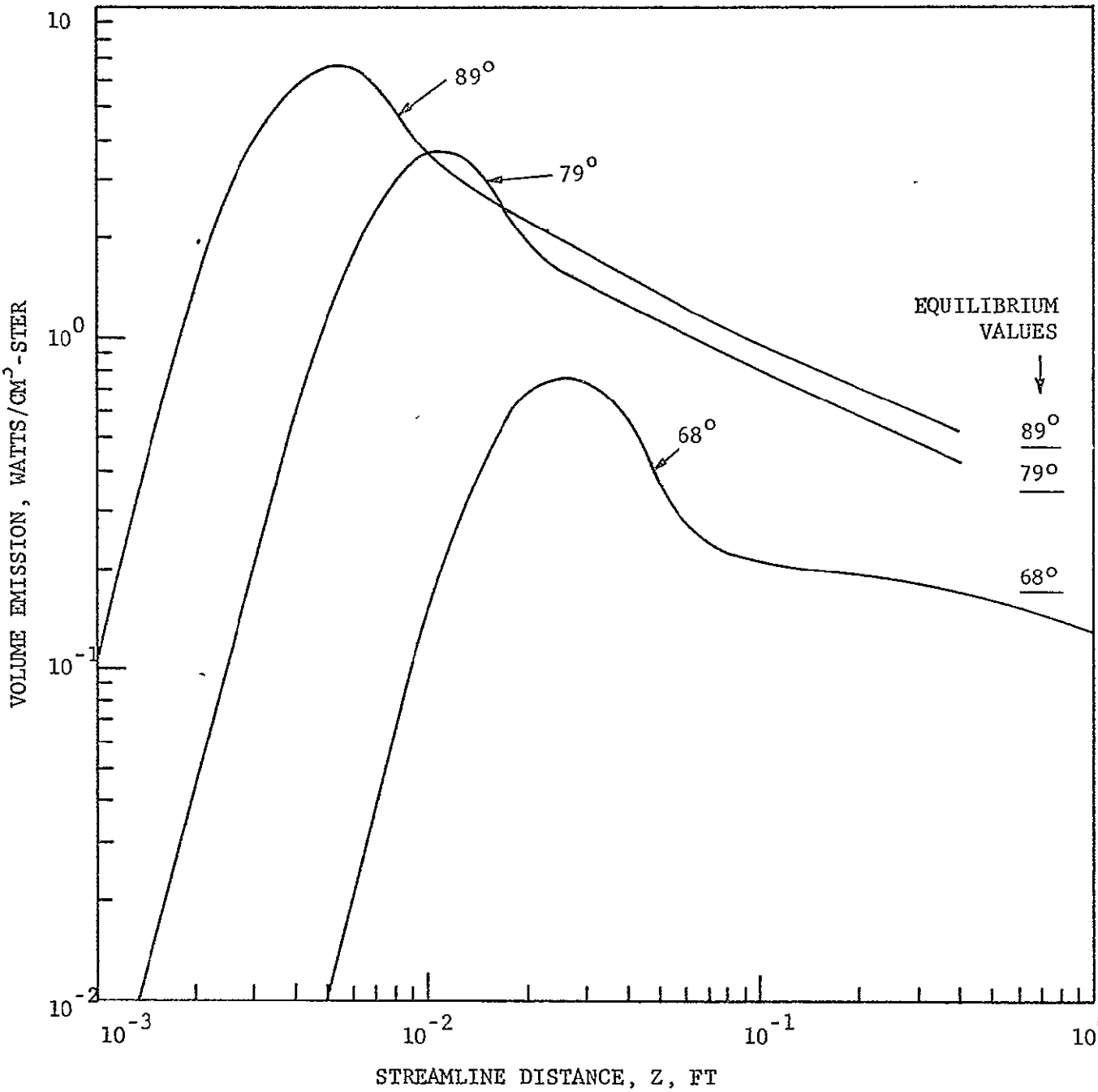

FIGURE 26. NON-EQUILIBRIUM PROFILES OF CN VIOLET EMISSION ALONG THE THREE STREAMLINES INDICATED IN FIGURES 17 AND 19. EQUILIBRIUM VALUES ARE ALSO SHOWN. COLLISION LIMITING CAUSES THE 68° PROFILE TO FALL BELOW EQUILIBRIUM.

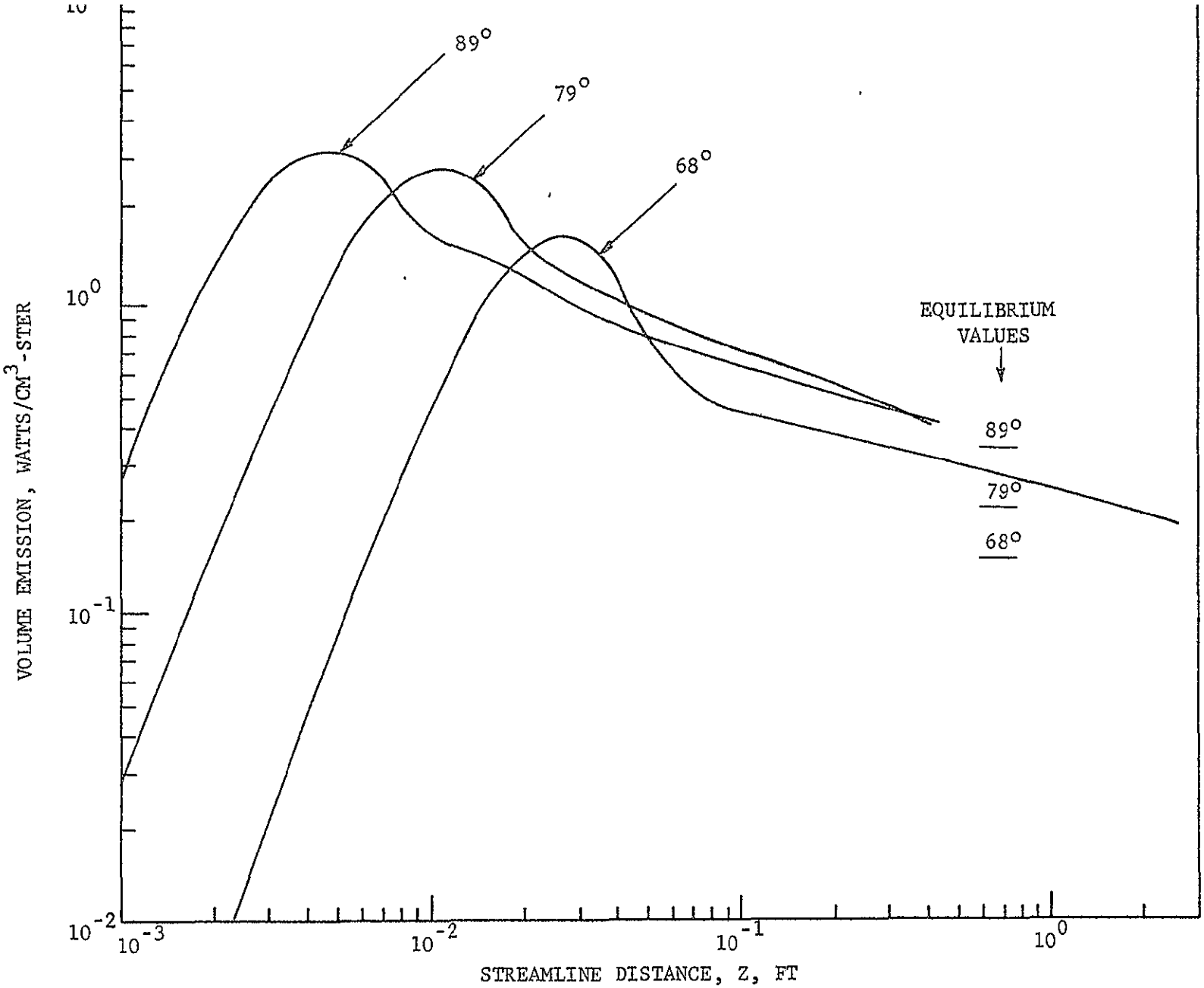

FIGURE 27. NON-EQUILIBRIUM PROFILES OF CN RED EMISSION ALONG THE THREE STREAMLINES INDICATED IN FIGURES 17 AND 19. EQUILIBRIUM VALUES ARE ALSO SHOWN.

Figures 26 and 27. Behind the normal shock the contribution from the CN violet band exceeds that from the CN red band by a factor of about 1.5; behind the 68° shock, the CN red band exceeds the CN violet band by a factor of about 2. The noticeable decrease in CN violet emission is due both to the lower gas temperature behind the oblique shock, and to an increase in the effect of collision limiting.

The total radiative heat transfer to the 6 body points on the sphere-cone shown in Figure 17 is given in Table 12. Radiation to points on the rounded section between the cone and the base was not computed because the non-equilibrium computer program did not run satisfactorily in this region.

The results listed in Table 12 include the effects of self-absorption, thermal boundary layer thickness, and collision limiting. Radiation cooling was not included because the reduction in gas enthalpy is less than 5% and affects the calculated radiation by less than 2%. The thermal boundary layer correction reduces the radiation by about 5%. Self-absorption of CO^{4+} emission reduces the radiation by as much as 6% on the cone surface. The magnitude of the collision limiting effect on CN violet emission is difficult to estimate without making calculations that omit collision limiting, but it is thought to reduce the total radiation to the cone surface by a factor of 1.5 to 2. The contribution to the total radiative heat transfer from the CO vibration-rotation bands and from the CO^{4+} band is 3 to 5% each.

Comparison of the non-equilibrium radiative heat transfer result on the sphere-cone, Table 12, with the equilibrium values shown in Table 9, column 3, indicates an increase by a factor of about 4 in the stagnation region and about 2.5 trhoughout the conical region. It is evident from these results that an equilibrium calculation is misleading for these flight conditions.

TABLE 12

NON-EQUILIBRIUM SPHERE-CONE RADIATIVE HEAT TRANSFER

Position (Figure 17)	Radiative Heat Transfer watts/cm^2
1	20.6
2	15.0
3	7.2
4	12.5
5	22.0
6	23.3

TABLE 13

NON-EQUILIBRIUM SPHERE-CAP RADIATIVE HEAT TRANSFER

Position (Figure 19)	Radiative Heat Transfer, watts/cm^2	
	Non-Equilibrium Region	Total
1	45.5	79.8
2	44.6	75.6
3	27.7	54.6
4	13.8	32.4

Comparison of the non-equilibrium radiative heat transfer on the sphere-cone with the convective heat transfer, Figure 21, shows that the former is only 10% of the latter in the stagnation region. However, on the conical region near the base the radiative heat transfer is 30% of the convective heat transfer and thus represents a significant contribution to the total heat transfer.

c. Sphere-Cap Non-Equilibrium Radiative Heat Transfer. From the non-equilibrium species profiles of Figures 23, 24, and 25, it is seen that non-equilibrium gas properties cover only about 1/3 of the sphere-cap shock layer. The remaining 2/3 of the layer is very close to equilibrium. The width of the non-equilibrium zone was found to vary very little throughout the shock layer, and was approximated by a constant 0.35 ft, shown in Figure 19. Because a major fraction of the shock layer is in equilibrium, the standoff distance computed using the frozen γ result is too large by about 25%. This is corrected in the radiative heat transfer calculation by reducing the thickness of the equilibrium zone by 0.30 ft.

The non-equilibrium radiation emission from the CN red and violet bands along the three streamlines noted above is shown in Figures 26 and 27. As mentioned previously the effect of radiation cooling is very small in the non-equilibrium region and is not included. Beyond the non-equilibrium region radiation cooling is included by reducing the gas enthalpy by the amount of the combined non-equilibrium and equilibrium radiation losses. This reduced enthalpy, listed in Table 11, and the gas pressure are used to obtain equilibrium radiation properties. Representative values of equilibrium volume radiation for various values of enthalpy and pressure are found in Table 5.

Profiles of the volume emission with and without radiation cooling are shown in Figure 28 for the 89^{o} streamline. In these profiles the CO^{4+} emission is omitted because it is so strongly self-absorbed in the sphere-cap flow. However, the CO^{4+} contribution is included in the radiative

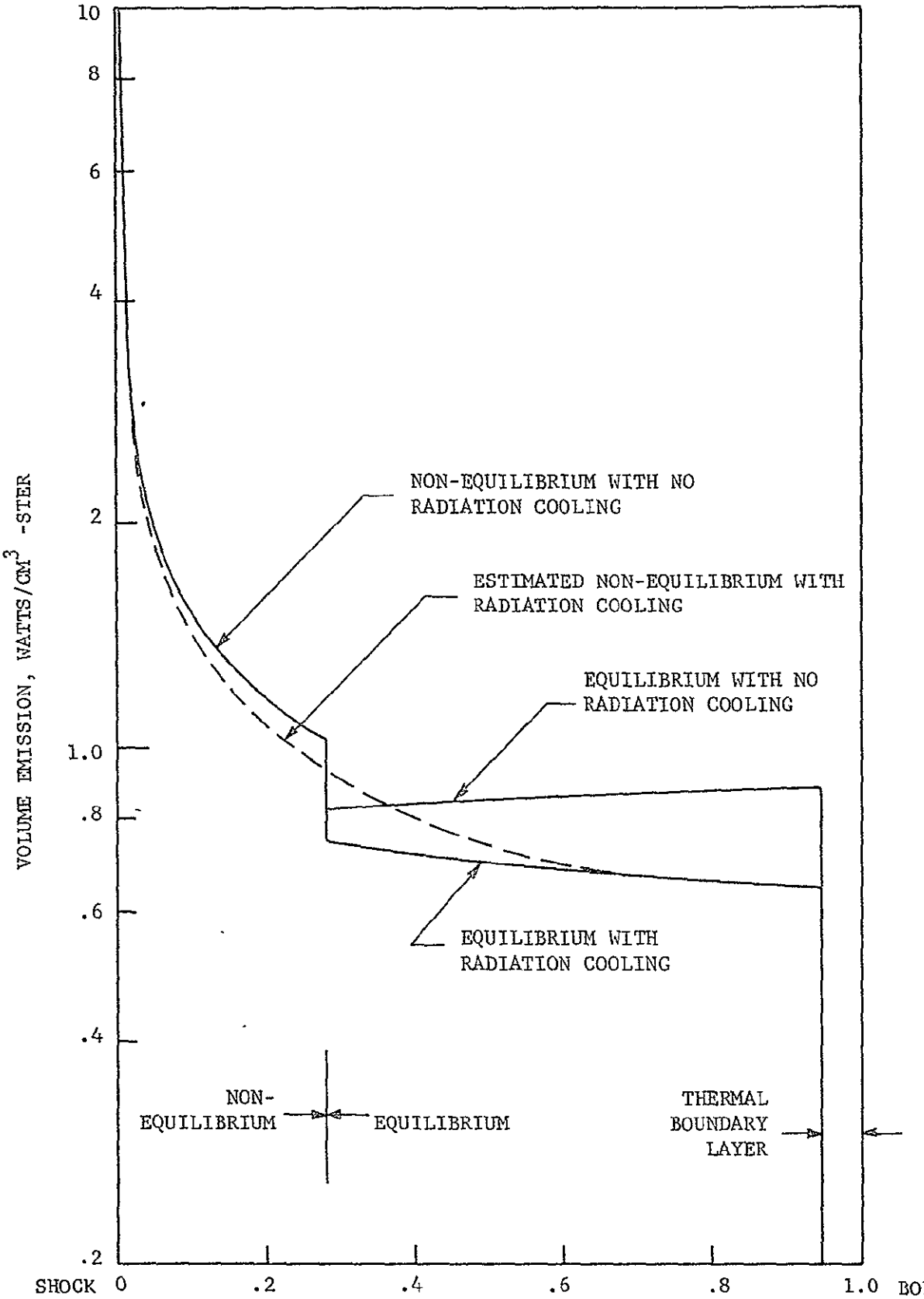

FIGURE 28. RADIATION PROFILES ALONG THE STAGNATION STREAMLINE OF THE SPHERE CAP. THE CN RED AND VIOLET BANDS AND THE CO VIBRATION-ROTATION BAND ARE INCLUDED: THE CO^{4+} BAND IS OMITTED BECAUSE IT IS STRONGLY SELF-ABSORBED.

heat transfer calculation. It is seen that radiation cooling reduces the equilibrium volume emission by as much as 25% at the boundary layer edge. It reduces our calculation of the total radiative heat transfer by about 10% at the stagnation point to about 6% at point 4.

The total radiative heat transfer to the 4 body points shown in Figure 19 is given in Table 13. These results include self-absorption, radiation cooling, thermal boundary layer thickness. Collision limiting in the non-equilibrium region is also included. The CO^{4+} emission is strongly self-absorbed and, as a result, contributes only 4 to 5% of the total radiative heat transfer. The CO vibration-rotation bands contribute about 6% to the total. The remainder arises from the CN red and violet bands There is some self-absorption of the CN violet emission from both the equilibrium and the non-equilibrium regions; this reduces the computed radiative heat transfer by about 10%. The thermal boundary layer correction reduces the radiative heat transfer by about 3%.

The contribution of the non-equilibrium region to the total radiative heat transfer is listed separately in Table 13 and is seen to represent 40% to 60% of the total. If equilibrium gas properties had been assumed, the calculated radiative heat transfer would have been smaller by approximately 35%.

It is seen by comparing the results of Table 13 with the results shown in Figure 22 that the radiative heat transfer exceeds the convective heat transfer throughout the front face of the sphere-cap. This occurs because the shock layer is thick, increasing the radiative heating and reducing the convective heating in comparison to the values found on the sphere-cone.

SECTION 5

CONCLUSIONS AND RECOMMENDATIONS

Methods have been developed and described here for computing the state and motion variables and the convective and radiative heat transfer over the front face of spherically blunted conical bodies traveling at hypersonic speeds through planetary atmospheres under equilibrium or non-equilibrium conditions. The numerical results carried out for Martian entry on a hyperbolic trajectory show the following significant results.

The flow field contains extensive regions of non-equilibrium gas. The non-equilibrium nature of the flow has very little effect on convective heat transfer (Figure 21), but leads to much greater radiative heat transfer than that computed on the basis of equilibrium flow (compare Figures 16 and 21).

The radiative heat transfer computed on the basis of non-equilibrium flow is a significant fraction of the total heat transfer, For the sphere-cap body shape, the radiative heating is more than twice the convective heating at the stagnation point (Figure 22). Although radiative heating is considerably smaller than convective heating on the sphere-cone (Figure 21), this is due to the small standoff distance and the oblique conical shock

that occur on this shape only when the angle of attack is near zero. Although angle of attack calculations were not made in this study, it is expected that at 10^{o} angle of attack the windward portion of the sphere-cone will support a shock angle and standoff distance that are comparable to those typical of the flow over the sphere-cap. Thus radiative heat transfer may exceed convective heat transfer on the sphere-cone at moderate angles of attack.

The low Reynolds number associated with these calculations leads to a significant thickening of the boundary layer. The major result of this is the increase in the convective heat transfer over the value based on a modified Newtonian approximation. The actual convective heating to the sphere-cone (Figure 16) exceeds the modified Newtonian value by more than 50% over most of the surface. This arises because the boundary layer on the conical portion of the sphere-cone extends beyond the low-velocity, high-entropy layer of fluid that passes through the spherical nose region.

The coupling among the inviscid flow, the viscous flow, and the radiation transfer was found to be significant, but amenable to evaluation through first order corrections to the uncoupled results.

It is recommended that in future work the non-equilibrium radiation from the CO fourth positive band be studied experimentally, that collision limiting of the CN violet band be studied experimentally, and that the non-equilibrium analysis be applied to the sphere-cone at small and moderate angles of attack in order to determine the convective and radiative heat transfer rates.

APPENDIX A

DERIVATION OF FINITE DIFFERENCE EQUATIONS

The left hand side and the first term on the right of Equation (6) are seen to be the conservation quantity averages that are desired. Let $\Omega(t)$ be the cell $j+\frac{1}{2}$, $i+\frac{1}{2}$. The area of the cell is denoted at the start of the time step by $G_{j+\frac{1}{2},i+\frac{1}{2}}$ and is determined from

$$G_{j+\frac{1}{2},i+\frac{1}{2}} = \iint_{\Omega(t_o)} dydx \tag{A1}$$

Similarly, the area of $\Omega(t_o+\tau)$ is denoted by $G^{j+\frac{1}{2},i+\frac{1}{2}}$,

$$G^{j+\frac{1}{2},i+\frac{1}{2}} = \iint_{\Omega(t_o+\tau)} dydx \tag{A2}$$

The mean value of the conservation quantity f in the cell $j+\frac{1}{2}$, $i+\frac{1}{2}$ at $t_o+\tau$ is defined by

$$f^{j+\frac{1}{2},i+\frac{1}{2}} = \frac{\iint_{\Omega(t_o+\tau)} f(x,y,t_o+\tau)dydx}{G^{j+\frac{1}{2},i+\frac{1}{2}}} \tag{A3}$$

with a similar definition at t_o for $f_{j+\frac{1}{2},i+\frac{1}{2}}$

The boundary motion gives a contribution only on the segments of the boundary j, $i+\frac{1}{2}$ and $j+1$, $i+\frac{1}{2}$. The ray portions of the boundary are stationary and have $V_n = 0$. The boundary motion contribution to the change in f is, therefore,

$$\int_{t_o}^{t_o+\tau} dt \iint_{\partial\Omega(t)} f(x,y,t)V_n ds = f_{j,i+\frac{1}{2}}G_{j,i+\frac{1}{2}} - f_{j+1,i+\frac{1}{2}}G_{j+1,i+\frac{1}{2}} \qquad (A4)$$

$G_{j,i+\frac{1}{2}}$ denotes the volume swept by the boundary, j, $i+\frac{1}{2}$ as it moves inward,

$$G_{j,i+\frac{1}{2}} = \int_{t_o}^{t_o+\tau} dt \int_{(j,i+\frac{1}{2})} V_n ds \qquad (A5)$$

and

$$G_{j+1,i+\frac{1}{2}} = \int_{t_o}^{t_o+\tau} dt \int_{(j+1,i+\frac{1}{2})} V_n ds \qquad (A6)$$

This definition corresponds to taking the uniform convention for the boundary velocity throughout the grid as positive when it moves toward the body. The velocity V_n is taken outward from each cell, and is inconvenient for use in moving from cell to cell as it must be continually redefined.

Since Equation (A4) is already of order τ compared to $f^{j+\frac{1}{2},i+\frac{1}{2}}G^{j+\frac{1}{2},i+\frac{1}{2}}$ the value of $f_{j,i+\frac{1}{2}}$ need only be correct to zero order,

$$f_{j,i+\frac{1}{2}} = \tfrac{1}{2}(f_{j-\frac{1}{2},i+\frac{1}{2}} + f_{j+\frac{1}{2},i+\frac{1}{2}}) + O([f_{j,i+\frac{1}{2}}])$$

where the bracket denotes the jump in f at the cell boundary. In Godunov's method a specific form is assigned to the first order term in this expression for all boundary quantities. The resulting first order terms stabilize the calculation.

The contributions from the line integral of P,Q about the cell boundary are seen to have the form $\tau(F,S)$ for each edge. Here F is taken to be the two component vector $\{P,Q\}$ and S the two component vector with magnitude equal to the length of the edge and direction along the outward normal to the edge. The notation (F,S) is the scalar product between the two vectors. S can be evaluated for the edge at time t_o, for first order accuracy in Equation (6), since the difference of $\tau(F,S)$ for opposite sides of the cell is already of first order relative to $f^{j+\frac{1}{2},i+\frac{1}{2}}G^{j+\frac{1}{2},i+\frac{1}{2}}$. The flow quantities appearing in (F,S) must be evaluated by Godunov's method for stability. Finally then, the flux contribution is seen to be

$$\int_{t_o}^{t_o+\tau} dt \int_{\partial\Omega(t)} Pdy - Qdx = \tau \sum_{(edges)} (F,S) \tag{A7}$$

For axisymmetric flow the source term in Equation (6) remains to be approximated. Again it is of first order compared to the leading term $f^{j+\frac{1}{2},i+\frac{1}{2}}G^{j+\frac{1}{2},i+\frac{1}{2}}$ so that the geometric factors and flow variables can be evaluated at $t = t_o$. When $y \neq 0$ inside the cell, this term will be approximated by

$$\int_{t_o}^{t_o+\tau} dt \iint_{\Omega(t)} \frac{1}{y} R(x,y,t)dsdy = \tau R_{j+\frac{1}{2},i+\frac{1}{2}} B_{j+\frac{1}{2},i+\frac{1}{2}} \tag{A8}$$

where

$$B_{j+\frac{1}{2},i+\frac{1}{2}} = \iint_{\Omega(t_o)} \frac{1}{y} dydx \tag{A9}$$

and

$$R_{j+\frac{1}{2},i+\frac{1}{2}} = R(f_{j+\frac{1}{2},i+\frac{1}{2}}) \tag{A10}$$

For cells bordering the axis, the expression (A9) is not convergent and must be replaced by the convergent integral

$$B^{o}_{j+\frac{1}{2},\frac{1}{2}} = \iint_{\Omega(t_o)} \frac{v}{y}\, dydx \tag{A11}$$

and a compatible modification of R to R^{o}

$$R^{o}(f) = \begin{matrix} \rho \\ \rho u \\ \rho v \\ \rho(\epsilon + \frac{p}{\rho}) \end{matrix} \tag{A12}$$

Denote Godunov's evaluation of ρ, u, v, p, ϵ on the cell boundaries by R, U, V, P, E respectively. Let $W_{j,i+\frac{1}{2}}$ denote the fluid velocity normal to the segment $j,i+\frac{1}{2}$ directed toward the body and computed from V,U. Similarly let $W_{j+\frac{1}{2},i}$ be the fluid velocity computed from V,U normal to $j+\frac{1}{2},i$ and directed along the shock layer from the axis. By Equations (A3), (A4), (A7) and (A8) the finite difference approximations to Equation (6) are

Conservation of Mass

$$\rho_{j+\frac{1}{2},i+\frac{1}{2}} = -[G^{j+\frac{1}{2},i+\frac{1}{2}}]^{-1}\{(\rho G)_{j+\frac{1}{2},i+\frac{1}{2}} - \tau[(RWS)_{j+\frac{1}{2},i+1} - (RWS)_{j+\frac{1}{2},i}]$$

$$-[R(\tau WS+G)_{j+1,i+\frac{1}{2}} - R(\tau WS+G)_{j,i+\frac{1}{2}}] - \tau k(\rho vB)_{j+\frac{1}{2},i+\frac{1}{2}}\} \tag{A13}$$

Conservation of x momentum

$$u^{j+\frac{1}{2}i+\frac{1}{2}} = [(\rho G)^{j+\frac{1}{2},i+\frac{1}{2}}]^{-1}\{(\rho uG)_{j+\frac{1}{2},i+\frac{1}{2}}$$

$$-\tau[(RUWS)_{j+\frac{1}{2},i+1} - (RUWS)_{j+\frac{1}{2},i}]$$

$$-[RU(\tau WS+G)_{j+1,i+\frac{1}{2}} - RU(\tau WS+G)_{j,i+\frac{1}{2}}]$$

$$-\tau[(PS\sin\sigma)_{j+1,i+\frac{1}{2}} - (PS\sin\sigma)_{j,i+\frac{1}{2}}]$$

$$-\tau[(PS\sin\theta)_{j+\frac{1}{2},i+1} - (PS\sin\theta)_{j+\frac{1}{2},i}]$$

$$-\tau k(\rho uvB)_{j+\frac{1}{2},i+\frac{1}{2}}\} \tag{A14}$$

Conservation of y momentum

$$v^{j+\frac{1}{2},i+\frac{1}{2}} = [(\rho G)^{j+\frac{1}{2},i+\frac{1}{2}}]^{-1}\{(\rho vG)_{j+\frac{1}{2},i+\frac{1}{2}}$$

$$-\tau[RVWS)_{j+\frac{1}{2},i+1} - (RVWS)_{j+\frac{1}{2},i}]$$

$$-[RV(\tau WS+G)_{j+1,i+\frac{1}{2}} - RV(\tau WS+G)_{j,i+\frac{1}{2}}]$$

$$-\tau[(PS\cos\theta)_{j+\frac{1}{2},i+1} - (PS\cos\theta)_{j+\frac{1}{2},i}]$$

$$+\tau[(PS\cos\sigma)_{j+1,i+\frac{1}{2}} - (PS\cos\sigma)_{j,i+\frac{1}{2}}]$$

$$-\tau k(\rho v^2 B)_{j+\frac{1}{2},i+\frac{1}{2}}\} \qquad (A15)$$

Conservation of energy

$$\epsilon^{j+\frac{1}{2},i+\frac{1}{2}} = [(\rho G)^{j+\frac{1}{2},i+\frac{1}{2}}]^{-1}\{(\rho\epsilon G)_{j+\frac{1}{2},i+\frac{1}{2}}$$

$$-\tau[(REWS)_{j+\frac{1}{2},i+1} - (REWS)_{j+\frac{1}{2},i}]$$

$$-[RE(\tau WS+G)_{j+1,i+\frac{1}{2}} - RE(\tau WS+G)_{j,i+\frac{1}{2}}]$$

$$-\tau[(PWS)_{j+\frac{1}{2},i+1} - (PWS)_{j+\frac{1}{2},i}]$$

$$-\tau[(PWS)_{j+1,i+\frac{1}{2}} - (PWS)_{j,i+\frac{1}{2}}]$$

$$-\tau k[\rho\epsilon v+pv)B]_{j+\frac{1}{2},i+\frac{1}{2}}\} \qquad (A16)$$

The difference Equations (A13) through (A16) contain the geometric quantities $G^{j+\frac{1}{2},i+\frac{1}{2}}$; $G_{j+\frac{1}{2},i+\frac{1}{2}}$; $G_{j,i+\frac{1}{2}}$, $S_{j,i+\frac{1}{2}}$; $S_{j+\frac{1}{2},i}$; $B_{j+\frac{1}{2},i+\frac{1}{2}}$ if $y \neq 0$ and $B^{o}_{j+\frac{1}{2},i+\frac{1}{2}}$ when $y = 0$ and $\sin\sigma_{j,i+\frac{1}{2}}$, $\cos\sigma_{j,i+\frac{1}{2}}$.

Thus the area of the cell is explicitly

$$G_{j+\frac{1}{2},i+\frac{1}{2}} = \iint_{\Omega(t_o)} dydx = \phi_{j,i+\frac{1}{2}} - \phi_{j+1,i+\frac{1}{2}} \qquad (A17)$$

where

$$\phi_{j,i+\frac{1}{2}} = \tfrac{1}{2}[\ell^2_{j,i+1}\cos\theta_{i+1}\sin\theta_{i+1} - \ell^2_{j,i}\cos\theta_i\sin\theta_i + (\xi_{i+1} - \ell_{j,i+1}\cos\theta_{i+1}$$

$$-\xi_i + \ell_{j,i}\cos\theta_i)(\ell_{j,i+1}\sin\theta_{i+1} + \ell_{j,i}\sin\theta_i)] \qquad (A18)$$

Similarly

$$G^{j+\frac{1}{2},i+\frac{1}{2}} = \iint_{\Omega(t_o+\tau)} dydx = \phi^{j,i+\frac{1}{2}} - \phi^{j+1,i+\frac{1}{2}} \qquad (A19)$$

with

$$\phi^{j,i+\frac{1}{2}} = \tfrac{1}{2}[(\ell^{j,i+1})^2 \cos\theta_{i+1} \sin\theta_{i+1} - (\ell^{j,i})^2 \cos\theta_i \sin\theta_i$$

$$+ (\xi_{i+1} - \ell^{j,i+1} \cos\theta_{i+1} - \xi_i + \ell^{j,i} \cos\theta_i)(\ell^{j,i+1} \sin\theta_{i+1} + \ell^{j,i} \sin\theta_i)] \quad \text{(A20)}$$

where $\ell^{j,i}$ is the location of $\ell_{j,i}$ at the end of the time interval. The area swept by the boundary $j,i+\frac{1}{2}$ is

$$G^{j,i+\frac{1}{2}} = \phi^{j,i+\frac{1}{2}} - \phi_{j,i+\frac{1}{2}} \quad \text{(A21)}$$

With the same definition holding when j is replaced by $j+1$. The lengths of the sides $S_{j,i+\frac{1}{2}}$, $S_{j+\frac{1}{2},i}$ are given by

$$S_{j+\frac{1}{2},i} = \ell_{j,i} - \ell_{j+1,i} \quad \text{(A22)}$$

and

$$S_{j,i+\frac{1}{2}} = [(\xi_{i+1} - \ell_{j,i+1} \cos\theta_{i+1} - \xi_i + \ell_{j,i} \cos\theta_i)^2 + (\ell_{j,i+1} \sin\theta_{i+1} -$$

$$- \ell_{j,i} \sin\theta_i)^2]^{\frac{1}{2}} \quad \text{(A23)}$$

The sine and cosine of the slope of a ray are determined from θ_i while the sine and cosine of the slope of a segment on the transverse interpolatry polygon are

$$\sin\sigma_{j,i+\frac{1}{2}} = \frac{\ell_{j,i+1} \sin\theta_{i+1} - \ell_{j,i} \sin\theta_i}{S_{j,i+\frac{1}{2}}} \quad \text{(A24)}$$

and

$$\cos\sigma_{j,i+\frac{1}{2}} = \frac{\xi_{i+1} - \ell_{j,i+1} \cos\theta_{i+1} - \xi_i + \ell_{j,i} \cos\theta_i}{S_{j,i+\frac{1}{2}}} \quad \text{(A25)}$$

The factor of the source term for axial symmetry, when $y \neq 0$, is

$$B_{j+\frac{1}{2},i+\frac{1}{2}} = \iint_{\Omega(t_o)} \frac{1}{y}\,dydx = I_{j+\frac{1}{2},i+1} + I_{j+1,i+\frac{1}{2}} - I_{j+\frac{1}{2},i} - I_{j,i+\frac{1}{2}} \tag{A26}$$

where

$$I_{j+\frac{1}{2},i} = \xi_i \ell n \frac{\ell_{i,i}}{\ell_{j+1,i}} \tag{A27}$$

$$I_{j,i+\frac{1}{2}} = [\xi_{i+1} - \ell_{j,i+1}(\cos\theta_{i+1} - \sin\theta_{i+1}\tan\sigma_{j,i+\frac{1}{2}})]$$

$$\ell n\left(\frac{\ell_{j,i+1}\sin\theta_{i+1}}{\ell_{j,i}\sin\theta_i}\right) \tag{A28}$$

If y = 0, the cells border the axis of symmetry, and $B^o_{j+\frac{1}{2},\frac{1}{2}}$ is given by

$$B^o_{j+\frac{1}{2},\frac{1}{2}} = \iint_{\Omega(t_o)} \frac{v}{y}dydx \tag{A29}$$

Since v = 0(y) as y → 0 the above integral is convergent. The integrand in Equation (A29) can be replaced by $\partial v/\partial y\big|_{y=0}$ to first order accuracy throughout the cell. An integration of Equation (A29) can then be performed to yield

$$B_{j+\frac{1}{2},\frac{1}{2}} = \int dx \frac{\partial v_o}{\partial y}(y_u(x) - y_\ell(x)) \tag{A30}$$

where $y_u(x)$ and $y_\ell(x)$ are the upper and lower boundaries of the cell. All cell boundaries are straight lines so that y_u and y_ℓ are proportional to x. Moreover, let $\partial v_o/\partial y$ be approximated by the mean value of V on the boundary segment as determined by the Godunov scheme, divided by the mean y coordinate, Δy, of the segment. Therefore

$$\left(\frac{\partial v_o}{\partial y}\right)_{j,\frac{1}{2}} = \frac{V_{j,\frac{1}{2}}}{\Delta y_{j,\frac{1}{2}}} \tag{A31}$$

and

$$\left(\frac{\partial v_o}{\partial y}\right)_{j+\frac{1}{2},1} = \frac{V_{1+\frac{1}{2},1}}{\Delta y_{j+\frac{1}{2},1}} \tag{A32}$$

From Equation (A30) it is seen that

$$B_{j+\frac{1}{2},\frac{1}{2}} = V_{j,\frac{1}{2}}\Delta x_{j,\frac{1}{2}} + V_{j+\frac{1}{2},1}\Delta x_{j+\frac{1}{2},1} - V_{j+1,\frac{1}{2}}\Delta x_{j+1,\frac{1}{2}} \tag{A33}$$

with the definitions

$$\Delta x_{j,\frac{1}{2}} = \xi_1 - \ell_{j,1}\cos\theta_1 - \xi_o + \ell_{j,o} \tag{A34}$$

$$\Delta x_{j+\frac{1}{2},1} = (\ell_{j,1} - \ell_{j+1,1})\cos\theta_1 \tag{A35}$$

Equations (A33-A35) along with the modified definition of R in Equation (A12) permit the product RB to be evaluated for cells adjoining the axis of symmetry. The definitions of Equations (A26-A28) along with R given in Equation (4) permit evaluation of the product in all other cells.

REFERENCES

1. Goldberg, L., "The Structure of the Viscous Hypersonic Shock Layer," GE TIS R 65-SD50, December 1965.
2. Hayes, W. D., and Probstein, R. F., Hypersonic Flow Theory, Academic Press, New York, 1959.
3. Ferri, A, Zakkay, V, and Ting, L., "Blunt-Body Heat Transfer at Hypersonic Speed and Low Reynolds Numbers," J. Aerospace Sciences, Vol. 28, pp. 962-971, December 1961.
4. Kuby, W. C., "Use of the Method of Integral Relations for the Determination of the Convective Heat Flux to a Re-Entry Body," AIAA Journal, 4, No. 5, 947 (1966).
5. Godunov, S. K., Zabrodin, A. V., and Prokopov, G. P , "The Difference Schemes for Two-Dimensional Unsteady Problems in Gas Dynamics and the Calculation of Flows with a Detached Shock Wave," Translation from the Journal of Computing Mathematics and Mathematical Physics, Academy of Sciences, USSR, 1, No. 6, November-December, 1961, by T. Strelkoff (edited by M. Holt).
6. Bohachevsky, I. O , and Rubin, E. L., "A Direct Method for Computation of Nonequilibrium Flows with Detached Shock Waves," AIAA Journal, 4, No. 4, 600 (1966).
7. Lax, P. D., "Weak Solutions of Nonlinear Hyperbolic Equations and their Numerical Computation," Comm. on Pure and Appl. Math., 7, No. 1, 159-193 (1954).

8. Burstein, S. Z., "Finite Difference Calculations for Hydrodynamic Flows Containing Discontinuities," NYO-1480-33 (1965), AEC Computing and Applied Mathematics Center, Courant Institute of Mathematical Sciences, New York University.
9. Lax, P. D., and Wendroff, B., "Difference Schemes with High Order of Accuracy for Solving Hyperbolic Equations," NYO 9759 (1962), AEC Computing and Applied Mathematics Center, Courant Institute of Mathematical Sciences, New York University.
10. Emery, A. F., "An Evaluation of Several Differencing Methods for Inviscid Fluid-Flow Problems," Sandia Corporation, Livermore Laboratory, March 1967.
11. Rusanov, V., "Calculation of Interaction of Non-Steady Shock Waves with Obstacles," National Research Council of Canada, Translation No. 1027, 1962.
12. Moretti, G. and Abbett, M., "A Time Dependent Computational Method for Blunt Body Flows," AIAA Journal, 4, No. 12, 2136 (1966).
13. Courant, R. and Friedrichs, K. O., Supersonic Flow and Shock Waves, (1948) Interscience Publishers, Inc., New York.
14. Bailey, H. E., "Equilibrium Thermodynamic Properties of Three Engineering Models of Martian Atmosphere," NASA SP-3021 (1965).
15. Korobkin, I. and Gruenewald, K. H., "Investigation of Local Laminar Heat Transfer on a Hemisphere for Supersonic Mach Numbers at Low Rates of Heat Flux," J. Aero Sci., 24 (3), 188 (1957).
16. Kentall, J. J., Jr., "Experiments on Supersonic Blunt Body Flows," Progress Rept. 20-372, Jet Propulsion Lab, California Institute of Technology, Pasadena, Calif. (Feb. 1959).
17. Boison, J. C. and Curtiss, H. A., "An Experimental Investigation of Blunt Body Stagnation Point Velocity Gradient," ARS Journal, 29 (2), 130 (1959).
18. Korkran, "Stagnation Point Velocity Gradient on Two Dimensional and Axisymmetric Bodies in Hypersonic Flow," ARS Journal, 32 (12), 1924 (1962).

19. Li, T. Y. and Geiger, R. E., "Stagnation Point of a Blunt Body in Hypersonic Flow," JAS, 24 (1), 25 (1957).

20. Mangler, K. W., "Some Special Aspects of Hypersonic Flow Fields," Journal Roy. Aero. Soc., 63, 508 (Sept. 1959).

21. Belotserkovskii, O. M., (editor), Supersonic Gas Flow Around Blunt Bodies, NASA Technical Translation F-453, June 1967.

22. Hoshizaki, H., "Heat Transfer in Planetary Atmospheres at Super-Satellite Speeds," ARS Journal, pp. 1544-1552, October, 1962.

23. Scala, S. M., and Gilbert, L. M., "Theory of Hypersonic Laminar Stagnation Region Heat Transfer in Dissociating Gases," G.E. R63 SD40, April 1963.

24. Kuby, W. C., S. R. Byron, R. M. Foster, R. F. Hoglund, and M. Holt, "Analysis of the Project Fire Re-entry Package Flow Field," Aeronutronic Report U-3020, (1964).

25. Lees, L., "Laminar Heat Transfer over Blunt Nosed Bodies at Hypersonic Speeds," Jet Propulsion, Vol. 26, April 1956, pp. 259-269.

26. Cheng, H. K., "The Blunt Body Problem in Hypersonic Flow at Low Reynolds Numbers," Cornell Aeronautical Lab Report, AF-1285-A-10,1963.

27. Oliver, R. C., Stephanou, S. E., and Baier, R. W., "Calculating Free-Energy Minimization," Chem. Eng., 121 (Feb., 1962).

28. Hildenbrand, D. L., "Study of Metal Additives for Solid Propellants - Tables of Thermodynamic Data for Performance Calculations," Aeronutronic Publication No. C-623 (1959).

29. Thomas, G. M., and Menard, W. A., "Experimental Measurements of Non-equilibrium and Equilibrium Radiation from Planetary Atmospheres," AIAA Journal 4, 227 (1966).

30. Main, R. P., and Bauer, E., "Opacities of Carbon-Air Mixtures at Temperatures from 3000°K to 10,000°K," Aeronutronic Report U-3046 (1965).

31. Main, R. P., and Bauer, E., "Equilibrium Opacities of Selected Materials at High Temperatures," Aeronutronic Report No. U-3304(1965).

32. Keck, J. C., et.al., Annals of Physics 7, 1 (1959). Patch, R. W., W. L. Shackleford, and S. S. Penner, J.Q.S.R.T. 2, 263 (1962).
33. Herzberg, G. H., Spectra of Diatomic Molecules, 2nd edition, D. Van Nostrand, Princeton, 1950.
34. Nicholls, R. W., J. Chem. Phys. 24, 1104 (1956).
35. Bates, D. R., M.N.R.A.S. 112, 614 (1952). Nicholls, R. W., J.Q.S.R.T. 2, 433 (1962). Spindler, Franck-Condon Factors Based on RKR Potentials with Application to Radiative Absorption Coefficients, AVCO-RAD-TM-64-55 (September 1964).
36. Soshnikov, V. N., Soviet Physics-Uspekhi 4, 425 (1961). Nicholls, R. W., Ann. de Geophysique 20, 144 (1964). Wentink, T., Jr., et.al., Electronic Oscillator Strengths of Diatomic Molecules, AVCO-RAD-TM-64-33 (July 1964).
37. Mulliken, R. S., J. Chem. Phys. 7, 20 (1939). Mulliken, R. S., and C. A. Rieke, Reports on Progress in Physics VIII, 231 (1941).
38. Breeze, J. C., et.al., J. Chem. Phys. 42, 402 (1965).
39. Breeze, J. C. and C. C. Ferriso, J. Chem Phys. 41, 3420 (1964).
40. Breeze, J. C. and C. C. Ferriso, "Integrated Intensity Measurements on the Fundamental and First Overtone Band Systems of CO between 2500 and 5000^{o}K," General Dynamics/Convair Space Science Laboratory Report GD/C-DBE 65-007, May 1965.
41. Finkelnburg, W. and Peters, Th., "Kontinuerliche Spektren," in S. Flugge (ed.), Handbuch der Physik Vol. XXVIII, Springer, Berlin, 1957.
42. Keck, J. C., R. A. Allen, and R. L. Taylor, J.Q.S.R.T. 3, 335 (1963). Taylor, R. L., "Continuum Infrared Radiation from High Temperature Air and Nitrogen," AVCO-Everett Research Report 154 (1963)
43. Bates, D. R., et.al., Proc. Roy. Soc. A170, 322 (1939).
44. Camac, M., "CO_2 Relaxation Processes in Shock Waves," AVCO Everett Research Report 194 (1964).
45. Wray, K. L., T. S. Freeman, J. Chem. Phys. 40, 2785 (1964).
46. Mayer, J. E., M. G. Mayer, Statistical Mechanics, John Wiley, New York (1940).

47. Wilson, J., "Ionization Rate of Air behind High Speed Shock Waves," AVCO Everett Research Report 222 (1965).

48. Massey, H.S.W. and E.H.S. Burhop, Electronic and Ionic Impact Phenomena, Clarendon Press, Oxford (1952).

49. Bennett, W. R., Jr., P. J. Kindlmann, Bull. Am. Phys. Soc. 8, 87 (1963).

50. Wray, K. L., J. D. Teare, in Atomic Collision Processes, ed. M.R.C. McDowell, North-Holland, Amsterdam, 1123 (1964).

51. Treanor, C. E., "A Method for the Numerical Integration of Coupled First Order Differential Equations with Greatly Different Time Constants," Cornell Aero. Lab. Report No. AG-1729-A-4 (1964).

52. Curtiss, C. F., and J. O. Hirschfelder, Proc. Nat. Acad. Sci. 38, 235 (1952).

53. McKenzie, R. L. and S. O. Arnold, "Experimental and Theoretical Investigations of the Chemical Kinetics and Non-equilibrium CN Radiation behind Shock Waves in CO_2-N_2 Mixtures," AIAA Preprint 67-322, presented at AIAA Thermophysics Specialist Conference, New Orleans, Louisiana, April, 1967.

54. Fay, J. A. and F. R. Riddell, "Theory of Stagnation Point Heat Transfer in Dissociated Air," J. Aero. Sci. 25, 73 (1958).

55. Thomas, G. M. and W. A. Menard, AIAA Journal 4, 227 (1966).

56. Wilson, L. N., "Inflections in Bow Shock Shape at Hypersonic Speeds," AIAA Journal, 5 (8), 1532 (1967).

57. Wurster, W. H., C. E. Treanor, and H. M. Thompson, J. Chem. Phys. 35 2560 (1962).

58. Jeunehomme, M., "Transition Moment of the First Positive System of Nitrogen," (Unpublished).

59. Gilmore, F. R., Approximate Radiative Properties of Air between 2000 and 8000°K, RAND Corporation RM-3997-ARPA, (March, 1964).

60. Jeunehomme, M., "Oscillator Strength of the First Negative and Second Positive Systems of Nitrogen," (Unpublished).

61. Wray, K. L., and T. J. Connolly, J.Q.S.R.T. 5, 633 (1965).

62. Ory, H. A., J. Chem. Phys. 40, 562 (1964).

63. Hesser, J. E. and K. Dressler, Ap. J. 142, 389 (1965).
64. Bennett, R. G., and F. W. Dalby, J. Chem. Phys. 36, 399 (1962).
65. Reis, V. H., J.Q.S.R.T. 5, 585 (1965).
66. Jeunehomme, M., J. Chem. Phys. 42, 4086 (1965).
67. Hicks, W. T., "Spectroscopy of High-Temperature Systems," Univ. of Calif. Rad. Lab. Rept. 3696 (1957).
68. Sviridov, A. G., N. N. Sobolev and V. M. Sutovskii, J.Q.S.R.T 5, 525 (1965).
69. Clementi, E., Ap. J. 132, 898 (1960).
70. Bennett, R. G. and F. W. Dalby, J. Chem. Phys. 32, 11 (1960).
71. Nicholls, R. W., Canad. J. Phys. 43, 1390 (1965).
72. Herzberg, G., Infrared and Raman Spectra of Polyatomic Molecules, D. Van Nostrand, Princeton 1945.
73. Griffing, V., K. V. Laidler, 3rd Symposium on Combustion, Madison, Wisconsin.
74. Hildenbrand, D. L., "Study of Metal Additives for Solid Propellants - Tables of Thermodynamic Data for Performance Calculations," Aeronutronic Report No. C-623 (1959).
75. Berkowitz, J., J. Chem. Phys. 36, 2533 (1962).
76. Davies, W. O., "Carbon Dioxide Dissociation at 6000° to 11,000°K," 43, 2809 (1965).
77. Lin, S. C., J. D. Teare, Phys. of Fluids 6, 355 (1963).
78. Byron, S., J. Chem. Phys. 44, 1378 (1966).
79. Wray, K. L., Progress in Astronautics and Rocketry 7, F. R. Riddell, Ed., Academic Press, 181 (1962).
80. Presley, L. L., C. Chakerian, Jr., and R. Watson, "The Dissociation Rate of Carbon Monoxide between 7,000° and 15,000°K," AIAA Preprint 66-518, presented at 4th Aerospace Sciences Meeting, Los Angeles, June, 1966.
81. McKenzie, R. L., Proc. AIAA-AAS Steping Stones to Mars Meeting, Baltimore (1966).

82. J. Nichols and E. Nierengraten, "Aerodynamic Characteristics of Blunt Bodies," JPL TR 32-677, November 1964. Schlieren photo taken in conjunction with this work.